Fall 2014

Modeling and estimation of crosstalk across a channel with multiple, non-parallel coupling and crossings of multiple aggressors in practical PCBS

Arun Reddy Chada

Department: Electrical and Computer Engineering

MODELING AND ESTIMATION OF CROSSTALK ACROSS A CHANNEL WITH MULTIPLE, NON-PARALLEL COUPLING AND CROSSINGS OF MULTIPLE AGGRESSORS IN PRACTICAL PCBS

by

ARUN REDDY CHADA

A DISSERTATION

Presented to the Faculty of the Graduate School of the

MISSOURI UNIVERSITY OF SCIENCE AND TECHNOLOGY

In Partial Fulfillment of the Requirements for the Degree

DOCTOR OF PHILOSOPHY

in

ELECTRICAL ENGINEERING

2014

Approved
Jun Fan, Advisor
James L. Drewniak
Daryl Beetner
Richard E. Dubroff
Bhyrav Mutnury

ABSTRACT

In Section 1, the focus is on alleviating the modeling challenges by breaking the overall geometry into small, unique sections and using either a Full-Wave or fast equivalent per-unit-length (Eq. PUL) resistance, inductance, conductance, capacitance (RLGC) method or a partial element equivalent circuit (PEEC) for the broadside coupled traces that cross at an angle. The simulation challenge is resolved by seamlessly integrating the models into a statistical simulation tool that is able to quantify the eye opening at BERs that would help electrical designers in locating crosstalk sensitive regions in the high speed backplane channel designs.

Section 2 investigates the FEXT crosstalk impact on eye opening at a specified bit error rate (BER) at different signal speeds for broadside and edge side differential coupled traces in inhomogeneous media and compared the results against homogeneous media models. A set of design guidelines regarding the material, coupled length and stackup parameter selection is formulated for designers based on the signaling speeds.

The major objective of the study in Section 3 is to determine quantitatively the effect of crosstalk due to periodic broadside coupled routing. Another objective is to help designers figure out the “dos” and “don’ts” of broadside coupled routing for higher signaling rates.

A new methodology is proposed in Section 4 to generate BER contours that capture the Tx driver jitter and ISI through the channel accurately using unique waveforms created from truth table bit combinations. It utilizes 2N short N bit patterns as waveforms and jitter correlation from current bit pattern into adjacent bit patterns to get equivalent transient simulation of a very large bit pattern.

ACKNOWLEDGMENTS

I would like to acknowledge, first and foremost, my advisors Dr. Jun Fan and Dr. James L. Drewniak. I should thank them for providing me the opportunity to pursue graduate studies in UMR/MS&T EMC Laboratory, their constant support– both professional and personal, and the flexibility they afforded to me to define and follow my research interests. Their understanding and reassuring nature has often helped me to tide over difficult times in graduate school. I am grateful to work for Dr. Bhyrav Mutnury while at DELL. I always enjoyed having technical discussions with Dr. Bhyrav. He constantly pushed and motivated me to perform at a high level through all the difficult times. I thank Dr. Yaojiang Zhang, whose continued guidance helped me establish the platform from where I could carry on.

I would like to thank Dr. Daryl Beetner, and Dr. Richard DuBroff, for their teaching in my courses, discussions related to my research and helpful suggestions on my dissertation.

I am really grateful to have Dr. Jun Fan and Dr. James L. Drewniak as my advisors as they provided me the opportunity to work with pioneers in the signal integrity and EMC fields. In the process, I have developed my knowledge of the technical subject, good presentation skills and became better at organizing my thoughts.

I would like to thank my parents for all the help both financially and emotionally and my sister for being a life-long source of guidance and inspiration. I would like to thank all my friends for making my stay in graduate school a memorable one.

TABLE OF CONTENTS

LIST OF ILLUSTRATIONS

LIST OF TABLES

1. CROSSTALK ESTIMATION METHODOLOGY ACROSS A VICTIM CHANNEL WITH MULTIPLE, NON PARALLEL COUPLINGS AND CROSSING OF MULTIPLE AGGRESSORS

1.1. INTRODUCTION

Increases in the cost of printed circuit boards (PCB) due to increases in the layer count have led to the design of PCB stack-ups with broadside coupled signals. The broadside coupling of signals in the adjacent layers also leads to crosstalk, which can at times be difficult to model and quantify in terms of its impact on the receiver eye opening. The difficulty stems from the fact that in most boards, multiple occurrences of broadside coupling occur between the signal traces at various angles. The challenges involved in rapid modeling include generating models for the broadside coupled section without the overhead of time-consuming Full-Wave simulations. Full wave simulations are time and memory intensive, especially for coupled traces that are at an angle, and real board designs can have hundreds of these angles. The simulation challenges include accurately predicting the impact of crosstalk on the bit error rate (BER). In this paper, the coupling between high-speed signal traces in adjacent layers is studied. As the signaling speeds increase from generation to generation, the need to estimate the impact of crosstalk on the overall system BER is important. This paper focuses on alleviating the modeling challenges by breaking the overall geometry into small, unique sections and using either a Full-Wave or fast equivalent per-unit-length (Eq. PUL) [1,10] resistance, inductance, conductance, capacitance (RLGC) method or a partial element equivalent circuit (PEEC) for the broadside coupled traces that cross at an angle. The simulation challenge is resolved by seamlessly integrating the models into a statistical simulation tool that is able to quantify the eye opening at BERs that would help electrical designers develop a set of design and routing guidelines that can save PCB cost while maintaining electrical integrity.

A complex topology of the broadside coupled traces in a real design is shown in Figure 1.1. However, the analysis of this topology has modeling challenges, including quickly generating models for the entire section without the overhead of time consuming Full-Wave simulations.

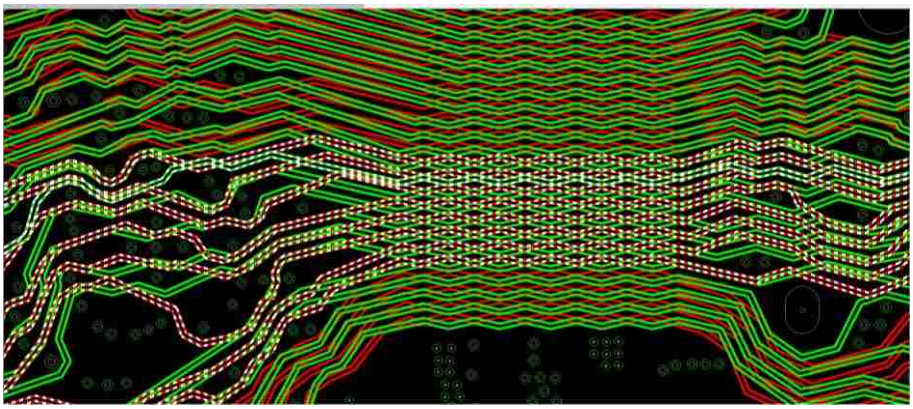

Figure 1.1. Broadside coupled traces in a real design

The coupling between parallel broadside coupled traces can be modeled using a multi-conductor transmission line theory that is based on telegrapher equations that use the per-unit-length (PUL) resistance, inductance, capacitance, and conductance (RLCG) matrices. However, the same approach is not applicable for the traces crossing at arbitrary angles. Previous work on modeling the coupling between the signal traces in [4, 5, 6] accounted the EM fields coupled from the aggressor on the victim as forcing terms in the telegrapher's equations. The coupling between the orthogonally routed traces was studied using the modified telegrapher equations in [2, 3]. For the traces crossing at an angle, the geometry was broken in to numerous small sections, and each section was modeled using the telegraphers equation from [7, 8], which uses the per-unit-length (PUL) resistance, inductance, conductance, capacitance (RLGC) model and assumes the sections are invariant. However, it requires a large number of sections to model the coupling physics accurately, which is time and memory intensive.

A quick methodology used to develop the Eq PUL RLGC models that capture the coupling physics of the broadside coupled traces crossing at an angle based on geometrical parameters of the stack-up and the dielectric material properties is proposed in [1]. The modeling approach proposed in [1], the traces that cross at an angle are modeled using a fast equivalent per-unit-length (Eq PUL) resistance, inductance, conductance, capacitance (RLGC) approach. The method is fast compared to the use of

Full-Wave modeling to extract the S-parameters. Empirical relations for resistance, inductance, conductance, capacitance (RLGC) matrices can be generated from multivariate curve fitting. In equivalent the per-unit-length (Eq PUL) resistance, inductance, conductance, capacitance (RLGC) approach [10], only the mutual inductance and capacitance matrices are optimized. The first step in the process is to obtain the per-unit-length (PUL) resistance, inductance, conductance, capacitance (RLGC) parameters of the parallel broadside coupled traces with the same stack-up as the initial starting point for the optimization process. The goal is to minimize the error between the Z parameters obtained using the equivalent per-unit-length (Eq PUL) resistance, inductance, conductance, capacitance (RLGC) model and the Z-parameters of the full wave model until it reaches the specified error criteria.

The Z-parameters are computed using the equivalent per-unit-length (Eq PUL) resistance, inductance, conductance, capacitance (RLGC) model with the chain parameters from [9] at every iteration. The chain parameters can be expressed as an infinite series of impedance and admittance matrices [9] and are applicable to traces that cross at an angle. The validation of the equivalent per-unit-length (Eq PUL) resistance, inductance, conductance, capacitance (RLGC) model has been done by [10] who modeled a 10-inch broadside coupled section with 45-degree angular coupled sections using the equivalent per-unit-length (Eq. PUL) model and Full-Wave solver, which resulted in similar eye width/height at a given BER with less than a 1% difference.

The signal speeds of high-speed serial links double almost every generation, and due to these increasing speeds, a wide range of new modeling and simulation challenges occur, including ensuring that models are passive, stable, and causal. Frequency-domain models, such as scattering parameter models that have measurement noise, limited bandwidth, incorrectly performed interpolation, and extrapolation operations, may exhibit non-causality and non-passivity in the time domain. Simulating millions of bits in a time-domain to measure the interface merit in terms of the BER is CPU and memory intensive.

Previously, it was shown in [11] that various simulation approaches provide similar answers at low interface speeds and different results at high interface speeds. Hence, it becomes important to understand the inherent assumptions of the simulation approach taken while simulating a high-speed interface. The sensitivity of simulation

approaches on SPICE-like circuit solvers was also discussed. It is a good design practice for high-speed design engineers to understand the sensitivity of the interface used in modeling and underlying simulation (statistical) assumptions and validate the results against the measurements.

Design engineers need a quick analysis approach to estimate the impact of broadside coupling due to various geometrical parameters of the stack-up. A metric that can estimate the crosstalk impact on the eye opening at a specified BER for a high data rate channel has not been previously developed. Therefore, an end-to-end crosstalk estimation methodology that quickly estimates the crosstalk impact on the BER eye contour of the receiver is proposed in this paper. The overall geometry of the coupled section is broken down into multiple sections that are modeled using either the Eq P.U.L RLGC, Full-Wave, or partial equivalent element circuit (PEEC) methods. The individual S-parameter blocks are then cascaded together to generate the S-parameter block of the entire section. Mathematical models of the voltage transfer functions of the throughput (THRU), near end crosstalk (NEXT), and far end crosstalk (FEXT) channels are generated using the S-parameter blocks. The voltage transfer functions are then converted to rational functions using a vector fitting algorithm. The impulse response of the THRU, NEXT, and FEXT channels are then obtained using the vector fitting algorithm. The impulse responses are then used to generate the statistical BER contours using statistical eye analysis approaches.

The crosstalk estimation methodology of the complex broadside routing observed in real PCBs is explained in Section 1.2. The validation of the block-by-block crosstalk methodology is performed in Section 1.3. The methodology is applied to a real coupled section from a complex PCB in Section 1.4. Section 1.5 summarizes the paper.

1.2. CROSSTALK ESTIMATION METHODOLOGY

The crosstalk estimation methodology can be broken into four major steps, as shown in Figure 1.2. The first step is to breakdown the end-to-end coupled section based on the victim and aggressor channels under study. After the aggressor and victim channels are identified, next step is to scan the entire geometry to find unique geometry

parts. After conducting a manual scan of the end-to-end complex broadside coupled section observed in real PCB's (see Figure 1.1), the overall geometry with several angular coupled sections can be modeled using only three unique geometry shapes, as seen in Figure 1.3.

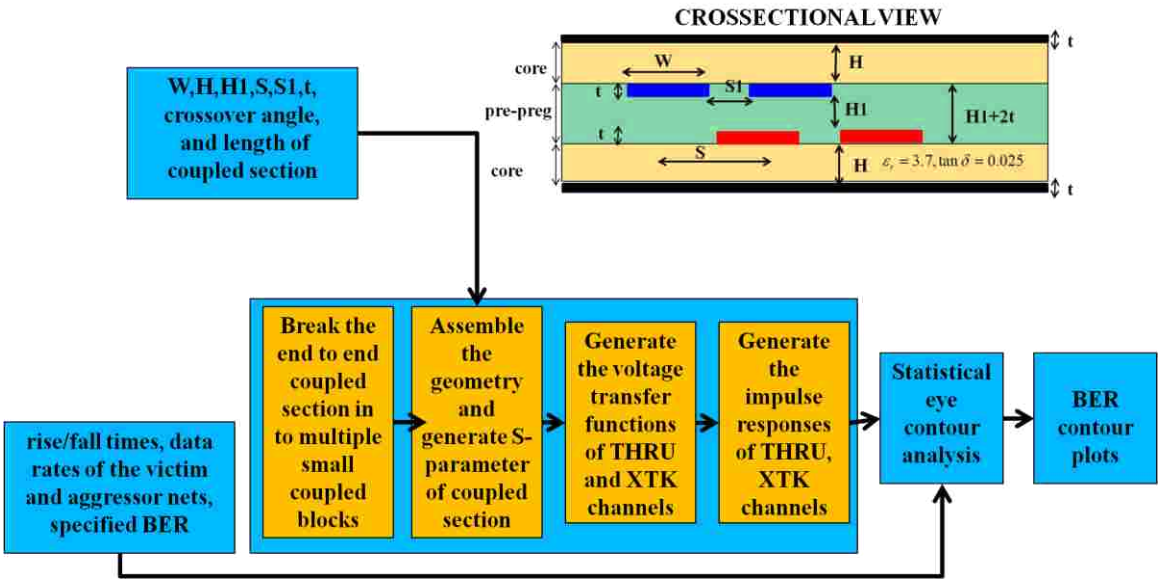

Figure 1.2. Process flow steps to estimate crosstalk impact in real PCB's

The majority of the unique geometry parts extracted while breaking down the victim and aggressor nets coupling path falls into three categories, as shown in Figure 1.3. The geometry breakdown of the end-to-end coupling path is very useful to quickly simulate the overall link. Since the parts are unique, with only variation in the angle and length of the parts, maintaining the library of parts is easy. The parallel coupled parts can be modeled quickly using 2D solvers without the overhead of Full-Wave simulations. Another advantage of this breakdown is one-to-one mapping of the output response to the geometry part. The library of geometry unique parts can be created for the complex PCB

under study. The number of parts in the library depends on the number of unique crossover angles, coupled section length, and the spacing between the victim and aggressor traces for the parallel parts.

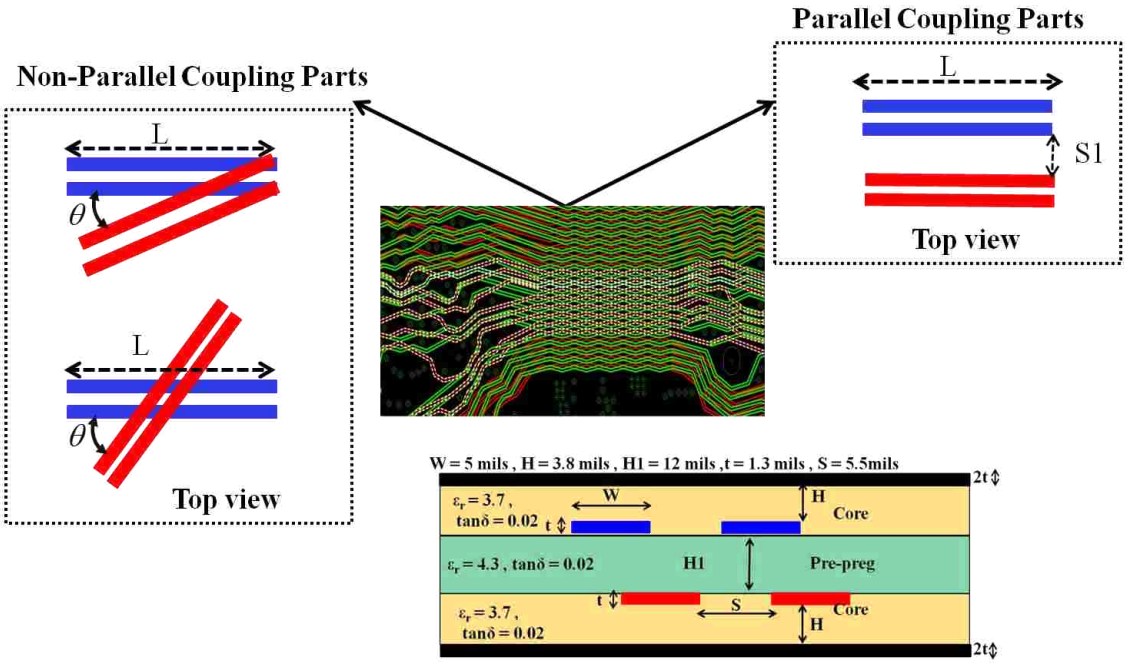

Figure 1.3. Unique geometry parts found in the real PCB's

The angle of crossover in angled coupled traces (see Figure 1.4) plays an important role in determining the length of the victim, and the aggressor traces the lengths when creating the library of parts. The coupling between the victim and aggressor traces saturates when the center-to-center spacing of S is greater than or equal to 13 H. The upper bound of S decides the length of the traces based on the angle. If the unique geometry part observed in the complex PCB's has a longer length than the upper bound, the extra length is modeled as uncoupled transmission lines. Unique parts with lengths smaller than the upper bound need to be simulated every time there is a unique length.

This burden can be alleviated through modeling each of three unique parts' sweeping crossover angle, center-to-center spacing, and coupled length until the upper bound of each variable is reached. The points where the sweep is performed should be chosen intelligently based on the functional variation of the crosstalk with respect to the angle, center-to-center spacing, and length. After the simulations are performed, a multi-variant curve fitting can be used to generate empirical relations for the S-parameters of the three types of unique geometry parts.

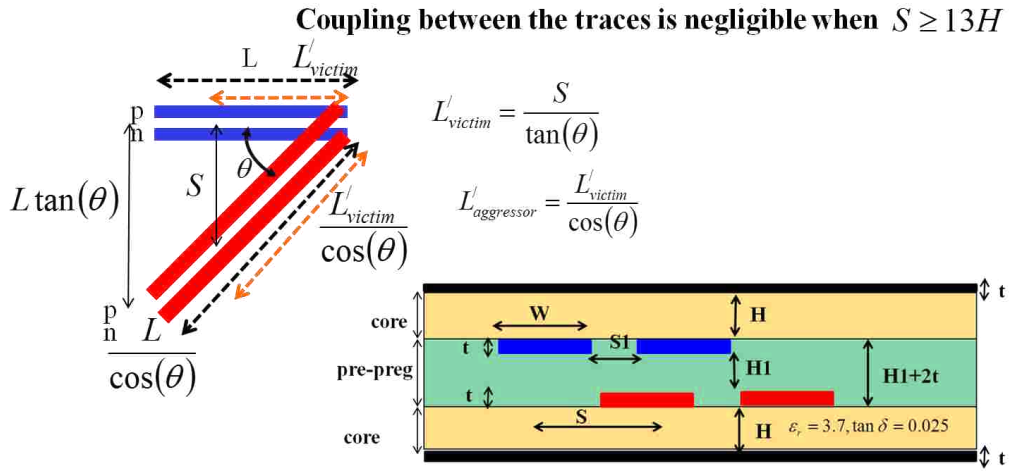

Figure 1.4. Sensitivity of crossover angle to the coupled section length

The geometry breakdown of the end-to-end coupling path between the victim and aggressor nets is explained in a step-by-step fashion (see Figure 1.5). The first step in the process is to identify the parts that when cascaded together give us the end-to-end geometry of the link. The next step is to obtain the S-parameters of each and every geometry part using the Eq PUL RLGC, PEEC circuit, or the Full-Wave model. The S-parameters of the individual parts are then cascaded using the analytical formulation given to obtain the global S-parameter block of the end-to-end coupling path.

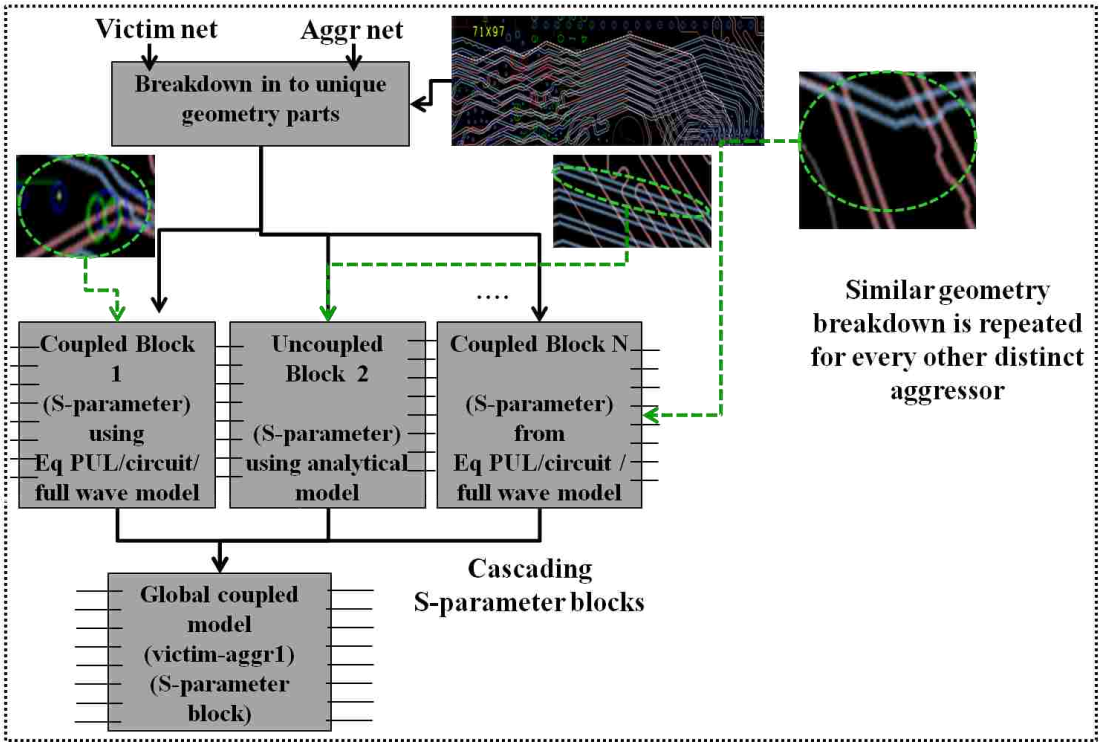

Figure 1.5. Generating the S-parameter of the end-to-end coupled link between the victim and aggressor channels

The cascading relations for cascading two S-parameter blocks are given as

$$S_{total} = \begin{bmatrix} B_1A_2(I - D_1A_2)^{-1}C_1 + A_1 & B_1A_2(I - D_1A_2)^{-1}D_1B_2 + B_1B_2 \\ C_2(I - D_1A_2)^{-1}C_1 & C_2(I - D_1A_2)^{-1}D_1B_2 + D_2 \end{bmatrix} \quad (1)$$

where,

$$S_1 = \begin{bmatrix} A_1 & B_1 \\ C_1 & D_1 \end{bmatrix}$$

$$S_2 = \begin{bmatrix} A_2 & B_2 \\ C_2 & D_2 \end{bmatrix}$$

This relation is used recursively until all the S-parameter blocks are exhausted. The final cascaded S-parameter matrix representing the end-to-end coupled section can be written as

$$S_{total} = \begin{bmatrix} A & B \\ C & D \end{bmatrix} \tag{2}$$

The global S-parameter block along with the source and load terminations is used to compute the voltage transfer function of the throughput (THRU) of the victim and crosstalk(XTK) from the aggressor channels using the formulation shown in equations (3)–(2). The process flow to generate the THRU and XTK channel rational functions is shown in Figure 1.6.

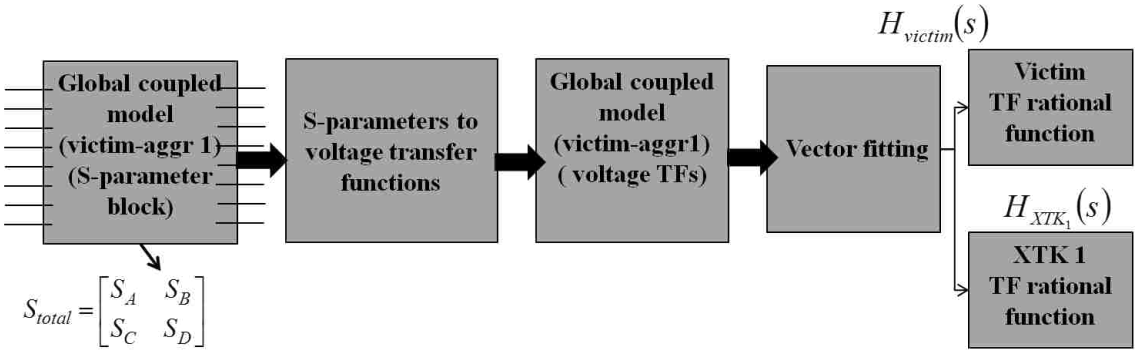

Figure 1.6. Generating the rational functions from S-parameter of the end-to-end coupled link between the victim and aggressor channels

$$\begin{bmatrix} b_1 \\ . \\ . \\ b_n \\ b_{n+1} \\ . \\ . \\ b_{2n} \end{bmatrix} = \begin{bmatrix} A & B \\ C & D \end{bmatrix} \begin{bmatrix} a_1 \\ . \\ . \\ a_n \\ a_{n+1} \\ . \\ . \\ a_{2n} \end{bmatrix} \tag{3}$$

The boundary condition satisfied at the load is

$$\begin{bmatrix} a_{n+1} \\ . \\ . \\ a_{2n} \end{bmatrix} = [S_{LOAD}] \begin{bmatrix} b_{n+1} \\ . \\ . \\ b_{2n} \end{bmatrix} \tag{4}$$

where,

$$[S_{LOAD}] = \left(\hat{Z}_{LOAD} + \hat{Z}_0\right)^{-1} \left(\hat{Z}_{LOAD} - \hat{Z}_0\right)$$

$$\hat{Z}_0 = \begin{bmatrix} Z_0 & 0 & . & 0 \\ 0 & Z_0 & . & 0 \\ . & 0 & Z_0 & 0 \\ 0 & 0 & 0 & Z_0 \end{bmatrix}$$

where Z_0 is the port impedance of port n.

The total voltages at the load terminals are given using

$$\begin{bmatrix} V_{n+1} \\ \cdot \\ \cdot \\ V_{2n} \end{bmatrix} = \left(\sqrt{Z_0} I\right) \left(\begin{bmatrix} a_{n+1} \\ \cdot \\ \cdot \\ a_{2n} \end{bmatrix} + \begin{bmatrix} b_{n+1} \\ \cdot \\ \cdot \\ b_{2n} \end{bmatrix} \right) \tag{5}$$

The total currents at the load terminals are given using

$$\begin{bmatrix} I_{n+1} \\ \cdot \\ \cdot \\ I_{2n} \end{bmatrix} = \left(\frac{1}{\sqrt{Z_0}} I \right) \left(\begin{bmatrix} a_{n+1} \\ \cdot \\ \cdot \\ a_{2n} \end{bmatrix} - \begin{bmatrix} b_{n+1} \\ \cdot \\ \cdot \\ b_{2n} \end{bmatrix} \right) \tag{6}$$

The boundary condition satisfied at the source is found using

$$\begin{bmatrix} V_1^S \\ \cdot \\ \cdot \\ V_n^S \end{bmatrix} = \begin{bmatrix} V_1 \\ \cdot \\ \cdot \\ V_n \end{bmatrix} + \left[\hat{Z}_{SOURCE}\right] \begin{bmatrix} I_1 \\ \cdot \\ \cdot \\ I_n \end{bmatrix} \tag{7}$$

The total voltages at the source terminals are given using

$$\begin{bmatrix} V_1 \\ \cdot \\ \cdot \\ V_n \end{bmatrix} = \left(\sqrt{Z_0} I\right) \left(\begin{bmatrix} a_1 \\ \cdot \\ \cdot \\ a_n \end{bmatrix} + \begin{bmatrix} b_1 \\ \cdot \\ \cdot \\ b_n \end{bmatrix} \right) \tag{8}$$

The total currents at the source terminals are given using

$$\begin{bmatrix} I_1 \\ \cdot \\ \cdot \\ I_n \end{bmatrix} = \left(\frac{1}{\sqrt{Z_0}} I \right) \left(\begin{bmatrix} a_1 \\ \cdot \\ \cdot \\ a_n \end{bmatrix} - \begin{bmatrix} b_1 \\ \cdot \\ \cdot \\ b_n \end{bmatrix} \right) \tag{9}$$

Substituting (8) and (9) in (7) modifies the equation to

$$\begin{bmatrix} V_1^S \\ \cdot \\ \cdot \\ V_n^S \end{bmatrix} = E \begin{bmatrix} a_1 \\ \cdot \\ \cdot \\ a_n \end{bmatrix} + F \begin{bmatrix} b_1 \\ \cdot \\ \cdot \\ b_n \end{bmatrix} \tag{10}$$

where,

$$E = \left(\sqrt{Z_0} I + \left[\hat{Z}_{SOURCE} \right] \frac{1}{\sqrt{Z_0}} I \right)$$

$$F = \left(\sqrt{Z_0} I - \left[\hat{Z}_{SOURCE} \right] \frac{1}{\sqrt{Z_0}} I \right)$$

Equations (5) and (6) can be re-written using the relation in (4) as

$$\begin{bmatrix} V_{n+1} \\ \cdot \\ \cdot \\ V_{2n} \end{bmatrix} = \sqrt{Z_0} I \left(\left[S_{LOAD} \right] + I \right) \begin{bmatrix} b_{n+1} \\ \cdot \\ \cdot \\ b_{2n} \end{bmatrix} \tag{11}$$

$$\begin{bmatrix} I_{n+1} \\ \cdot \\ \cdot \\ I_{2n} \end{bmatrix} = \frac{1}{\sqrt{Z_0}} I\left(\left[S_{LOAD}\right] - I\right) \begin{bmatrix} b_{n+1} \\ \cdot \\ \cdot \\ b_{2n} \end{bmatrix} \tag{12}$$

From equation (3)

$$\begin{bmatrix} b_{n+1} \\ \cdot \\ \cdot \\ b_{2n} \end{bmatrix} = \left[C\right] \begin{bmatrix} a_1 \\ \cdot \\ \cdot \\ a_n \end{bmatrix} + \left[D\right] \begin{bmatrix} a_{n+1} \\ \cdot \\ \cdot \\ a_{2n} \end{bmatrix} \tag{13}$$

$$\begin{bmatrix} b_{n+1} \\ \cdot \\ \cdot \\ b_{2n} \end{bmatrix} = \left[C\right] \begin{bmatrix} a_1 \\ \cdot \\ \cdot \\ a_n \end{bmatrix} + \left[D\right]\left[S_{LOAD}\right] \begin{bmatrix} b_{n+1} \\ \cdot \\ \cdot \\ b_{2n} \end{bmatrix} \tag{14}$$

$$\begin{bmatrix} b_{n+1} \\ \cdot \\ \cdot \\ b_{2n} \end{bmatrix} = \left(\left[I\right] - \left[D\right]\left[S_{LOAD}\right]\right)^{-1} \left[C\right] \begin{bmatrix} a_1 \\ \cdot \\ \cdot \\ a_n \end{bmatrix} \tag{15}$$

Similarly from equation (3)

$$\begin{bmatrix} b_1 \\ \cdot \\ \cdot \\ b_n \end{bmatrix} = \left[A\right] \begin{bmatrix} a_1 \\ \cdot \\ \cdot \\ a_n \end{bmatrix} + \left[B\right] \begin{bmatrix} a_{n+1} \\ \cdot \\ \cdot \\ a_{2n} \end{bmatrix} \tag{16}$$

$$\begin{bmatrix} b_1 \\ \cdot \\ \cdot \\ b_n \end{bmatrix} = \left([A] + [B][S_{LOAD}]([I] - [D][S_{LOAD}])^{-1}[C] \right) \begin{bmatrix} a_1 \\ \cdot \\ \cdot \\ a_n \end{bmatrix} \tag{17}$$

Substituting (10) in (16) results in

$$\begin{bmatrix} a_1 \\ \cdot \\ \cdot \\ a_n \end{bmatrix} = \left(E + F\left([A] + [B][S_{LOAD}]([I] - [D][S_{LOAD}])^{-1}[C] \right) \right)^{-1} \begin{bmatrix} V_1^S \\ \cdot \\ \cdot \\ V_n^S \end{bmatrix} \tag{18}$$

Define P as

$$[P] = \left(E + F\left([A] + [B][S_{LOAD}]([I] - [D][S_{LOAD}])^{-1}[C] \right) \right)^{-1}$$

Equation (18) can be re-written as

$$\begin{bmatrix} a_1 \\ \cdot \\ \cdot \\ a_n \end{bmatrix} = [P] \begin{bmatrix} V_1^S \\ \cdot \\ \cdot \\ V_n^S \end{bmatrix} \tag{19}$$

Substituting equation (19) in equation (15) results in

$$\begin{bmatrix} b_{n+1} \\ \cdot \\ \cdot \\ b_{2n} \end{bmatrix} = ([I] - [D][S_{LOAD}])^{-1}[C][P] \begin{bmatrix} V_1^S \\ \cdot \\ \cdot \\ V_n^S \end{bmatrix} \tag{20}$$

Substituting equation (20) in equations (11) and (12) results in

$$\begin{bmatrix} V_{n+1} \\ \cdot \\ \cdot \\ V_{2n} \end{bmatrix} = \sqrt{Z_0}\, I\left([S_{LOAD}] + I\right)\left([I] - [D][S_{LOAD}]\right)^{-1}[C][P]\begin{bmatrix} V_1^S \\ \cdot \\ \cdot \\ V_n^S \end{bmatrix} \tag{21}$$

$$\begin{bmatrix} I_{n+1} \\ \cdot \\ \cdot \\ I_{2n} \end{bmatrix} = \frac{1}{\sqrt{Z_0}}\, I\left([S_{LOAD}] - I\right)\left([I] - [D][S_{LOAD}]\right)^{-1}[C][P]\begin{bmatrix} V_1^S \\ \cdot \\ \cdot \\ V_n^S \end{bmatrix} \tag{22}$$

Substituting equations (20) and (17) in equations (8) and (9) results in

$$\begin{bmatrix} V_1 \\ \cdot \\ \cdot \\ V_n \end{bmatrix} = \left(\sqrt{Z_0}\, I\right)\left([I] + \left([A] + [B][S_{LOAD}]\left([I] - [D][S_{LOAD}]\right)^{-1}[C]\right)\right)[P]\begin{bmatrix} V_1^S \\ \cdot \\ \cdot \\ V_n^S \end{bmatrix} \tag{23}$$

$$\begin{bmatrix} I_1 \\ \cdot \\ \cdot \\ I_n \end{bmatrix} = \left(\frac{1}{\sqrt{Z_0}}\, I\right)\left([I] + \left([A] + [B][S_{LOAD}]\left([I] - [D][S_{LOAD}]\right)^{-1}[C]\right)\right)[P]\begin{bmatrix} V_1^S \\ \cdot \\ \cdot \\ V_n^S \end{bmatrix} \tag{24}$$

Equations (21) and (23) can be written as

$$\begin{bmatrix} V_{n+1} \\ \cdot \\ \cdot \\ V_{2n} \end{bmatrix} = [X]\begin{bmatrix} V_1^S \\ \cdot \\ \cdot \\ V_n^S \end{bmatrix} \tag{25}$$

where,

$$[X] = \sqrt{Z_0} I([S_{LOAD}] + I)([I] - [D][S_{LOAD}])^{-1}[C][P]$$

$$\begin{bmatrix} V_1 \\ \cdot \\ \cdot \\ V_n \end{bmatrix} = [Y] \begin{bmatrix} V_1^S \\ \cdot \\ \cdot \\ V_n^S \end{bmatrix} \tag{26}$$

where,

$$[Y] = \left(\sqrt{Z_0} I\right)([I] + ([A] + [B][S_{LOAD}]([I] - [D][S_{LOAD}])^{-1}[C]))[P]$$

By exciting only the aggressor channel, the THRU and XTK voltages can be computed. The ratio of the THRU and XTK voltages with respect to the source voltages is defined as THRU and XTK voltage transfer functions. The voltage transfer functions are converted into rational functions using the vector fitting approach.

The impulse of the THRU and XTK channels is then computed from their rational functions.

$$H_{voltage}(s) \approx \sum_{i=1}^{m} \frac{q_i}{s - p_i} \tag{27}$$

The impulse response can be obtained from the rational function given in equation (27) as

$$h(t) = \sum_{i=1}^{m} q_i e^{p_i t} \tag{28}$$

The final step of this methodology generates the THRU and XTK channel responses to obtain the BER eye contours. The impulse response is used to compute the time domain response of the THRU and XTK channels using the convolution technique with either user-defined input stimuli or unique input stimuli with n-bit combinations. The value of n is decided based on the settling time of the THRU and XTK channels' pulse/step responses. The value of n for the THRU and XTK channels is different as the impulse responses are different. The procedure is repeated for all the other aggressor and victim coupling paths. The entire process flow of generating BER eye contours is illustrated in Figure 1.7.

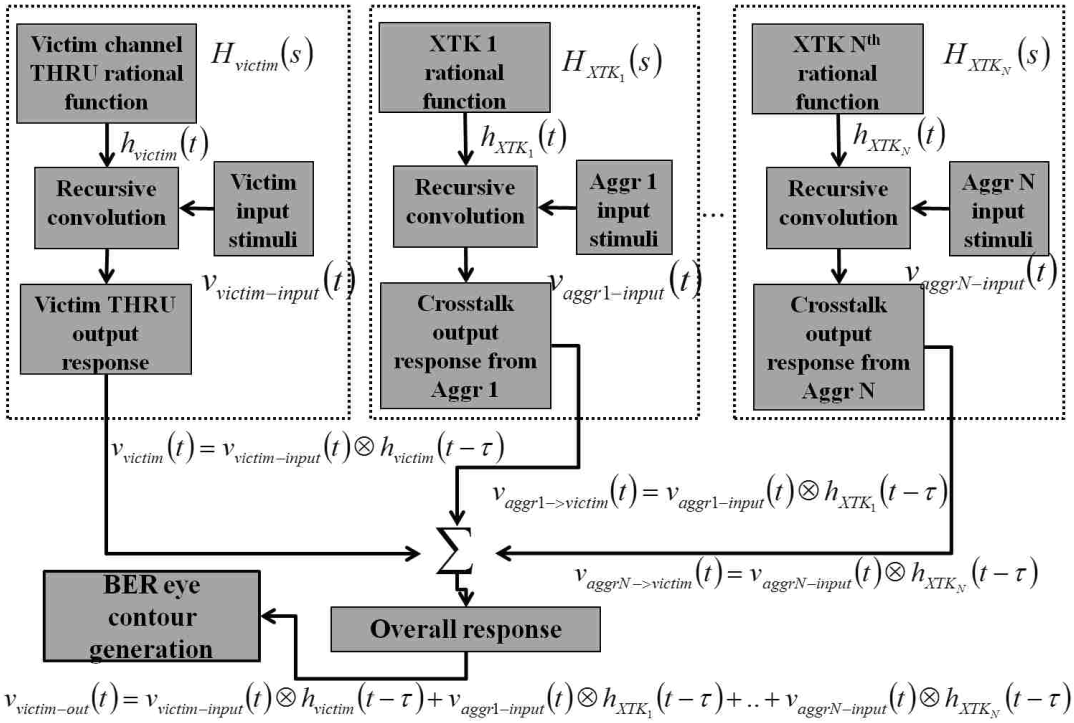

Figure 1.7. Generating the time-domain responses of the end-to-end coupled link with the victim and aggressor channels to create BER eye contour

The input stimuli is constructed using truth table bit combinations. These truth table combinations cover all the different transitions that are possible. The overall responses of all the truth table patterns are superimposed on a single eye diagram grid. A 2D histogram is generated for such a grid to acquire the probability density function. Each column of the 2D histogram is a voltage PDF. The crosstalk PDF is also generated. The crosstalk PDF is convolved with the ISI PDF to generate the overall PDF observed at the receiver in the presence of the crosstalk. The overall PDF is then converted to a cumulative distribution function (CDF). By generating the contour map of the CDF, the BER contours can be obtained. The procedure to generate the BER eye contours is discussed in detail in the final chapter. Other methods used to generate the BER contours include the stat-eye method or the generation of an eye diagram using in house fast electromagnetic analysis suite (FEMAS) for the pseudo random bit sequence (PRBS) patterns.

1.3. VALIDATION OF METHODOLOGY

The test structure shown in Figure 1.8 is a five-inch broadside differential angular coupled segment that uses a core and pre-preg dielectric with a relative permittivity of 3.7 and a loss tangent of 0.025 at 1 GHz. To prove the modeling concept divide the overall coupled section (five inches) into multiple parallel coupled and non-parallel coupled parts, the parallel and non-parallel parts are generated using Full-Wave solvers. The overall coupled section is also solved using the Full-Wave FEM solver to compare it against the cascaded block-by-block model. The coupled model consists of different routings with different coupling angles, which is close to a real scenario. The geometry contains different crossover angles with the largest angle at 60 degree and smallest at 30 degree. The small blocks are cascaded together to build a block-by-block coupled S-parameter matrix. The S-parameters of the Full-Wave FEM model and block-by-block model are then compared. The correlation between the THRU and near-end crosstalk (NEXT) S-parameters is good for both approaches from a frequency domain point of view, as seen in Figure 1.9. A step input of the 1V peak-peak with a rise/fall time of 30 ps is applied to the aggressor trace to obtain the NEXT step response at the victim's receiver.

The step responses of the Full-Wave FEM model for the entire coupled section are compared against the block-by-block model of the coupled section, as seen Figure 1.10. The correlation between the block-by-block model and the Full-Wave FEM model of the entire coupled section is very good in both the time and frequency domains.

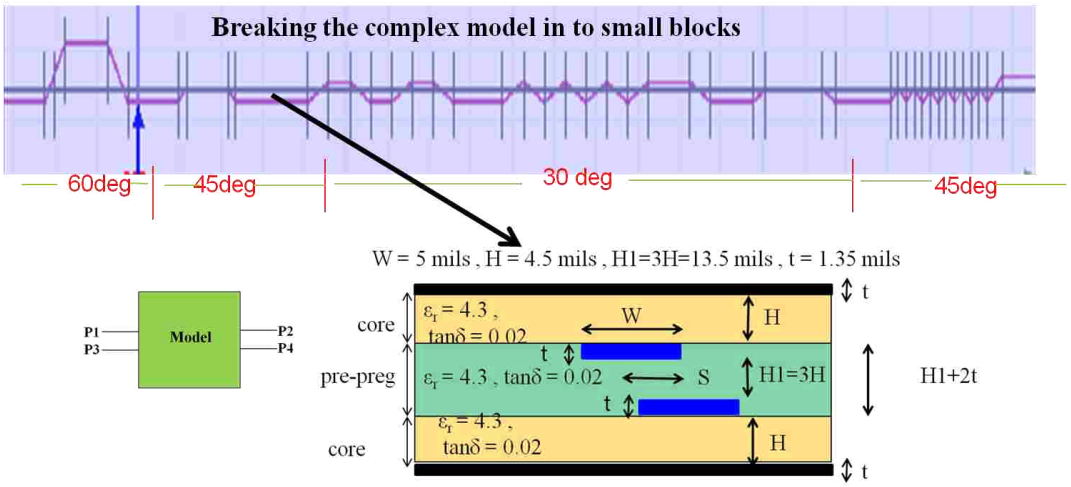

Figure 1.8. Geometry and stack-up of the end-to-end complex coupled section

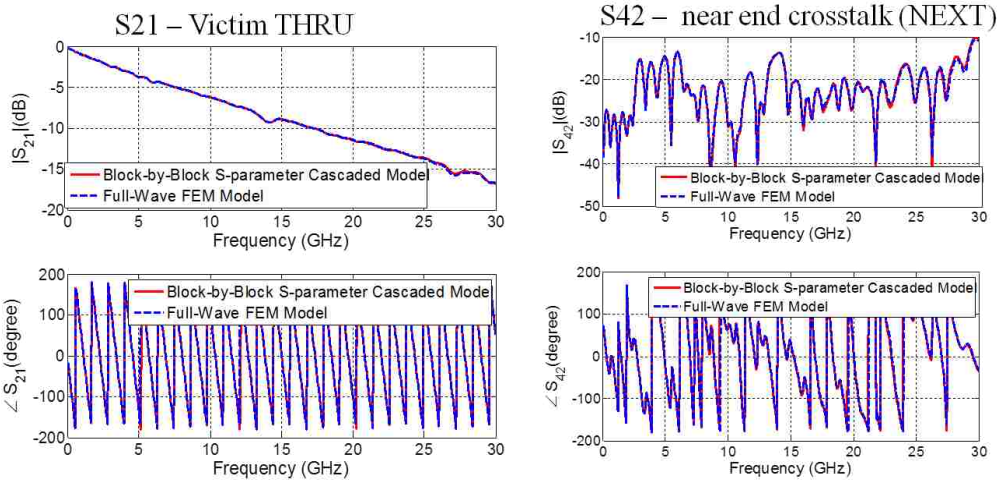

Figure 1.9. Comparison of the THRU and NEXT frequency domain responses for the Full-Wave model and the block-by-block model of the end-to-end coupled section

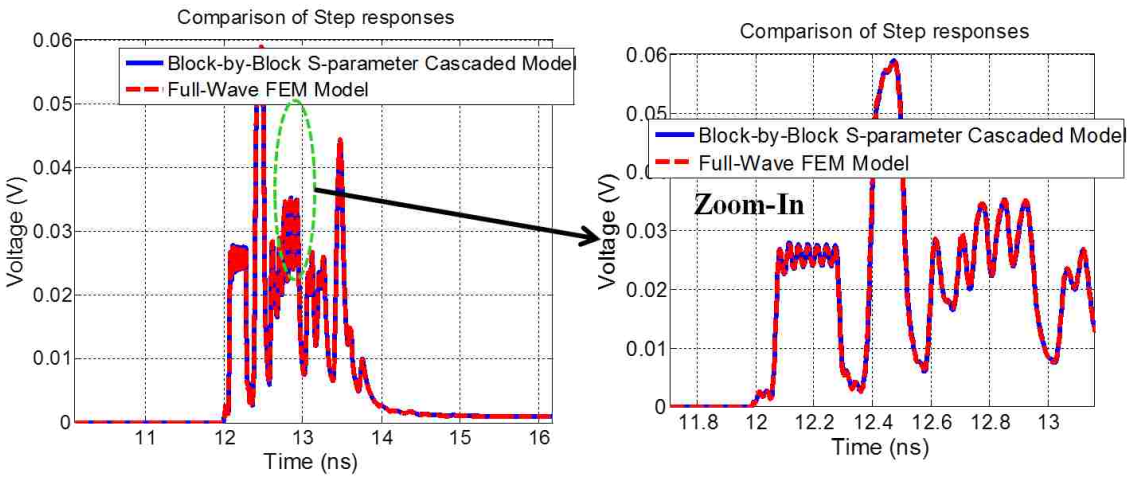

Figure 1.10. The comparison of the NEXT time domain response of the Full-Wave model and the block-by-block model of the end-to-end coupled section

The step responses of the Full-Wave FEM model for the entire coupled section correlate very well against the block-by-block model of the coupled section. The time-domain correlation of step response implies correlation of impulse response. The impulse response dictates the crosstalk response and its impact on the receiver eye opening. Majority of the statistical analysis tools take impulse as an input to generate the BER eye contours. Since the impulse responses of the Full-Wave FEM model and block-by-block model of entire coupled section correlate very well, translates to good correlation of BER eye contours.

A single-ended input of a 500 mV peak-peak with a rise/fall time of 35ps at a data rate of 10 Gbps is used on both the aggressor and victim for the complex broadside for a 5 -inch long line coupled section described in Figure. 1.8. The NEXT impact on the receiver eye opening is compared in Figure 1.11. The eye width and eye height of the block-by-block and Full-Wave models of the end-to-end complex broadside coupled segment are compared at 10 Gbps in Table 1.1.

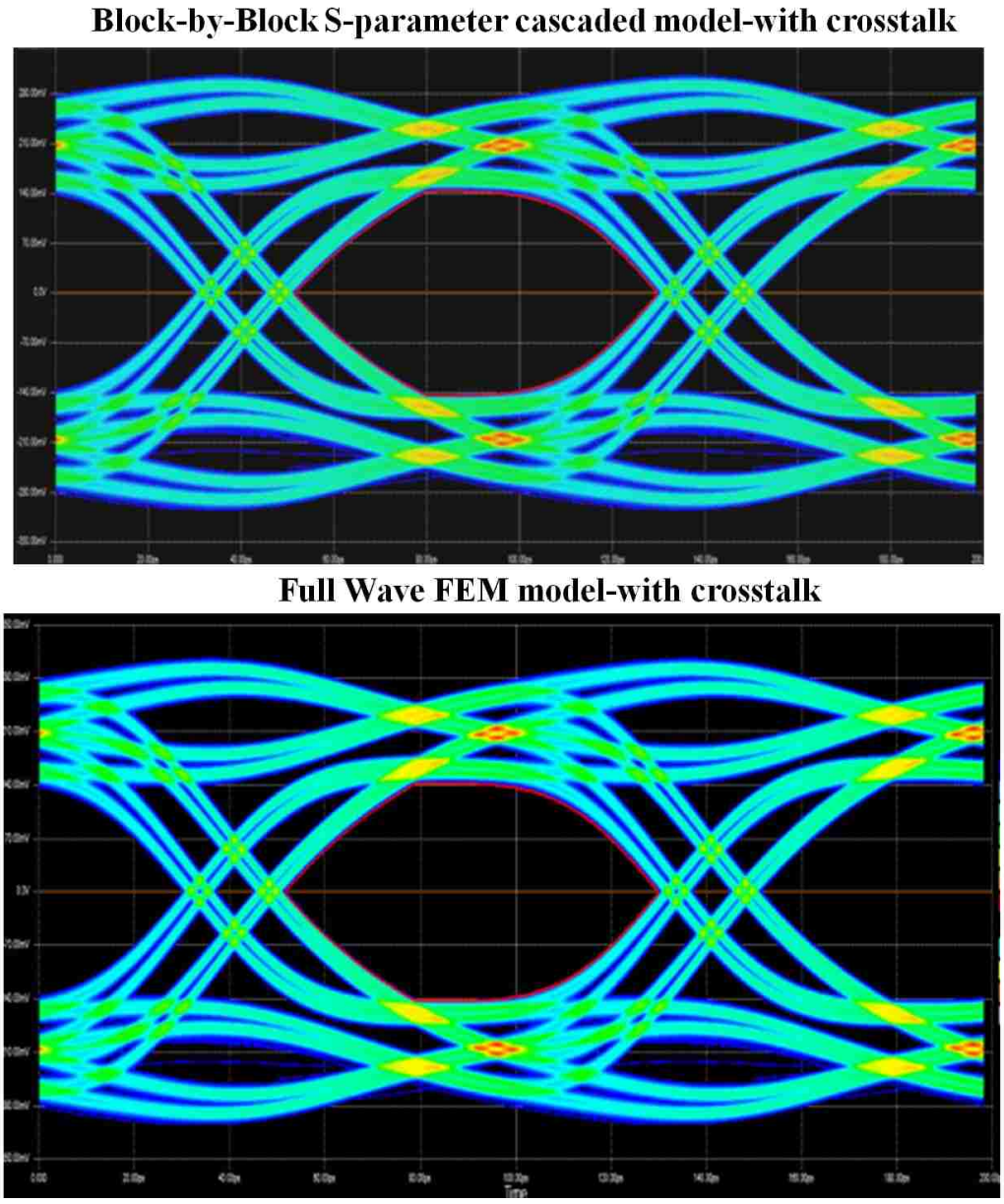

Figure 1.11. Comparison of the NEXT impact on the receiver eye opening the Full-Wave model and the block-by-block model of the end-to-end coupled section

The differences in eye height and eye width in the block-by-block model and the Full-Wave model of entire end-to-end coupled section are within 1%. The divide-and-

conquer approach of the big crosstalk analysis problem into multiple smaller blocks and analysis yielded results within 1% of the end-to-end Full-Wave FEM model.

Table 1.1. Comparison of the eye diagram results of block-by-block model with Full-Wave FEM model of entire coupled section

Model	EH(mV)	EW(ps)
Block-by-Block without crosstalk	331.1	92.5
Full-Wave FEM Model without crosstalk	331.8	92.7
Block-by-Block with crosstalk	275.1	78
Full-Wave FEM Model with crosstalk	274	78.2

1.4. APPLICATION OF CROSSTALK METHODOLOGY TO COMPLEX COUPLED SECTION IN PRACTICAL PCBS

The end-to-end assembly model of the victim to multiple aggressor coupling for a real board is shown in Figure 1.12. In this design example, eight broadside aggressors and two edge coupled aggressors are selected based on the vicinity of the aggressor to the victim lanes. The overall length of the end-to-end channel is 21 inches. The stack-up parameters are: W is 5 mils, H is 3.8 mils, H1 is 12 mils, S is 5.5 mils, S1 is 14 mils, t1 is 1.3 mils, and t2 is 2.6 mils. The core and pre-preg dielectric with a relative permittivity of 3.7 and 4.3 and a loss tangent of 0.025 at 1 GHz are used as dielectric media. The broadside coupling is only on the backplane channel. Based on the confidence gained from the validation of the methodology in the previous section, the Full-Wave FEM

model of the end-to-end link is not simulated as the model is very big and takes an enormous amount of simulation time, which is not feasible for engineering timelines. The broadside coupled aggressors create a near-end crosstalk (NEXT) issue as the signal direction in the aggressors is the opposite of the victim lane. The edge coupled aggressors create a far-end crosstalk (FEXT) issue as the signal direction is the same as the victim lane. The edge coupled aggressors and victim link belong to the same signal BUS (example data) whereas the broadside aggressors belong to different signal BUSs (example address).

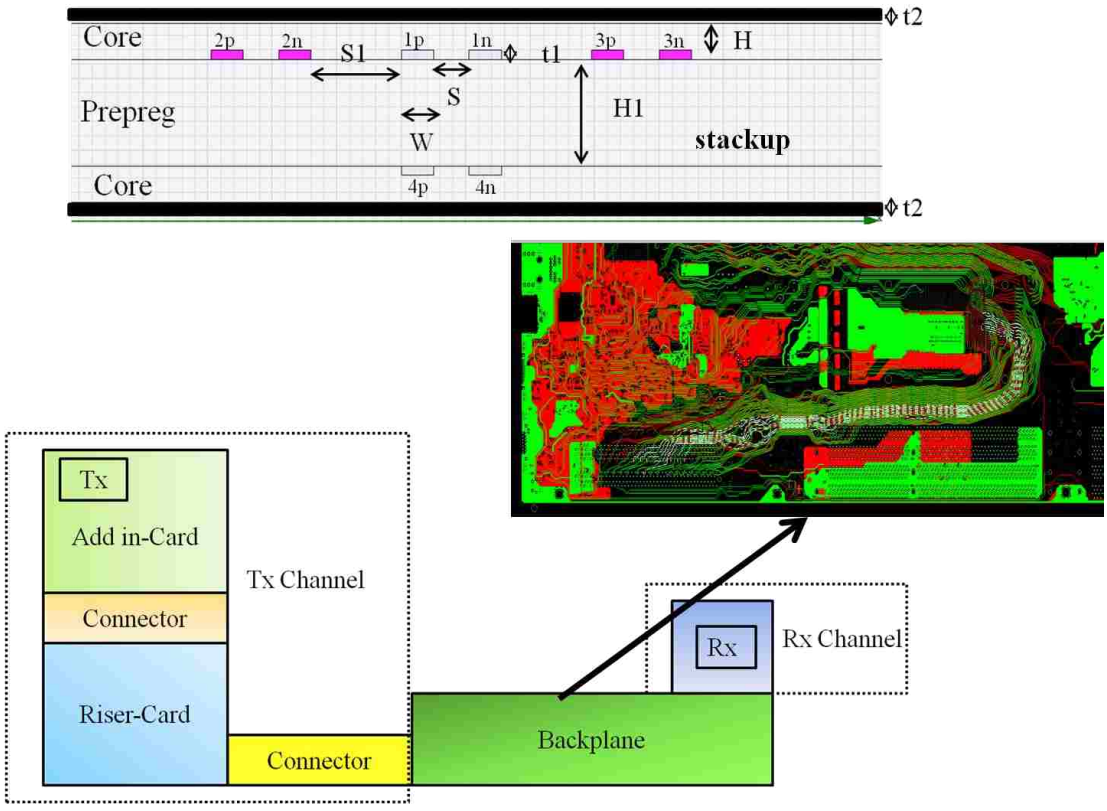

Figure 1.12. Geometry and stack-up of the end-to-end complex coupled section in practical PCB

The schematic for the end-to-end signal link path consists of a Tx channel, backplane, and Rx channel is shown in Figure 1.13. The Tx channel consists of a transmitter die, package, via, and traces on PCI-E add in card attached to the riser card through PCI-E connector seen in Figure 1.12. The riser card is connected to the backplane through the connector. The broadside coupling is present in the backplane channel. The Rx channel consists of a receiver die, package, via, and traces connected to the backplane channel. The CPU is the receiver in this example. The edge-side coupling is throughout the entire signal link path. The coupled length of the Tx channel is 7.5 inches, the backplane channel is 11.5 inches, and the Rx channel is 2.05 inches. The PCI-E gen3 is running at a speed of 8 Gbps. The THRU of the signal link path, NEXT from one of eight broadside coupled aggressors, and the FEXT from one of the two edge coupled aggressors is shown in Figures 1.14–1.16.

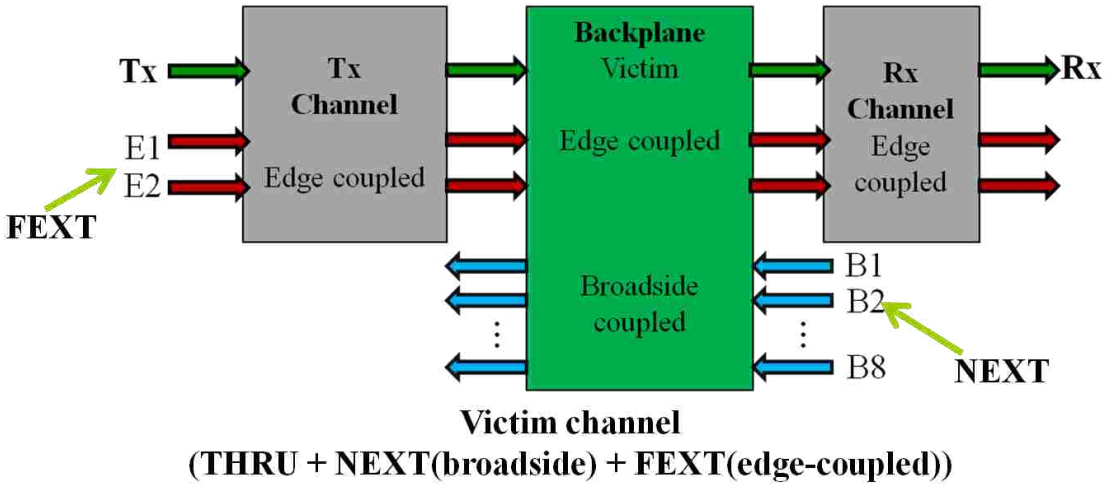

Figure 1.13. Schematic of the end-to-end complex coupled section

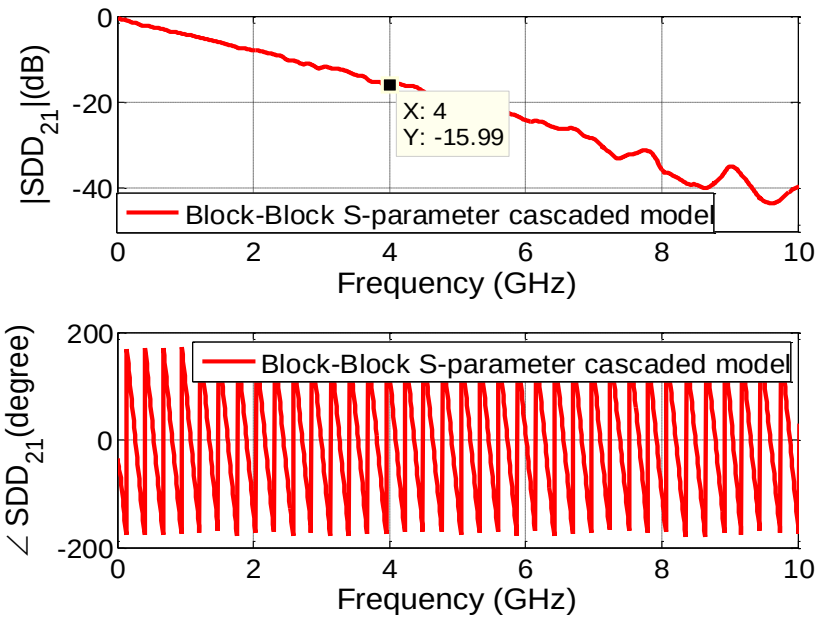

Figure 1.14. The THRU of the victim channel

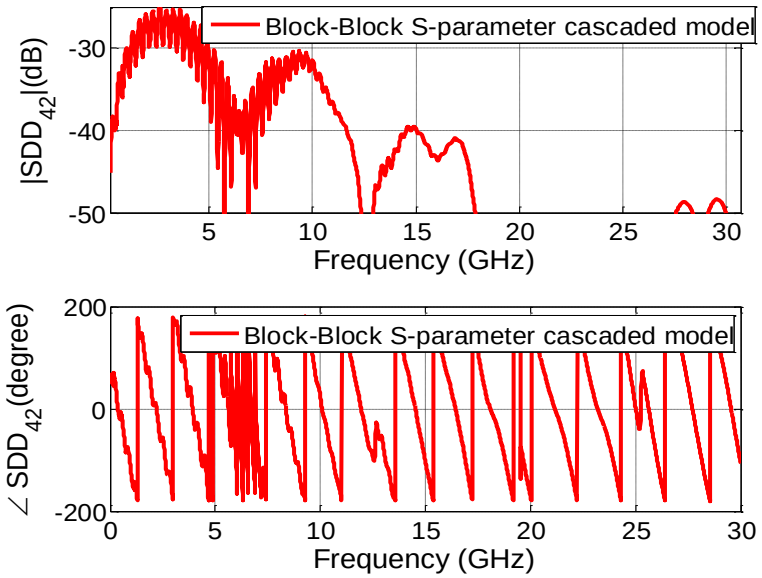

Figure 1.15. The NEXT of the broadside coupled aggressor channel

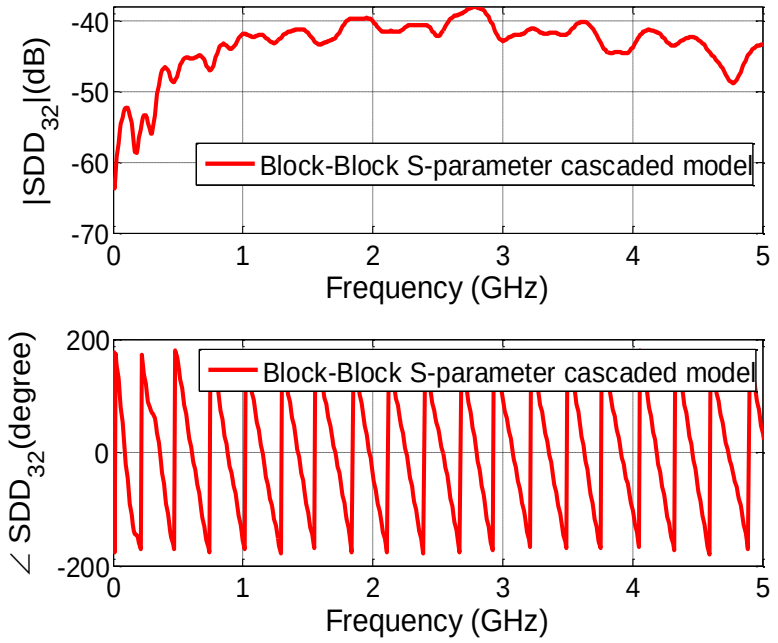

Figure 1.16. The FEXT of the edge coupled aggressor channel

A differential input of 500 mV peak-peak with a rise/fall time of 20ps at a data rate of 8 Gbps is used on both the aggressor and victim for the complex broadside coupled section described in Figure 1.12, which shows a 21-inch long line. The data pattern on the victim channel is PRBS-18, whereas all the aggressor channels are fed PRBS-9 patterns. Due to the loss in the THRU channel, there is no eye opening without any kind of Tx equalization. The eye at the receiver is opened by applying 6 dB de-emphasis. The eye opening before and after equalization is shown in Figure 1.17. The input and output waveforms after applying de-emphasis is shown in Figure 1.18.

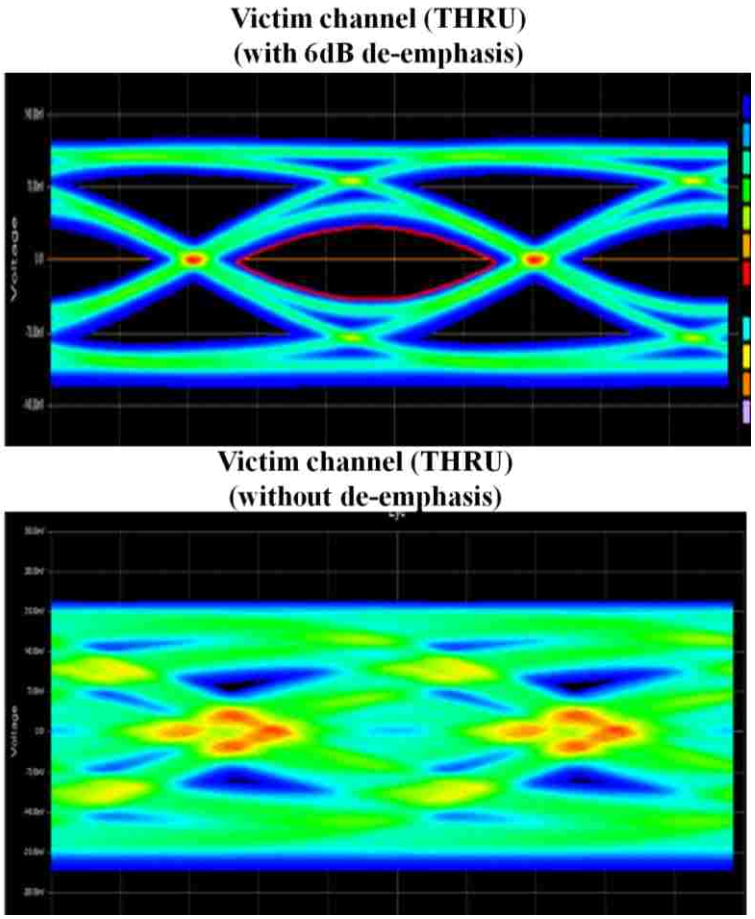

Figure 1.17. Eye opening before and after equalization of THRU channel

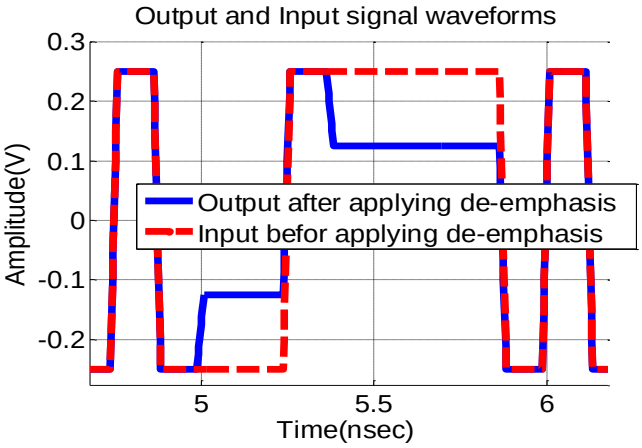

Figure 1.18. The impact of 6 dB de-emphasis on the input signal

The NEXT impact on the receiver eye opening is shown in Figure 1.19 and Figure 1.20. The impact on eye opening due to NEXT from the broadside coupled aggressors and the FEXT from the edge coupled aggressors is shown in Table 1.2.

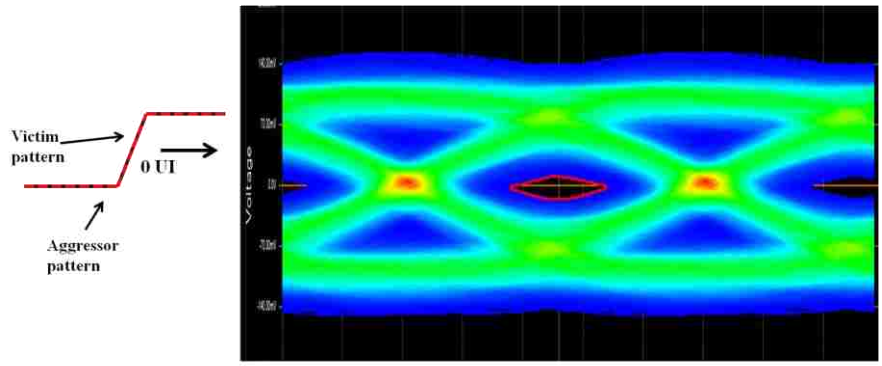

$$UI = \frac{1}{data - rate} = \frac{1}{8 \times 10^9} = 125ps$$

Figure 1.19. The impact of the NEXT and the FEXT on the receiver eye opening for a 0UI skew

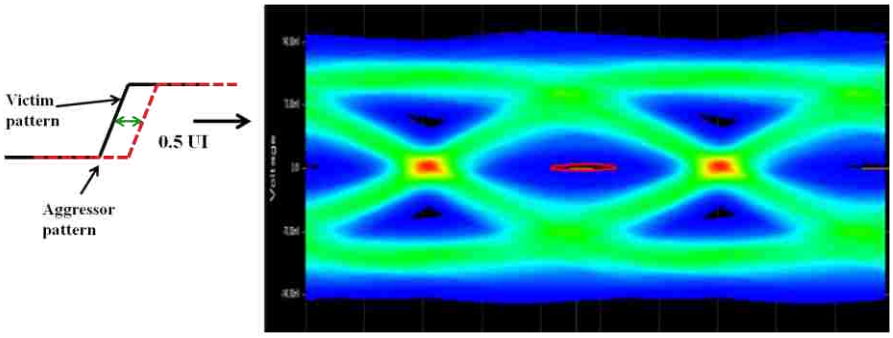

$$UI = \frac{1}{data - rate} = \frac{1}{8 \times 10^9} = 125ps$$

Figure 1.20. The impact of the NEXT and the FEXT on the receiver eye opening for a 0.5UI skew

The victim channel without any crosstalk requires a 6 dB de-emphasis gain to open the eye contour. No de-emphasis is applied on the aggressors. The eye width of the BER contour shrinks from 91ps to 35ps in the presence of eight broadside aggressors and two edge coupled aggressors. This is a significant reduction in the jitter budget that allows the designer to accommodate the NEXT and FEXT crosstalk impact on the BER contour at an 8 Gbps data rate.

Table 1.2. The impact of the NEXT and the FEXT on the receiver eye opening

	Aggressors activated	Timing relation	Eye Width (ps)
Without Crosstalk	None		**91**
With Crosstalk	8 broadside (NEXT) + 2 edge coupled (FEXT)	0UI	**35**
With Crosstalk	8 broadside (NEXT) + 2 edge coupled (FEXT)	0.5UI	28
With Crosstalk	8 broadside (NEXT)	0UI	41
With Crosstalk	8 broadside (NEXT)	0.5UI	38
With Crosstalk	2 edge coupled (FEXT)	0UI	88
With Crosstalk	2 edge coupled (FEXT)	0.5UI	90

The timing relationships studied here are in-phase and out-of-phase crosstalk. The impact of the NEXT from the broadside coupled aggressors on the BER eye contour is severe compared to the FEXT from the edge coupled aggressors. The 180 degree out-of-phase crosstalk impacts the eye height more than the eye width. A thru channel without any crosstalk from the aggressors requires 6 dB de-emphasis to open the eye. The

aggregate crosstalk impact of two edge coupled aggressors and eight broadside coupled aggressors on the eye width of the BER eye contour opening is severe compared to when only two edge coupled aggressors are used.

1.5. DESIGN IMPLICATIONS OF PROPOSED METHODOLOGY

The proposed methodology can be applied to identify the worst-case crosstalk affected sections in the overall coupled link containing multiple sections. When analyzing different coupling sections, the aggressors in only one of the section is enabled and all other sections are disabled to identify the impact from the section under observation. The flowchart of the methodology is illustrated in Figure 1.21. This will help the designer to specifically target the crosstalk sensitive areas in the design.

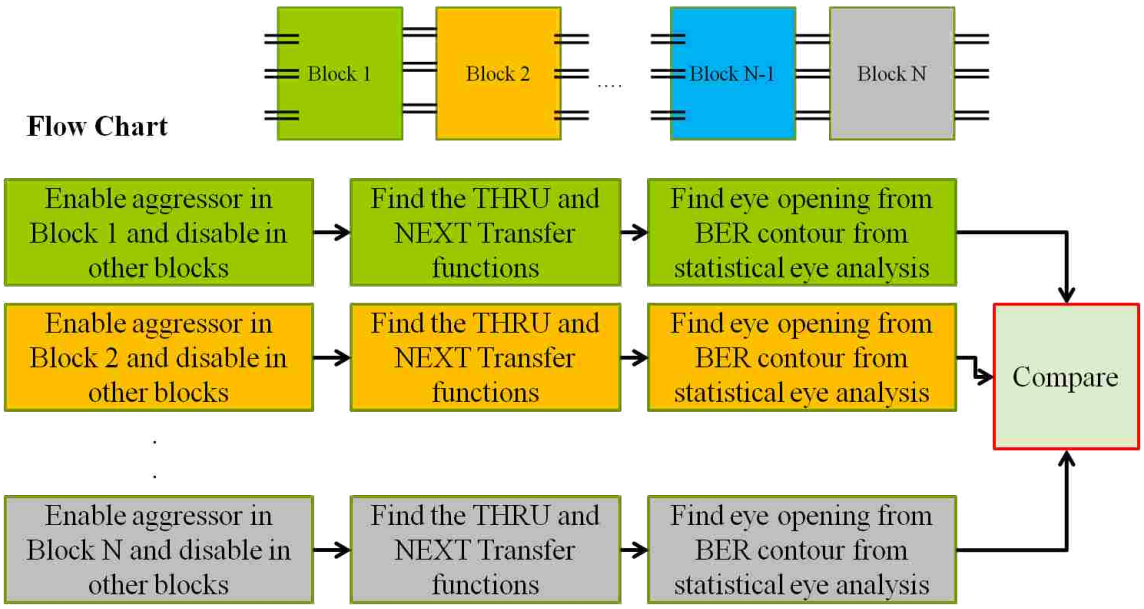

Figure 1.21. The flowchart to locate the crosstalk sensitive sections in the entire link path

1.6. CONCLUSIONS

This paper introduces a crosstalk methodology that can alleviate the modeling burden of an entire end-to-end coupled link. The entire coupled link is broken into smaller unique parts, which fall into one of three library part types. The smaller manageable parts can be simulated using Full-Wave solvers, the Eq P.U.L RLGC approach, or the PEEC model. The smaller parts are cascaded in a block-by-block fashion to generate the S-parameter of the entire coupled link path. The divide-and-conquer approach is validated by comparing the frequency and time domain results of the block-by-block and Full-Wave models of the entire coupled link. The proposed methodology is applied to the victim channel in the presence of 10 aggressor channels that were chosen from a practical PCB of the data center server. The proposed methodology serves as a powerful tool to test the sensitive data channels crosstalk from nearby data channels without the burden of using huge Full-Wave models and the simulation overhead by utilizing statistical eye analysis. The proposed methodology can help designers determine the crosstalk impact and locate the crosstalk-sensitive areas in the design.

2. QUANTIFYING THE IMPACT OF FEXT ON EYE MARGIN FOR COUPLED LINES IN INHOMOGENOUS MEDIA

2.1. INTRODUCTION

Increases in printed circuit board (PCB) costs are leading to denser routing of high speed signal traces and to the use of low cost dielectric materials that are not homogeneous for high volume manufacturing. This, in turn, is increasing crosstalk among the traces. The crosstalk between the coupled traces in adjacent layers and the same layers is becoming an important factor to take into account as the signal speeds increase. The dielectric media surrounding the traces are not homogeneous and this increases the Far End Crosstalk (FEXT) and insertion loss (THRU), thereby reducing the signal to noise ratio of the high speed link. Designers must not ignore the difference in dielectric materials used for pre-preg and core dielectrics. The difference in dielectric material properties makes the medium inhomogeneous, resulting in different modal velocities in coupled lines and creating nulls in the insertion loss profile. The inhomogeneity in the media also increases the Far End Crosstalk (FEXT) at the nulls of insertion loss. In this paper, the coupling is considered between high speed signal traces in adjacent layers and the same layers. As the signaling speeds increase from generation to generation, the need to estimate the impact of crosstalk on the overall system bit error rate (BER) becomes important.

Previously, work on the FEXT impact in inhomogeneous media has focused on single coupled microstrips and striplines [12-26]. Simple crosstalk relations were developed only for single ended coupled lines. Currently, high speed links use differential signaling schemes, so crosstalk relations developed for single-ended coupled lines cannot be used to derive meaningful guidelines. Solutions to mitigate the FEXT were developed for coupled microstrip lines in [27-32]. Some of the solutions proposed might not be applicable for low cost/high volume manufacturing processes. Other crosstalk mitigation solutions have mainly focused on reducing the inhomogeneity in the media or on reducing the coupling between the signal traces, but no mathematical model to predict the crosstalk based on the physics of coupling has been derived. Formulations for crosstalk estimation in the literature [12] either assumed lossless media or homogeneous media or

they are too complex for any real insight into the coupling physics useful for designers. The frequencies considered were not high compared to current data speeds. The formulations and solutions do not deal with more than 3-conductor transmission line systems. Formulations developed for more than 3-condcutor systems in [15] are rigorous, but are too complex to derive any meaningful relation between the coupling physics, PCB cross section, and source/load terminations. The guidelines provided previously to mitigate the impact of FEXT are not based on the BER metric. The formulations did not provide any means to estimate the impact on BER eye contour.

The work presented in this paper addresses the above issues and also provides an impulse response derived from FEXT transfer function to estimate the impact on the BER eye opening by using statistical analysis for single-ended and differential lines. The mode cancelation effect of different propagating modes and its impact on crosstalk response observed in the presence of inhomogeneous media for single-ended and differential lines is explained using analytical formulations and validated in Sections 2.2 and 2.3. Robustness of the differential coupled lines to FEXT is explained in Section 2.4. The impact on eye opening from FEXT in inhomogeneous media at various signaling speeds for differential lines is studied in Section 2.5. Guidelines based on horizontal eye opening of the statistical bit error rate (BER) eye contour are given in Section 2.6 to help the designer at different data rates. Section 2.7 summarizes the paper.

2.2. CLOSED FORM EXPRESSION FOR CROSSTALK IN COUPLED LINES DUE TO INHOMOGENEOUS MEDIA

The analytical expression of FEXT and the insertion loss profile for (N+1)-conductor transmission line structure shown in Figure 2.1 can be derived by starting from telegrapher equations [13,14] along with boundary conditions at the source and load terminals for the transmission lines.

$$\frac{d}{dz}\left[\hat{V}_z\right] = -\left[\hat{Z}\right]\left[\hat{I}_z\right] \tag{29}$$

$$\frac{d}{dz}\left[\hat{I}_z\right] = -\left[\hat{Y}\right]\left[\hat{V}_z\right] \tag{30}$$

where,

$$\hat{V}_z = \begin{bmatrix} V_1(z) \\ V_2(z) \\ . \\ V_n(z) \end{bmatrix} \quad , \quad \hat{I}_z = \begin{bmatrix} I_1(z) \\ I_2(z) \\ . \\ I_n(z) \end{bmatrix}$$

$$\hat{Z} = \hat{R} + j\omega\hat{L}, \hat{Y} = \hat{G} + j\omega\hat{C}$$

$$\hat{R}, \hat{L}, \hat{G}, \hat{C} \quad are \quad per-unit-length \ symmetric \ matrices$$

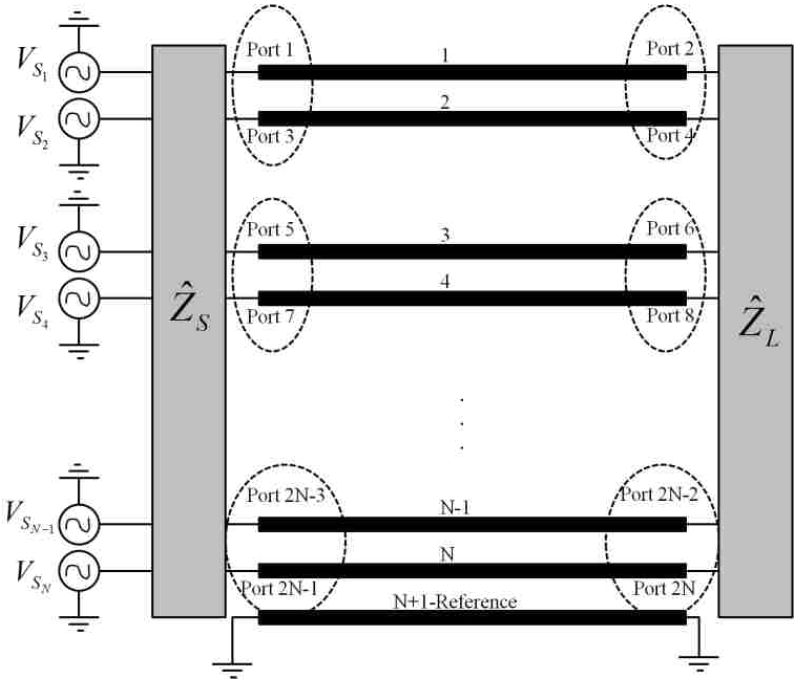

Figure 2.1. N+1-conductor transmission line schematic with arbitrary source and load terminations

The voltage wave equation can be derived from equations (29) and (30)

$$\frac{d^2}{dz^2}\left[\hat{V}_z\right] = \left[\hat{Z}\right]\left[\hat{Y}\right]\left[\hat{V}_z\right] \tag{31}$$

The voltage wave equation can be decoupled into a modal voltage wave equation using the similarity transformation

$$\hat{V}_z = \hat{T}_V \hat{V}_z^m \tag{32}$$

where $\hat{T}_V$ is a matrix whose columns are eigenvectors that diagonalize the $\hat{Z}\hat{Y}$ matrix product.

The general solution for modal voltages can be written in the form

$$\left[\hat{V}_z^m\right] = e^{-\hat{\gamma} z}\left[\hat{V}^{m^+}\right] + e^{\hat{\gamma} z}\left[\hat{V}^{m^-}\right] \tag{33}$$

where,

$$e^{\pm\hat{\gamma} z} = \begin{bmatrix} e^{\pm\gamma_{m_1} z} & 0 & 0 & 0 \\ 0 & e^{\pm\gamma_{m_2} z} & 0 & 0 \\ 0 & 0 & . & 0 \\ 0 & 0 & 0 & e^{\pm\gamma_{m_n} z} \end{bmatrix}$$

$$\hat{V}^{m^+} = \begin{bmatrix} V_{m_1}^+ \\ V_{m_2}^+ \\ . \\ V_{m_n}^+ \end{bmatrix} \quad , \quad \hat{V}^{m^-} = \begin{bmatrix} V_{m_1}^- \\ V_{m_2}^- \\ . \\ V_{m_n}^- \end{bmatrix}$$

$$\left[\hat{T}_V\right]^{-1}\left[\hat{Z}\right]\left[\hat{Y}\right]\left[\hat{T}_V\right]=\left[\hat{T}_I\right]^{-1}\left[\hat{Y}\right]\left[\hat{Z}\right]\left[\hat{T}_I\right]=\hat{\gamma}^2$$

$$\hat{\gamma}^2=\begin{bmatrix}\gamma_{m_1}^2 & 0 & 0 & 0\\ 0 & \gamma_{m_2}^2 & 0 & 0\\ 0 & 0 & . & 0\\ 0 & 0 & 0 & \gamma_{m_n}^2\end{bmatrix}$$

$$\hat{\gamma}=\hat{\alpha}+j\hat{\beta}$$

where γ is the propagation constant matrix, α is the attenuation constant matrix, and β is the phase constant matrix.

The line voltages can be written in terms of modal voltages as

$$\left[\hat{V}_z\right]=\hat{T}_V\left(e^{-\hat{\gamma}z}\left[\hat{V}^{m^+}\right]+e^{\hat{\gamma}z}\left[\hat{V}^{m^-}\right]\right) \tag{34}$$

Substituting equation (34) in (28), the line currents can be written in terms of modal voltages as

$$\left[\hat{I}_z\right]=\hat{Z}_C\hat{T}_V\left(e^{-\hat{\gamma}z}\left[\hat{V}^{m^+}\right]-e^{\hat{\gamma}z}\left[\hat{V}^{m^-}\right]\right) \tag{35}$$

where, $\hat{Z}_C$ is the characteristic impedance matrix given by

$$\left[\hat{Z}_C\right]=\left(\left[\hat{Z}\right]^{-1}\left[\hat{T}_V\right]\hat{\gamma}\left[\hat{T}_V\right]^{-1}\right)^{-1} \tag{36}$$

Assuming no independent sources at the load terminals, the boundary conditions at the source and load are

$$\hat{V}_{z=0} = \hat{V}_S - \hat{Z}_S \hat{I}_{z=0} \tag{37}$$

$$\hat{V}_{z=l} = \hat{Z}_L \hat{I}_{z=l} \tag{38}$$

Substituting the voltage and current solutions in the boundary conditions

$$\begin{bmatrix} \left(I + \hat{Z}_S \hat{Y}_C\right)\hat{T}_V & \left(I - \hat{Z}_S \hat{Y}_C\right)\hat{T}_V \\ \left(I - \hat{Z}_L \hat{Y}_C\right)\hat{T}_V e^{-\hat{\gamma} L} & \left(I + \hat{Z}_L \hat{Y}_C\right)\hat{T}_V e^{\hat{\gamma} L} \end{bmatrix} \begin{bmatrix} \hat{V}_m^+ \\ \hat{V}_m^- \end{bmatrix} = \begin{bmatrix} \hat{V}_s \\ 0 \end{bmatrix} \tag{39}$$

Rearranging the equation (39) by defining matrices A and B as

$$[A][B] \begin{bmatrix} \hat{V}_m^+ \\ \hat{V}_m^- \end{bmatrix} = \begin{bmatrix} \hat{V}_s \\ 0 \end{bmatrix} \tag{40}$$

where,

$$[A] = \begin{bmatrix} \left(I + \hat{Z}_S \hat{Y}_C\right)\hat{T}_V & 0 \\ 0 & \left(I + \hat{Z}_L \hat{Y}_C\right)\hat{T}_V e^{\hat{\gamma} L} \end{bmatrix}$$

$$[B] = \begin{bmatrix} I & \left(\left(I + \hat{Z}_S \hat{Y}_C\right)\hat{T}_V\right)^{-1}\left(I - \hat{Z}_S \hat{Y}_C\right)\hat{T}_V \\ \left(\left(I + \hat{Z}_L \hat{Y}_C\right)\hat{T}_V e^{\hat{\gamma} L}\right)^{-1}\left(I - \hat{Z}_L \hat{Y}_C\right)\hat{T}_V e^{-\hat{\gamma} L} & I \end{bmatrix}$$

$$\hat{V}_S = \begin{bmatrix} V_{S_1} \\ V_{S_2} \\ . \\ V_{S_N} \end{bmatrix}$$

Defining the reflection coefficients at the source and load as $\hat{\Gamma}_{source}$ and $\hat{\Gamma}_{load}$

$$\hat{\Gamma}_{source} = -\left(I + \hat{Z}_S \hat{Y}_C\right)^{-1}\left(I - \hat{Z}_S \hat{Y}_C\right) \tag{41}$$

$$\hat{\Gamma}_{load} = -\left(I + \hat{Z}_L \hat{Y}_C\right)^{-1}\left(I - \hat{Z}_L \hat{Y}_C\right) \tag{42}$$

The matrix $[B]$ can be rewritten using equations (41) and (42)

$$[B] = \begin{bmatrix} I & -\hat{T}_V{}^{-1}\hat{\Gamma}_{source}\hat{T}_V \\ -\left(e^{\hat{\gamma} L}\right)^{-1}\hat{T}_V{}^{-1}\hat{\Gamma}_{load}\hat{T}_V e^{-\hat{\gamma} L} & I \end{bmatrix} \tag{43}$$

Equation (39) is broke down in to two simultaneous equations as

$$\left(I + \hat{Z}_S \hat{Y}_C\right)\left(\hat{T}_V \hat{V}_m^+ - \hat{T}_V\left(\hat{T}_V{}^{-1}\hat{\Gamma}_{source}\hat{T}_V\right)\hat{V}_m^-\right) = \hat{V}_s \tag{44}$$

$$-\left(I + \hat{Z}_L \hat{Y}_C\right)\left(\hat{T}_V e^{\hat{\gamma} L}\left(\left(e^{\hat{\gamma} L}\right)^{-1}\hat{T}_V{}^{-1}\hat{\Gamma}_{load}\hat{T}_V e^{-\hat{\gamma} L}\right)\hat{V}_m^+ + \hat{T}_V e^{\hat{\gamma} L}\hat{V}_m^-\right) = 0 \tag{45}$$

Equation (45) can be solved to give

$$\hat{V}_m^- = B\hat{V}_m^+ \tag{46}$$

where,

$$B = \left(\left(e^{\hat{\gamma} l}\right)^{-1}\hat{T}_V{}^{-1}\hat{\Gamma}_{load}\hat{T}_V e^{-\hat{\gamma} l}\right)$$

Substitute equation (46) in to equation (44) to get

$$\hat{V}_m^+ = \left(\left(\left(I + \hat{Z}_S \hat{Y}_C\right)\hat{T}_V\right)A\right)^{-1}\hat{V}_S \tag{47}$$

where,

$$A = \left(I - \left(\hat{T}_V{}^{-1}\hat{\Gamma}_{source}\hat{T}_V\right)B\right)$$

The line voltages can be obtained by substituting equations (46) and (47) into equation (34)

$$\left[\hat{V}_z\right] = \hat{T}_V e^{-\hat{\gamma} z}\left(I + \hat{\Gamma}_V(z)\right)\hat{V}_m^+ \tag{48}$$

where $\hat{\Gamma}_V(z)$ is equivalent voltage reflection coefficient along the Tx line at any arbitrary position z.

$$\hat{\Gamma}_V(z) = \left(\left(e^{-\hat{\gamma} z}\right)^{-1} e^{\hat{\gamma} z}\right)\left(\left(e^{\hat{\gamma} l}\right)^{-1}\hat{T}_V{}^{-1}\hat{\Gamma}_{load}\hat{T}_V e^{-\hat{\gamma} l}\right)$$

The metric quantifying the impact of FEXT on the THRU can be formulated as the ratio of the FEXT and THRU voltages

$$XTK_{metric} = \frac{FEXT}{THRU} \tag{49}$$

For single-ended coupled lines, the FEXT and THRU voltages are given as

$$FEXT_{Single} = \left(V_{z=l}^2\right) \tag{50}$$

$$THRU_{Single} = \left(V_{z=l}^1\right) \tag{51}$$

$$XTK_{Single} = \frac{\left(V_{z=l}^2\right)}{\left(V_{z=l}^1\right)} \tag{52}$$

For differential coupled lines, the differential FEXT and THRU voltages are given as

$$FEXT_{diff} = \left(V_{z=l}^{3} - V_{z=l}^{4}\right) \tag{53}$$

$$THRU_{diff} = \left(V_{z=l}^{1} - V_{z=l}^{2}\right) \tag{54}$$

$$XTK_{diff} = \frac{\left(V_{z=l}^{3} - V_{z=l}^{4}\right)}{\left(V_{z=l}^{1} - V_{z=l}^{2}\right)} \tag{55}$$

A crosstalk metric based on horizontal eye opening at specified BER can be defined using the FEXT and THRU voltage transfer functions to generate the impulse responses to obtain the statistical bit-error-rate(BER) eye contour shown in Figure 2.2, as

$$XTK - impact\% = \frac{EW_{without-xtk} - EW_{with-xtk}}{EW_{without-xtk}} \times 100\% \tag{56}$$

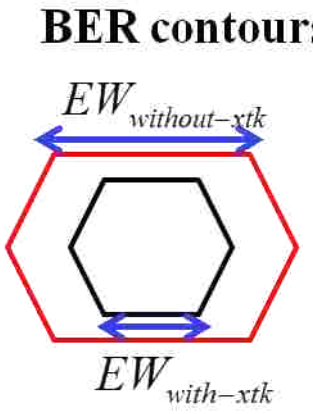

Figure 2.2. The FEXT metric definition based on BER eye contour

The crosstalk metric defined in equation (49) has one to one mapping relation with the crosstalk metric defined in equation (56). The reason being that the impulse response required to generate the BER eye contours is obtained by taking inverse Fourier transform of voltage transfer function. Inverse Fourier transform is a linear operator and so the transformation between the two crosstalk metric is also linear.

A 3-conductor transmission line system representing two single-ended coupled lines will have two propagating modes. In inhomogeneous media, the modal velocities of the two propagating modes differ. A single-ended aggressor trace excited with voltage of polarity (+), can have two possible polarities of voltages on the victim trace, (+) and (-), to conserve the total energy in the system. The two columns of the Tv matrix, whose elements have the signs (+,+) and (+,-), are the two modes 1 and 2 that determine the FEXT and THRU characteristics. The FEXT voltage has a maxima and the THRU voltage has a minima when the phase difference between the two propagating modes is an integer multiple of 180^0.

Equation (48) can be written as a superposition of two independent mode voltages. The FEXT voltage at the load end can be written as

$$FEXT = e^{-\gamma_1 l}\left(C - e^{-(\gamma_2-\gamma_1)l}D\right) \tag{56}$$

where C and D are constants obtained from equation (48) after re-arrangement. The FEXT voltage at the receiver given in equation (56) has a maximum value when

$$e^{-(\gamma_2-\gamma_1)l} = e^{(\alpha_1-\alpha_2)l}e^{j(\beta_1-\beta_2)l} = -1 \tag{57}$$

$$e^{j(\beta_1-\beta_2)l} = -1 \Rightarrow \left|(\beta_1-\beta_2)l\right| = (2n-1)\pi \quad n = 1,2,... \tag{58}$$

$$2\pi f\left|\left(\frac{l}{v_1}-\frac{l}{v_2}\right)\right| = (2n-1)\pi \quad n = 1,2,.. \tag{59}$$

where,

$$\hat{\gamma} = \begin{bmatrix} \gamma_1 & 0 \\ 0 & \gamma_2 \end{bmatrix}$$

$$\beta_1 = \frac{2\pi f}{v_1} \quad , \quad \beta_2 = \frac{2\pi f}{v_2}$$

A 5-conductor transmission line system representing two differential coupled lines can have four propagating modes. Aggressor differential line traces are excited with complimentary voltages with polarities (+,-). Two possible polarities of voltages on victim differential line traces are (+,-) and (-,+), in order to conserve the total energy in the system. The four columns of the T_v matrix determine the four possible independent modes. The two columns of the T_v matrix, whose elements have the signs (+,-,+,-) and (+,-,-,+), are the two modes 1 and 2 that determine the FEXT and THRU characteristics. The FEXT voltage has a maxima and the THRU voltage has a minima when the phase difference between these two propagating modes is an integer multiple of 180^0. The frequency where this occurs can be computed for the two modes of interest using similar equations in the form of equations (56)-(59).

The inhomogeneity percentage of the dielectric media is computed as

$$INHOMOGENEITY\% = \frac{\varepsilon_{pre-preg} - \varepsilon_{core}}{\varepsilon_{core}} \times 100 \qquad (60)$$

The single-ended coupled lines test structure shown in Figure 2.3 is a 10 inch complete broadside coupled model using core dielectric with relative permittivity of 3.7 and loss tangent of 0.025 at 1GHz. The pre-preg dielectric constant is set 15% higher than the core dielectric constant. The lossless case is used to simplify the analysis without losing sight of the coupling physics. Five test cases with different trace widths of 3, 5, 8, 10, and 20 mils are studied while maintaining the 50 Ohm line impedance.

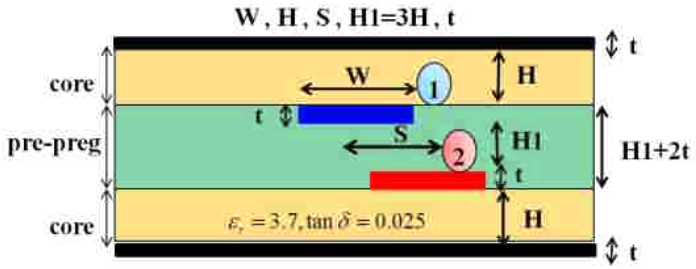

Figure 2.3. Stackup of broadside coupled single-ended lines

The capacitance and inductance curves scale with geometry when the 50 Ohm line impedance is maintained, as shown in Figure 2.4 and Figure 2.5. The physics-based FEXT metric given in (52) scales with geometry for a fixed characteristic impedance of 50 Ohm, as shown in Figure 2.6.

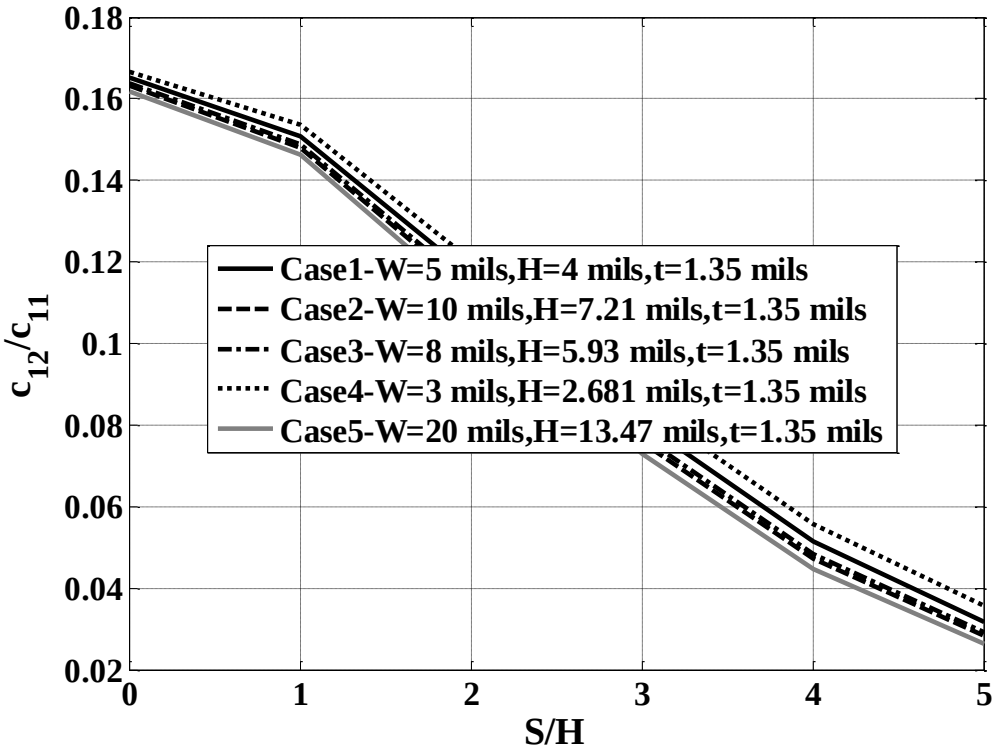

Figure 2.4. Scaling of coupling capacitance with geometry

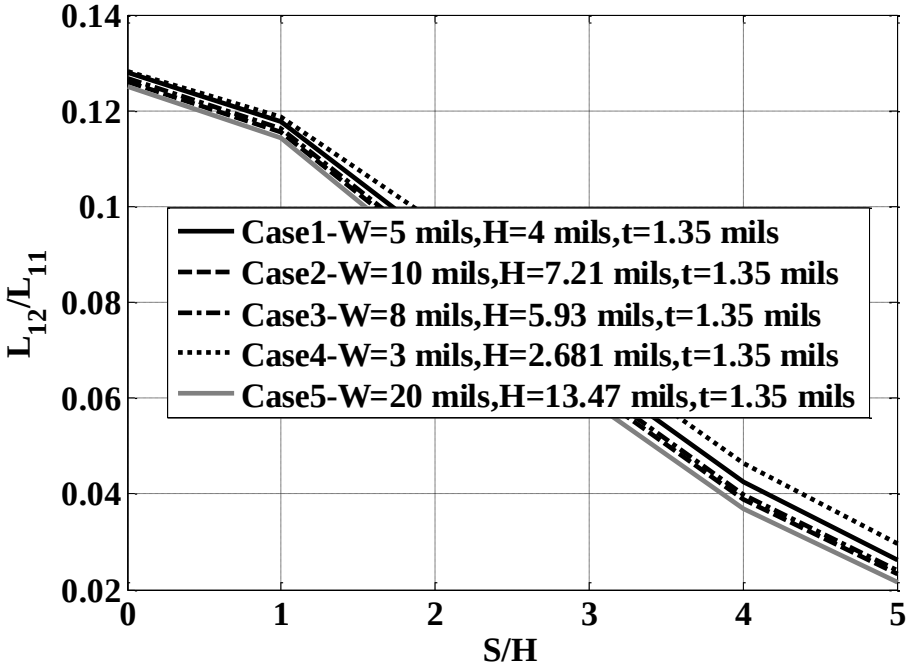

Figure 2.5. Scaling of coupling inductance with geometry

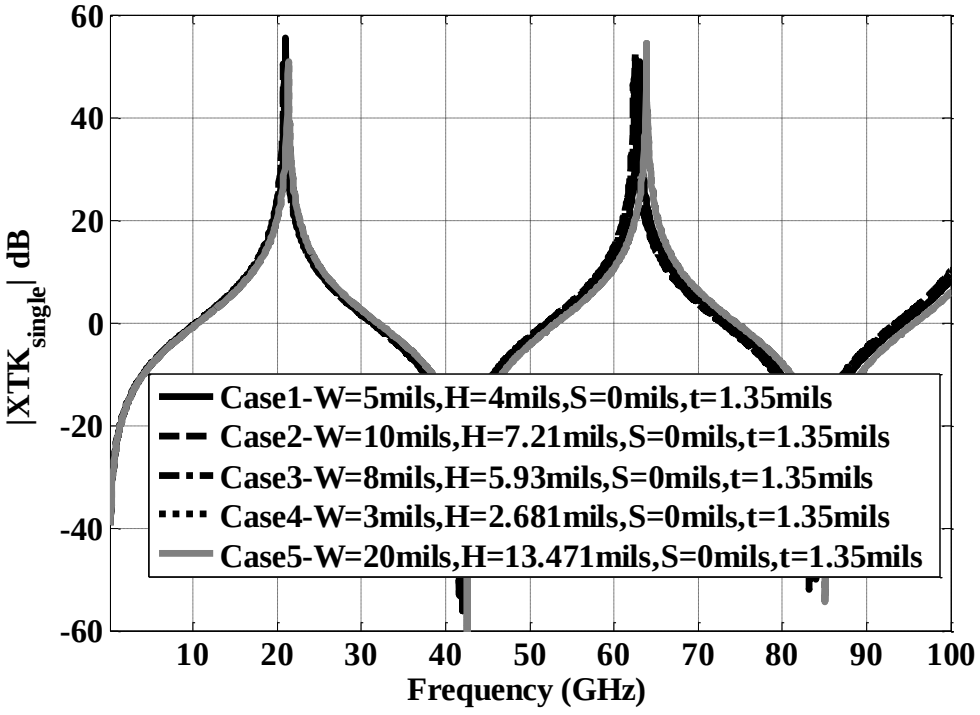

Figure 2.6. Scaling of the XTK metric for lossless single-ended coupled lines with geometry

A differential coupled line test structure, as shown in Figure 2.7, is a 10 inch complete broadside coupled model that uses a core dielectric with a relative permittivity of 3.7 and a loss tangent of 0.025 at 1 GHz. The pre-preg dielectric constant is set 15% higher than the core dielectric constant. The lossless case is used to simplify the analysis without losing sight of the coupling physics. Five test cases with different trace widths of 3, 5, 8, 10, and 20 mils are studied while maintaining the 100 Ohm line impedance.

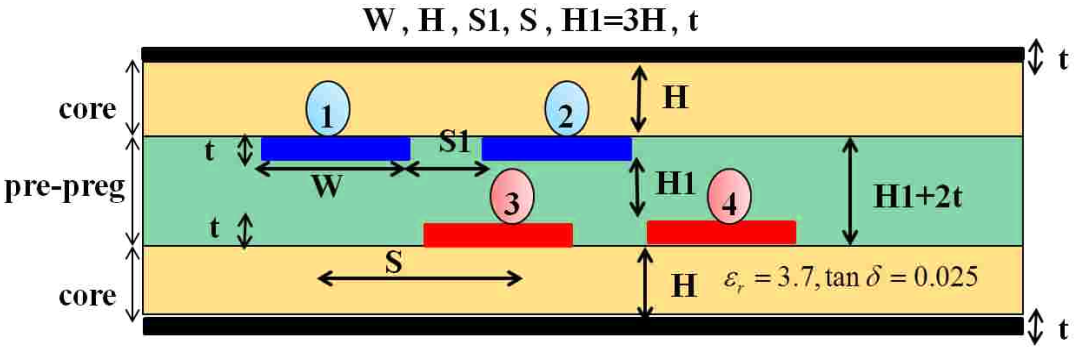

Figure 2.7. Stackup of broadside coupled differential lines

The capacitance and inductance curves scale with geometry when the 100 Ohm line impedance is maintained, as shown in Figure 2.8, Figure 2.9, Figure 2.10, and Figure 2.11. The physics-based differential FEXT metric given in equation (55) scales with geometry for fixed characteristic impedance of 50 Ohm, as shown in Figure 2.12.

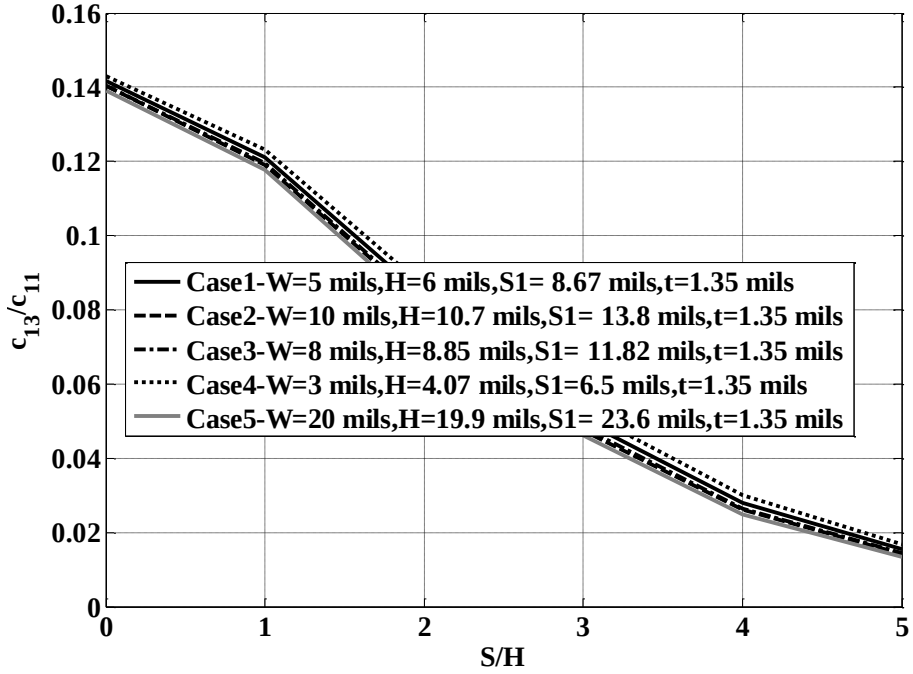

Figure 2.8. Scaling of coupling capacitance C13 for differential lines

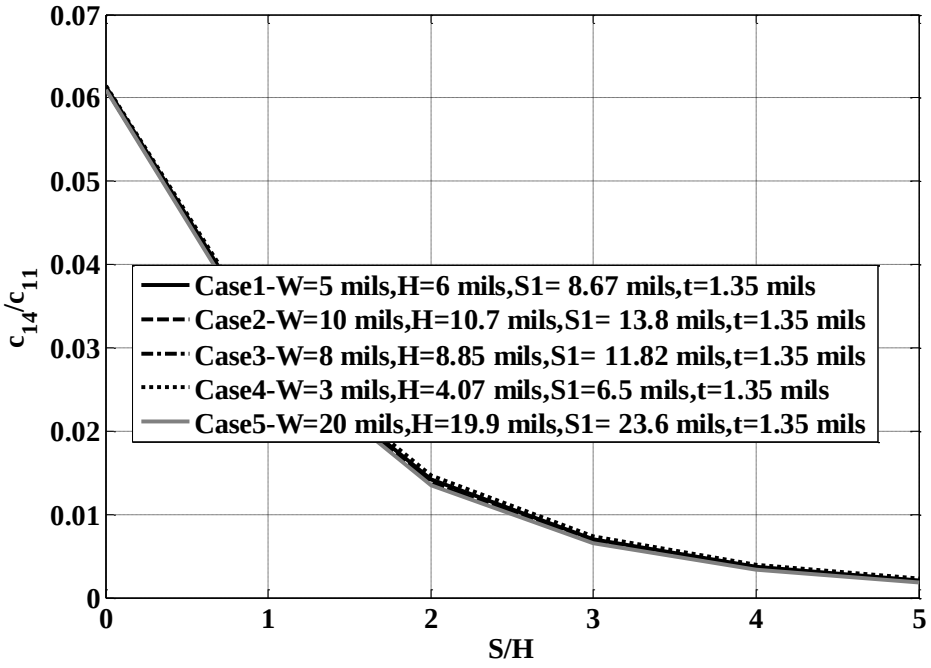

Figure 2.9. Scaling of coupling capacitance C14 for differential lines

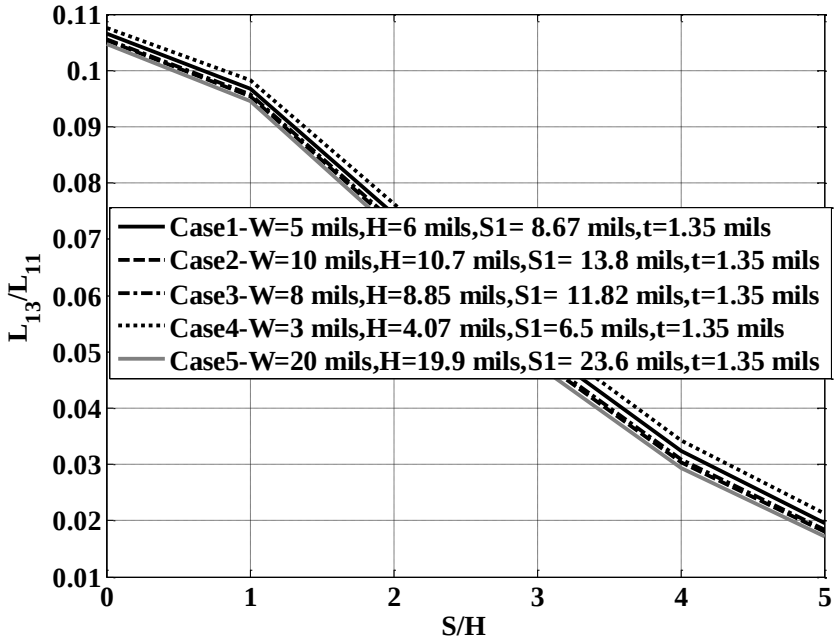

Figure 2.10. Scaling of coupling inductance L13 for differential lines

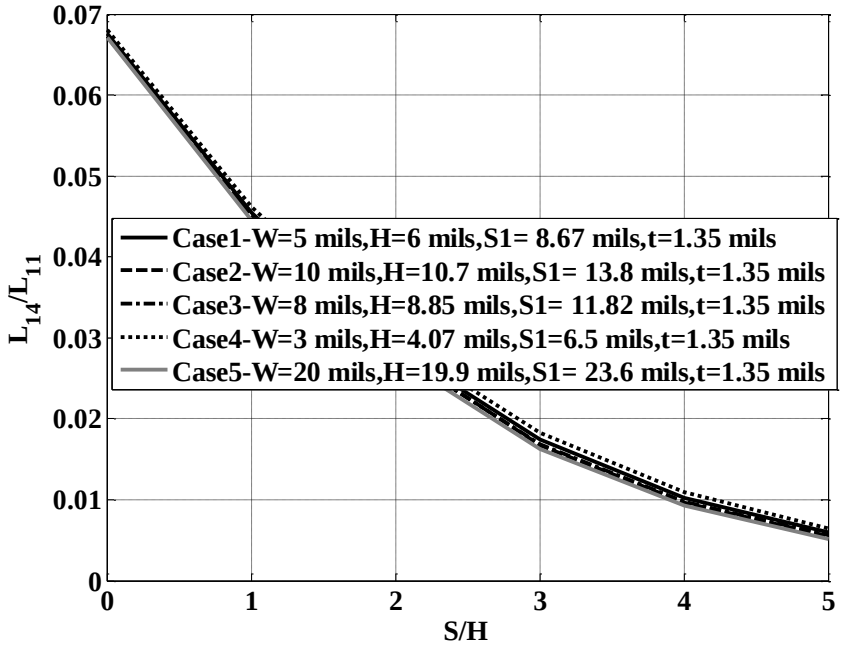

Figure 2.11. Scaling of coupling inductance L14 with geometry for differential lines

The geometry scaling observed for the FEXT metric shown in Figure 2.6 and Figure 2.12 enables the generation of design guidelines based on one stackup and can be scaled seamlessly to other coupled line stackups. Similarly C23, C24, L23 and L24 also scale with geometry parameters. This scalability makes the developed guidelines applicable to any coupled line scenario as long as the characteristic impedance is maintained.

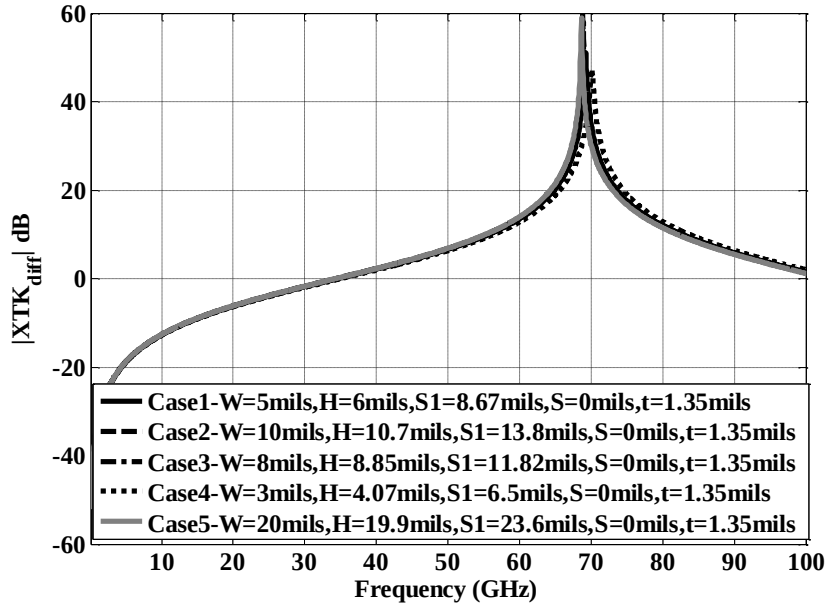

Figure 2.12. Scaling of the XTK metric for lossless differential coupled lines with geometry

2.3. VALIDITY OF THE TEM MODE ASSUMPTION FOR COUPLED LINES IN INHOMOGENEOUS MEDIA

A single-ended coupled line test structure with the stackup shown in Figure 2.3 is a 10 inch lossy complete broadside coupled line using a core dielectric with a relative

permittivity of 3.7 and loss tangent of 0.025 at 1 GHz. Geometry parameters of W = 5mils, H=4 mils, S = 0 mils, and t = 1.35mils for a 50 Ohm characteristic impedance are chosen for validation. The pre-preg dielectric constant is set 15% higher than the core dielectric constant. The null frequency location can be computed using equation (59).

The TEM mode does not exist in inhomogeneous media, but the assumption of quasi-TEM is used for solving the telegrapher equations. The ratio of the axial field component to the transverse field component is computed in order to understand the sensitivity of the quasi-TEM mode assumption. The ratio for single-ended coupled lines in inhomogeneous and homogeneous media is compared as in Figure 2.13 and Figure 2.14 for the stackup shown in Figure 2.3. The observation point for the field calculation is between the one of the traces and its nearest reference plane. For single-ended coupled lines with 3H vertical spacing between the victim and aggressor traces, the axial field component is very small compared to the transverse field. When the ratio is very small, the TEM-mode assumption is fair.

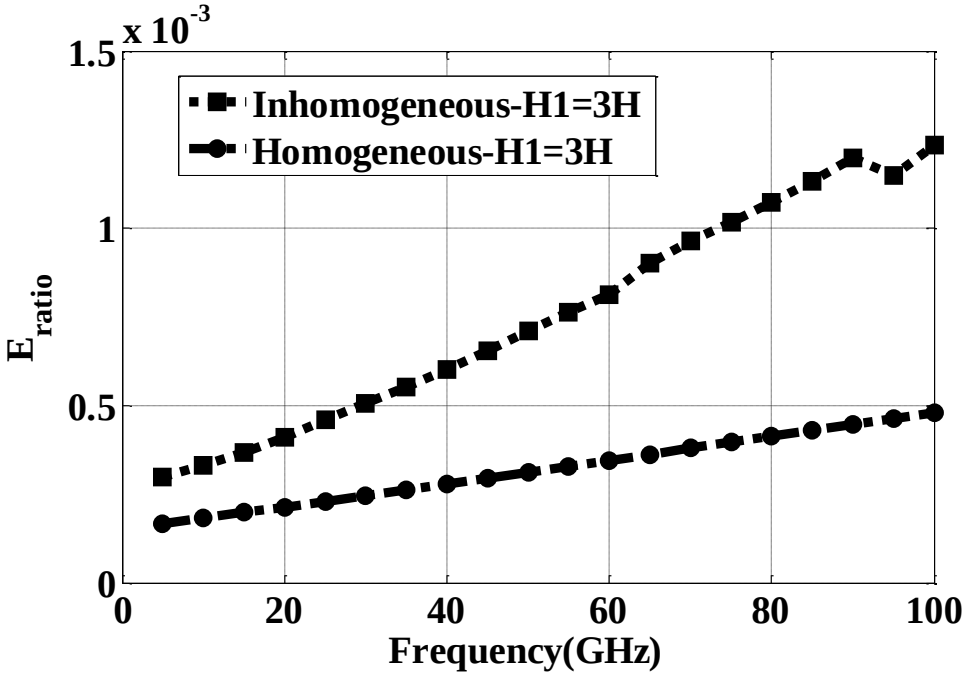

Figure 2.13. The ratio of axial E-field to transverse E-field

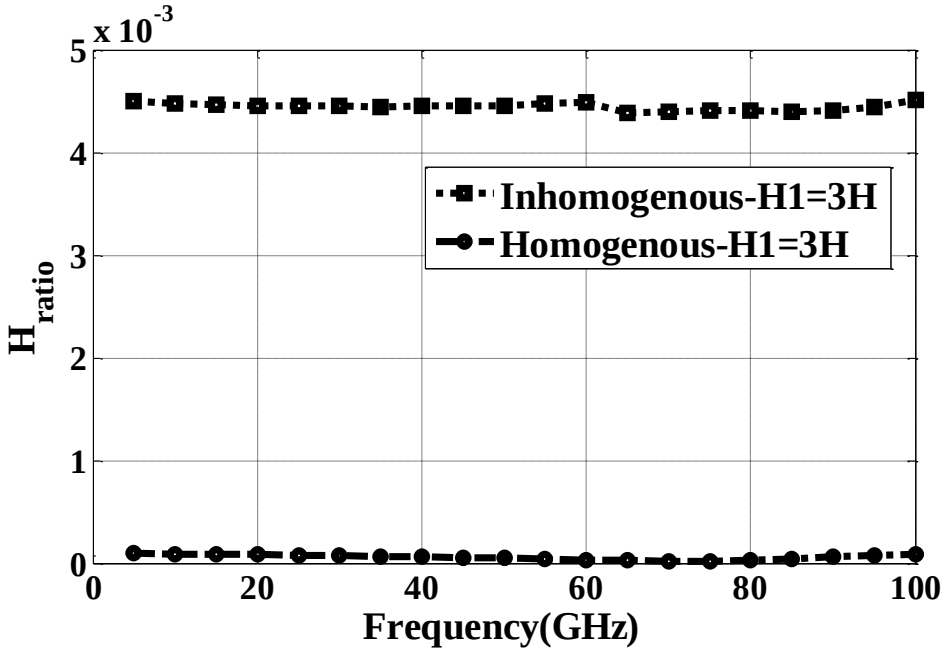

Figure 2.14. The ratio of axial H-field to transverse H-field

Higher order TM and TE modes can exist in a parallel-plate waveguide structure described by the stackup shown in Figure 2.3 and Figure 2.7. The onset of higher modes determines the upper bound for crosstalk expressions based on the TEM mode assumption. The cutoff frequency of the TM/TE modes can be computed using the transverse resonance technique described in [16]. The cutoff frequency using the transverse resonance method is computed as

$$f_C^{TM_1} = \frac{\left(3\times10^8\right)}{2\sqrt{\varepsilon_{EQ}}\left(2H + H1 + 2t\right)} \tag{61}$$

where,

$$\varepsilon_{EQ} = \frac{\varepsilon_{CORE}H + \varepsilon_{PREPEG}\left(H1 + 2t\right) + \varepsilon_{CORE}H}{2H + H1 + 2t}$$

The cutoff frequency of the TM1 mode for 3H vertical spacing between the traces computed using (61) is 128 GHz when H is 4 mils. The maximum value H can have is 6 mils for most practical PCB applications, in which case the cutoff frequency is 89 GHz. The cutoff frequency of the TM1 mode for 7H vertical spacing between the traces, computed using (61), is 75 GHz when H is 4 mils. The maximum value H can have is 6 mils for most practical PCB applications, in which case the cutoff frequency is 50 GHz. The vertical spacing of 7H is rarely used in practical PCB stackups due to the increasing cost of the material used.

The THRU and FEXT transfer functions obtained from the S-parameters from the Full-Wave solver and the transfer function equations using RLGC obtained from the 2D-solver are compared in Figure 2.15.

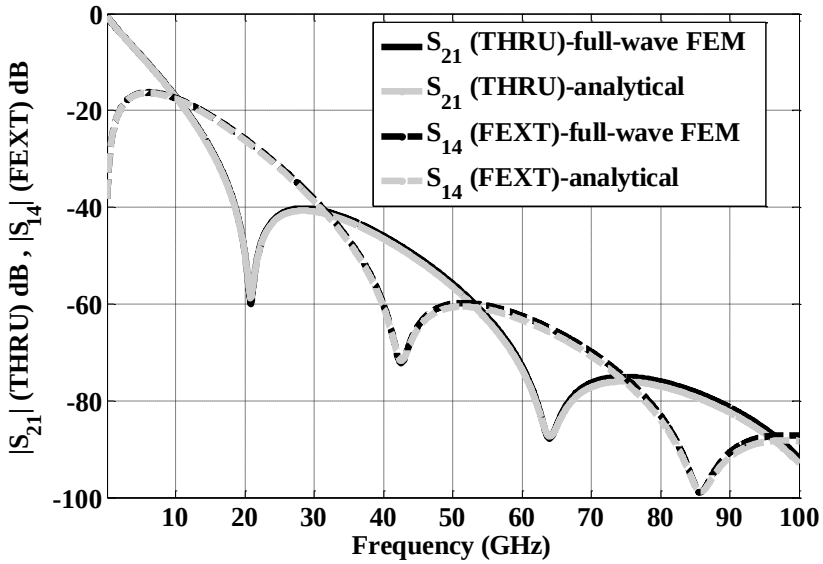

Figure 2.15. Validation of THRU and FEXT transfer functions from RLGC with S-parameters obtained from the Full-Wave solver for single-ended complete broadside coupled lines

The FEXT has maxima where THRU has minima, thereby reducing the signal-to-crosstalk ratio. The frequency location where THRU is null is

$$f = \frac{(2n-1)}{2\left|\left(\frac{l}{v_1} - \frac{l}{v_2}\right)\right|} = (2n-1)\times 21\times 10^9 \tag{62}$$

where,

$v_1 = 1.5245\times 10^8\ m/s \quad , \quad v_2 = 1.503\times 10^8\ m/s$

$l = 10\ inches$

The pre-preg dielectric constant is varied from 15% to 0% higher than the core dielectric constant. A step input of 1V pk-pk with a rise/fall time of 10 ps is applied to the aggressor trace to obtain the FEXT step response at the victim's receiver. The 15% difference in pre-preg and core dielectric is worse than 10%, while 10% is worse than 5%, and 5% is worse compared to homogeneous media, as shown in Figure 2.16.

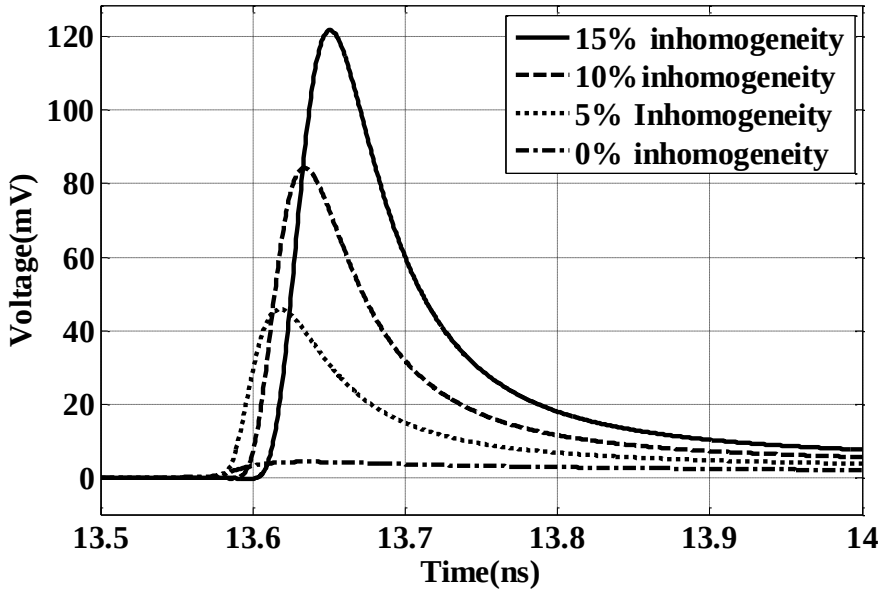

Figure 2.16. Comparison of the FEXT step response for different degrees of inhomogeneity in the dielectric media for single-ended coupled Tx lines

A differential coupled line test structure with the stackup shown in Figure 2.7 is a 10 inch lossy complete broadside coupled line using a core dielectric with a relative permittivity of 3.7 and loss tangent of 0.025 at 1 GHz. Geometry parameters of W = 5mils, H=6 mils, S = 0 mils, S1 = 8.67 mils and t = 1.35mils for a 100 Ohm characteristic impedance are chosen for validation. The pre-preg dielectric constant is set 15% higher than the core dielectric constant. The differential THRU and FEXT transfer functions obtained from the S-parameters from the Full-Wave solver and the transfer functions using RLGC obtained from the 2D-solver are compared in Figure 2.17.

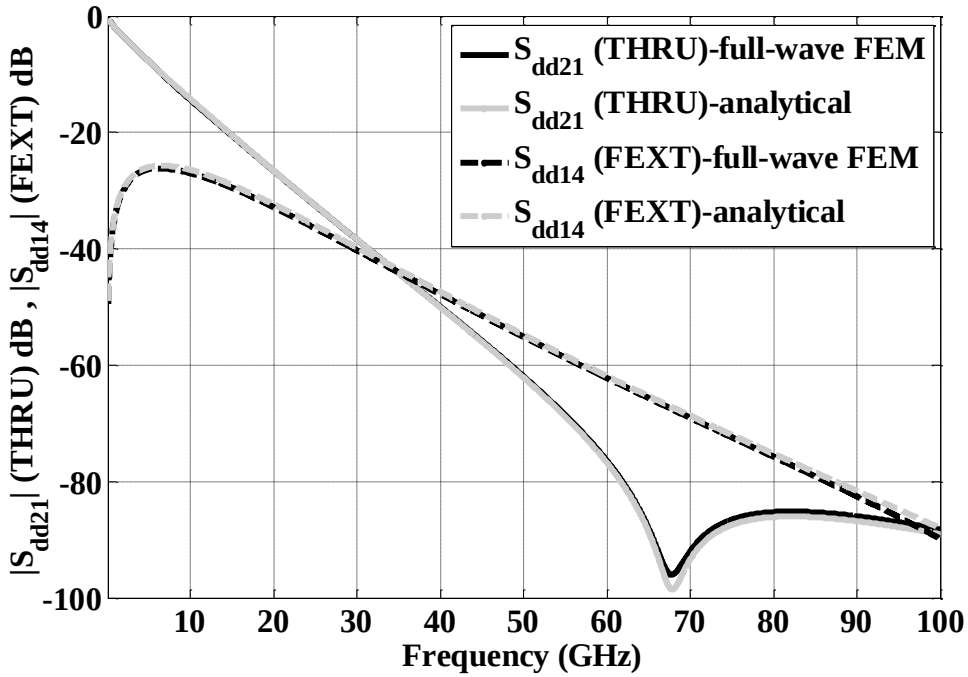

Figure 2.17. Validation of THRU and FEXT transfer functions from RLGC with S-parameters obtained from Full-Wave solver for differential complete broadside coupled lines

The FEXT has maxima where THRU has minima, thereby reducing the signal-to-crosstalk ratio. The frequency location where THRU is null is

$$f = \frac{(2n-1)}{2\left|\left(\frac{l}{v_1} - \frac{l}{v_2}\right)\right|} = (2n-1)\times 69.4\times 10^9 \tag{63}$$

where,

$v_1 = 1.5056\times 10^8\ m/s \quad , \quad v_2 = 1.4992\times 10^8\ m/s$

$l = 10\ inches$

The pre-preg dielectric constant is varied from 15% to 0% higher than the core dielectric constant. A step input of 1V pk-pk with a rise/fall time of 10 ps is applied to the aggressor trace to obtain the FEXT step response at the victim's receiver. The 15% difference in pre-preg and core dielectric relative is worse than 10%, while 10% is worse than 5%, and 5% is worse compared to homogeneous media, as shown in Figure 2.18.

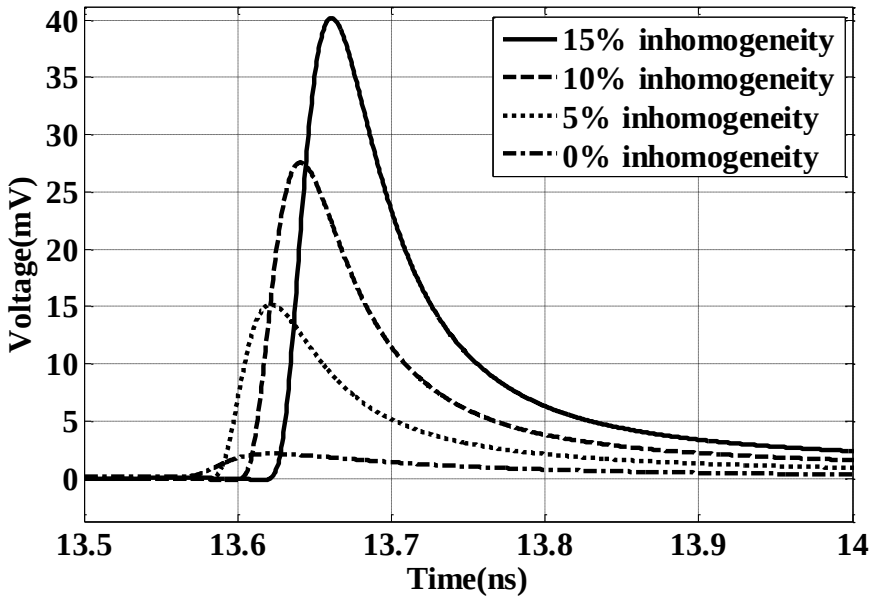

Figure 2.18. Comparison of FEXT step response for different degrees of inhomogeneity in the dielectric media for differential coupled Tx lines

As the signaling speeds increase, the amount of FEXT impacting the receiver eye increases with the increasing amount of inhomogeneity in the medium. The amount of FEXT seen on the victim receiver side for a differential coupled Tx line scenario is at least 3 times smaller compared to a single-ended coupled Tx line scenario for the same input, as seen from Figure 2.16 and Figure 2.18.

2.4. ROBUSTNESS OF DIFFERENTIAL LINES FROM FEXT DUE TO INHOMOGENEOUS MEDIA

H1 is varied from 1H to 5H to understand the sensitivity of the differential FEXT transfer function to H1 for differential coupled line stackups described in Figure 2.7 for a 10 inch coupled line. Geometry parameters of W = 5mils, H=6 mils, S = 0 mils, S1 = 8.67 mils and t = 1.35mils for a 100 Ohm characteristic impedance are chosen. The pre-preg dielectric constant is assumed to be 15% higher than the core dielectric constant. The variation in the coupling capacitance and inductance that dictate the location of the null frequency location is shown in Figure 2.19. The comparison of differential THRU and FEXT transfer functions for different values of H1 is shown in Figure 2.20.

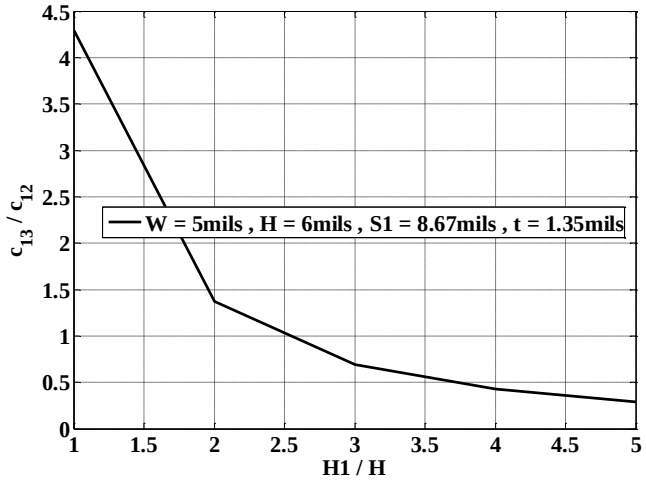

(a)

Figure 2.19. (a) Variation in coupling capacitance with vertical spacing between the victim and aggressor (b) Variation in coupling inductance with vertical spacing between the victim and aggressor

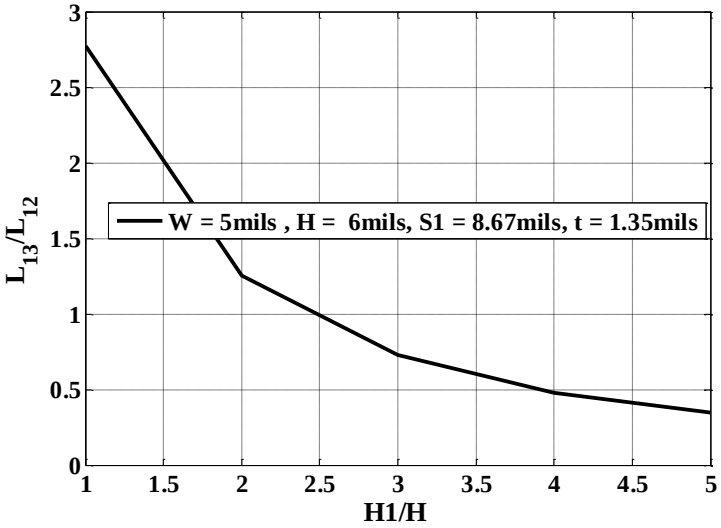

(b)

Figure 2.19. (a) Variation in coupling capacitance with vertical spacing between the victim and aggressor (b) Variation in coupling inductance with vertical spacing between the victim and aggressor (cont.)

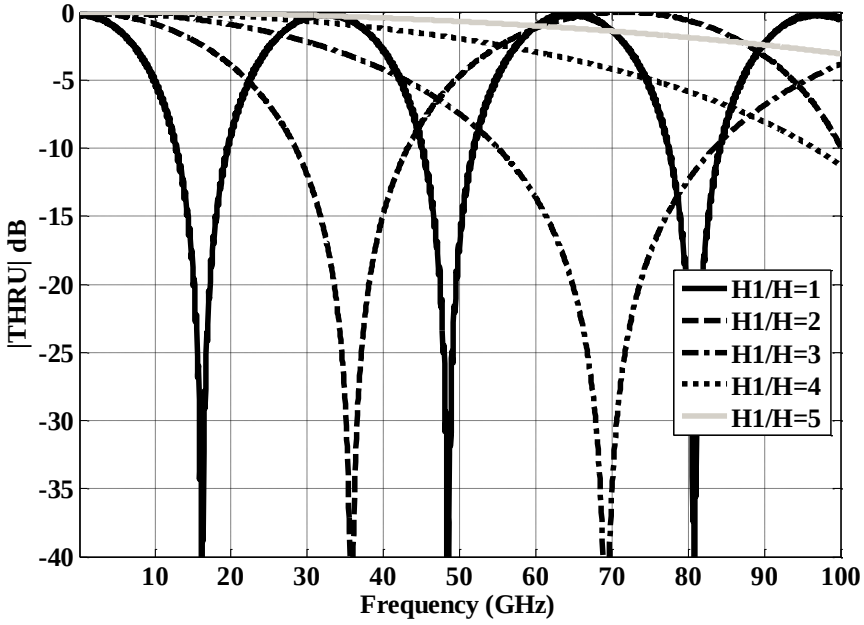

(a)

Figure 2.20. (a) Variation of THRU with vertical spacing between the victim and aggressor (b) Variation of FEXT with vertical spacing between the victim and aggressor

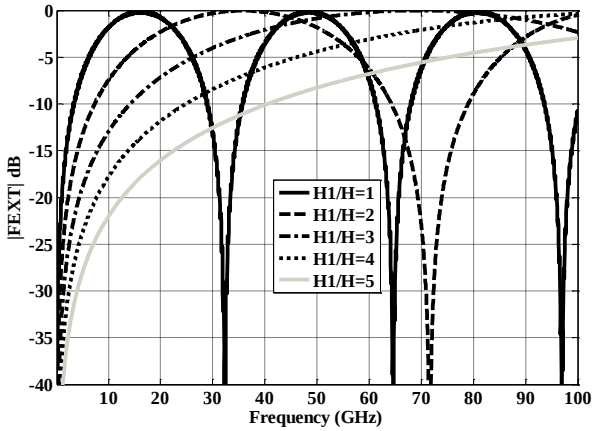

(b)

Figure 2.20. (a) Variation of THRU with vertical spacing between the victim and aggressor (b) Variation of FEXT with vertical spacing between the victim and aggressor (cont.)

The ratio of the mutual inductances L_{13} to L_{12} and the mutual capacitances C_{13} to C_{12} becomes greater than 1 when H1 is less than 2H, pushing the THRU null frequency below 20 GHz, making it more susceptible to FEXT.

2.5. IMPACT DUE TO FEXT IN INHOMOGENEOUS MEDIA

A differential input of 500mV pk-pk with a rise/fall time of 35 ps at a data rate of 10 Gbps, a rise/fall time of 29 ps at a data rate of 12 Gbps, and a rise/fall time of 21 ps at a data rate of 16 Gbps is used on both the aggressor and victim for the stackup described in Figure 2.7 for a 10 inch coupled line. Case1 parameters of differential stackup is used. The pre-preg dielectric constant is assumed to be 15% higher than the core dielectric constant. The eye width and eye height of homogeneous and inhomogeneous models are compared at 10, 12, and 16 Gbps in Table 2.1. The FEXT and THRU transfer functions of broadside coupled differential lines in homogeneous and inhomogeneous media are compared in Figure 2.21. The FEXT is negligible in homogeneous media for the same stackup, and the location of null frequency occurs at infinity. The impact of FEXT can be seen on eye height and eye width at 16 Gbps in Figure 2.22.

Table 2.1. Comparison of eye diagram results of differential complete broadside coupled lines in homogeneous and inhomogeneous media

	10 Gbps		12 Gbps		16 Gbps	
Media	EW (ps)	EH (mV)	EW (ps)	EH (mV)	EW (ps)	EH (mV)
Inhomogeneous-without crosstalk	74	171	53	120	23	36
Homogeneous-without crosstalk	75	183	55	134	27	53
Inhomogeneous-With crosstalk	66	161	45	108	13	20
Homogeneous-with crosstalk	75	182	55	134	27	53

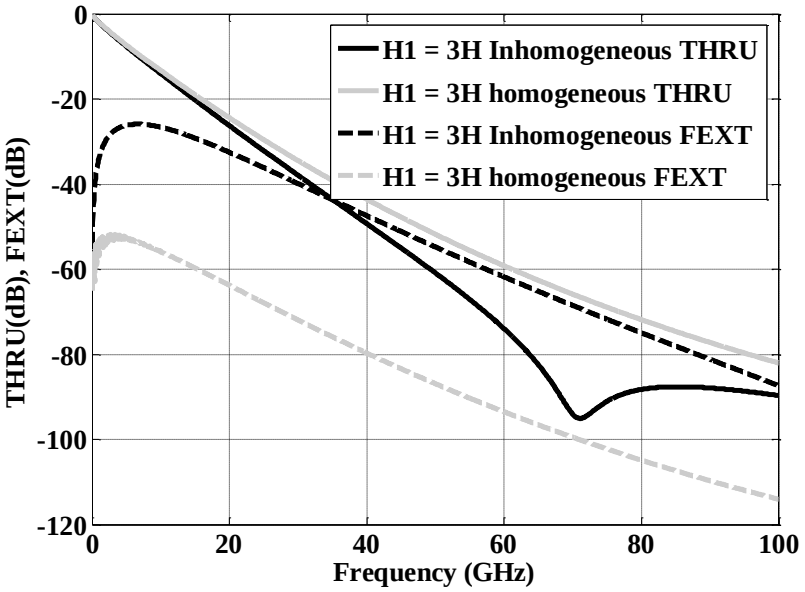

Figure 2.21. Comparison of FEXT and THRU transfer functions of homogeneous and inhomogeneous media for broadside differential coupled lines

Table 2.1 shows that with 15% inhomogeneity between the core and pre-preg, the in-phase crosstalk has 10% impact on eye width at 10 Gbps, 14% impact on eye width at 12 Gbps, and 42% impact on eye width at 16 Gbps, as compared to less than 1% in the case of homogeneous media.

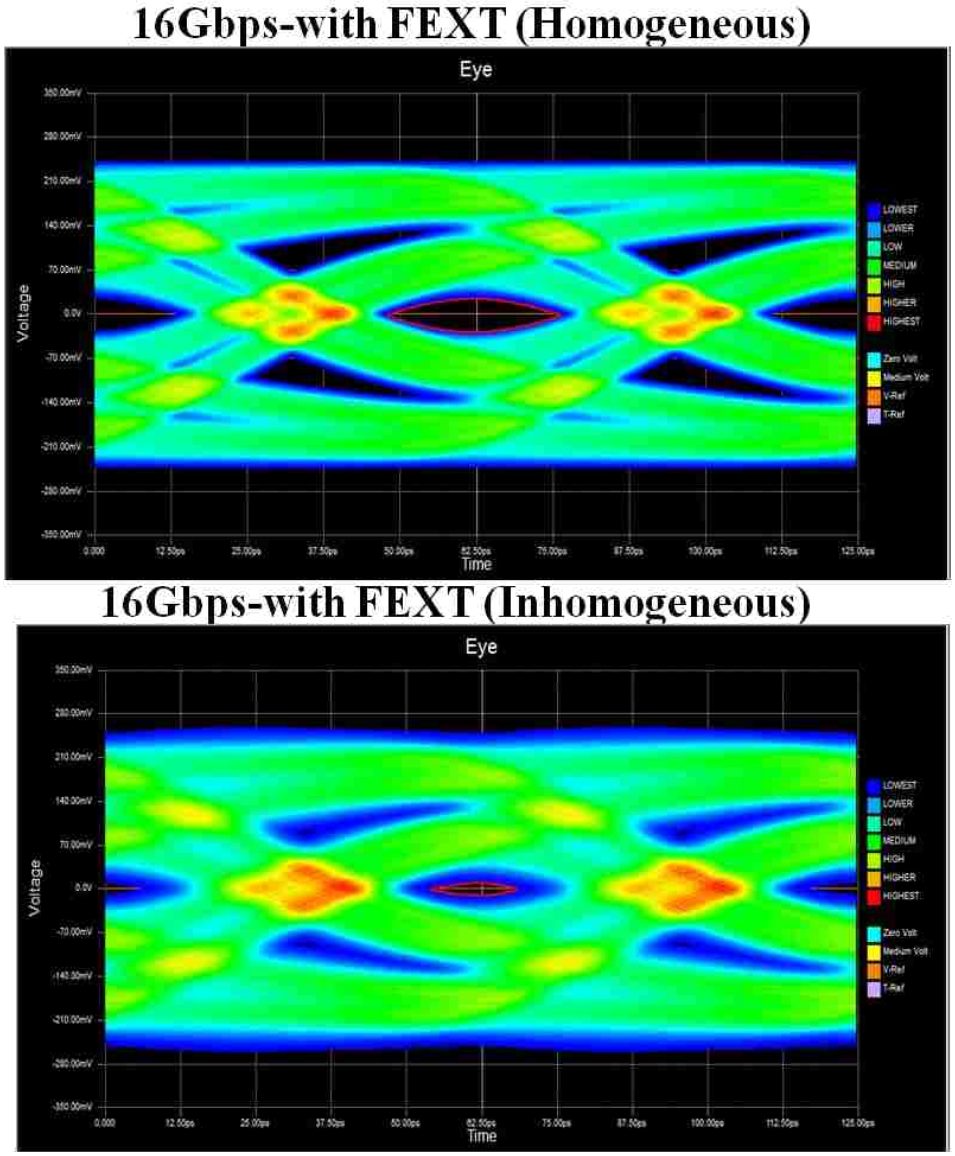

Figure 2.22. Eye opening comparison between homogeneous and inhomogeneous media for broadside differential coupled lines at 16 Gbps

2.6. SENSITIVITY OF HORIZONTAL EYE OPENING FROM FEXT WITH GEOMETRY PARAMETERS

A 10 inch complete broadside differential coupled trace using core dielectric with relative permittivity of 3.7 and loss tangent of 0.025 at 1GHz using stackup is shown in Figure 2.23. As the difference in dielectric constants of the core and pre-preg materials increases, the impact on the eye opening from FEXT increases. The inhomogeneity percentage controls the C_{13} and C_{14} that determines the FEXT impact. Smaller inhomogeneity implies higher peaking location, thereby reducing the FEXT impact on the eye opening in the frequency range of interest. Differential coupled lines are more robust compared to single-ended coupled lines at higher data rates, as C_{13} is always less than C_{12} for nominal vertical spacing of 3H. Design engineers have less control over the material properties in high volume manufacturing of low-cost PCBs.

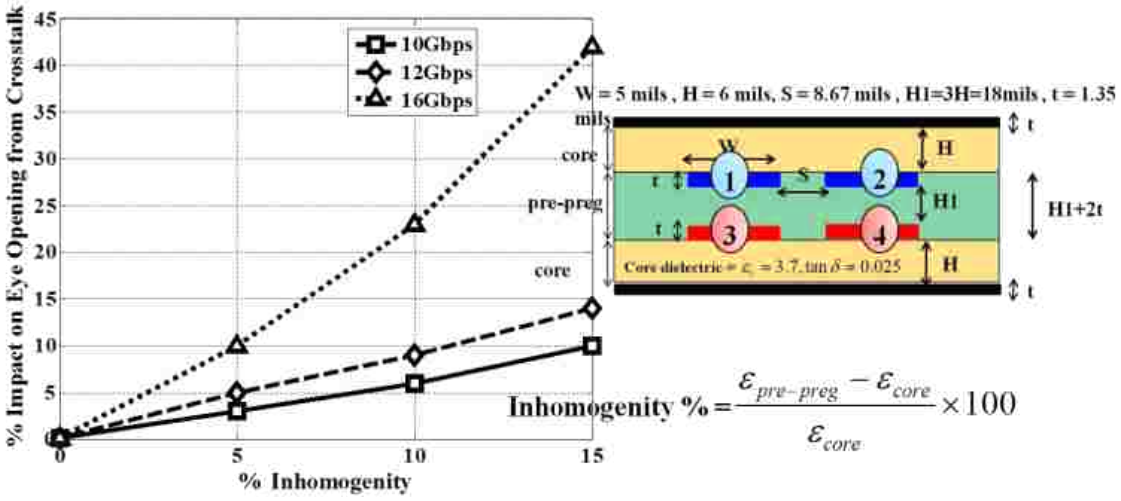

Figure 2.23. Comparison of FEXT impact on eye opening for differential complete broadside coupled lines at 10, 12, and 16 Gbps by varying the degree of inhomogeneity

A 10 inch broadside coupled and edge coupled differential traces using core dielectric with relative permittivity of 3.7 and loss tangent of 0.025 at 1GHz using stackup is shown in Figure 2.24 and Figure 2.25. As the horizontal separation between the victim and aggressor traces is increased, the impact of FEXT on the eye opening is reduced. The horizontal separation between the victim and aggressor traces controls the factors C_{13}, C_{14}, L_{13}, and L_{14} that determines the FEXT impact. The mutual capacitance and mutual inductance values control the peaking frequency locations in the FEXT transfer function. The peaking locations are pushed to a higher frequency as the spacing S1 is increased, thereby reducing the FEXT impact on the eye opening. For the stackup shown in Figure 2.24, the FEXT impact for the horizontal spacing in the range from 3H to 7H is more than the impact at 3H. The aggressor positive trace is symmetric from the victim's positive and negative trace when the spacing is close to 3H. The effect of the aggressor positive trace is cancelled in the differential FEXT at the victim's receiver. This trend occurs as C_{13} and L_{13} are less than C_{14} and L_{14} and it continues until the individual values are negligible.

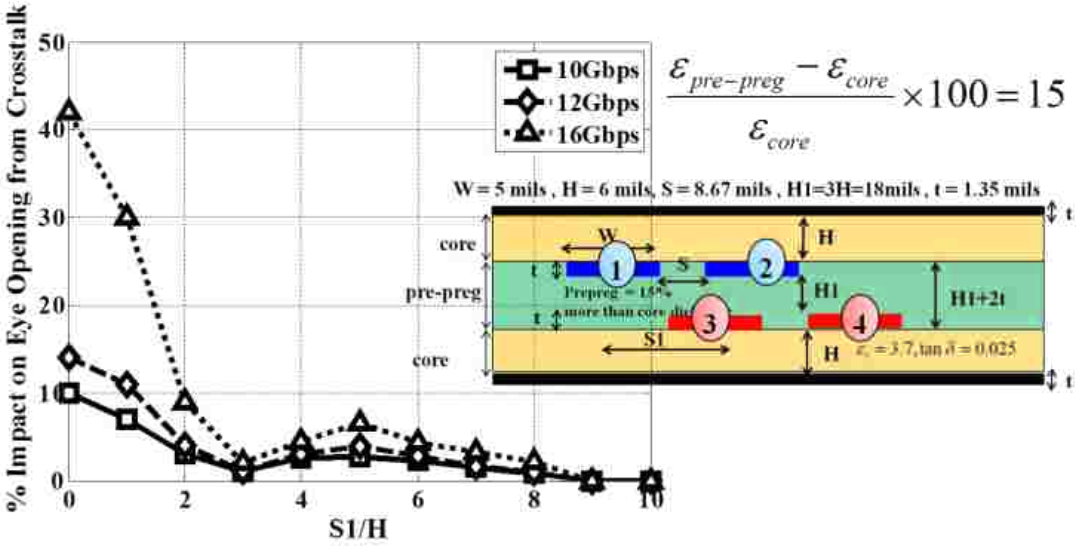

Figure 2.24. Comparison of FEXT impact on eye opening between differential offset broadside coupled lines at 10, 12, and 16 Gbps by varying the offset spacing

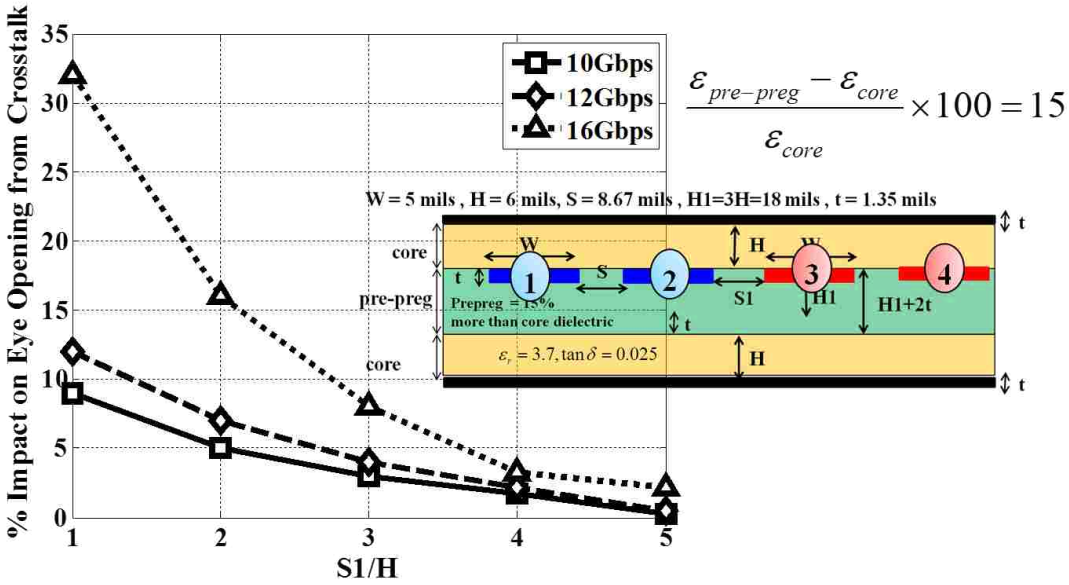

Figure 2.25. Comparison of FEXT impact on eye opening between differential offset edge coupled lines at 10, 12, and 16 Gbps by varying the offset spacing

The impact of FEXT on the eye opening decreases as the S1 spacing increases for the stackup shown in Figure 2.25. For spacing above 3H, the impact is less than 10% for the stackup shown in Figure 2.24 and Figure 2.25.

A 10 inch complete broadside differential coupled trace using core dielectric with relative permittivity of 3.7 and a loss tangent of 0.025 at 1 GHz using stackup is shown in Figure 2.26. As the vertical separation between the victim and aggressor traces is increased, the impact of FEXT on the eye margin reduction is reduced. The vertical separation between the victim and aggressor traces controls C_{13}, C_{14}, L_{13}, and L_{14}, which determine the FEXT impact. Differential coupled lines are more robust to FEXT, since C_{13} is always less than C_{12} for vertical spacing above 3H. When the vertical spacing is less than 2H, then C_{13} is greater than C_{12} and directly impacts its FEXT immunity. Design engineers with a limit on their board thickness can use a horizontal offset separation of at least 3H instead of increasing the board thickness.

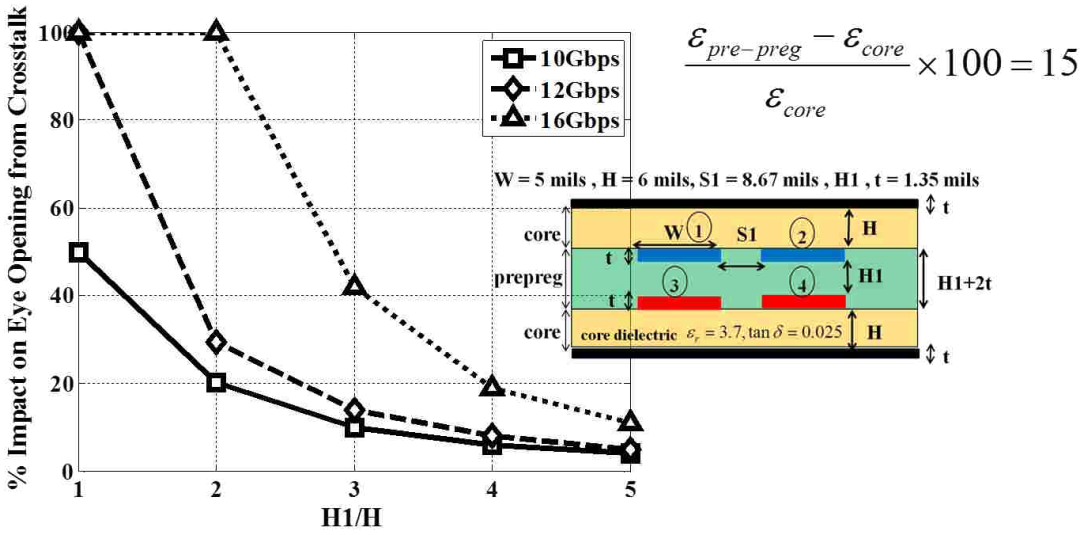

Figure 2.26. Comparison of the FEXT impact on eye opening for differential complete broadside coupled lines at 10, 12, and 16 Gbps by varying the vertical spacing H1

A complete broadside differential coupled trace using a core dielectric with a relative permittivity of 3.7 and a loss tangent of 0.025 at 1GHz using stackup shown in Figure 2.27 is studied. A step input of 1V pk-pk with a rise/fall time of 10ps is applied on an aggressor trace to obtain the FEXT step response at the victim's receiver. The end-to-end signal link path spans a length of 10 inches. The length of the coupled section in the entire signal path is varied from 1 inch to 10 inches. As the coupled length section is increased, the impact of FEXT on the eye margin reduction is increased. The coupled length determines the frequency location where FEXT has a maxima. The FEXT impact is severe when the frequency location is pushed into lower frequencies. Longer coupled length translates into worse FEXT noise, as shown in Figure 2.28. The coupled length cannot be more than 3 inches in order to be within 10% of the receiver margin assigned to FEXT noise for signaling speeds up to 16Gbps, as shown in Figure 2.27. Depending on the amount of the receiver margin allocated to FEXT, the designer can choose the appropriate length.

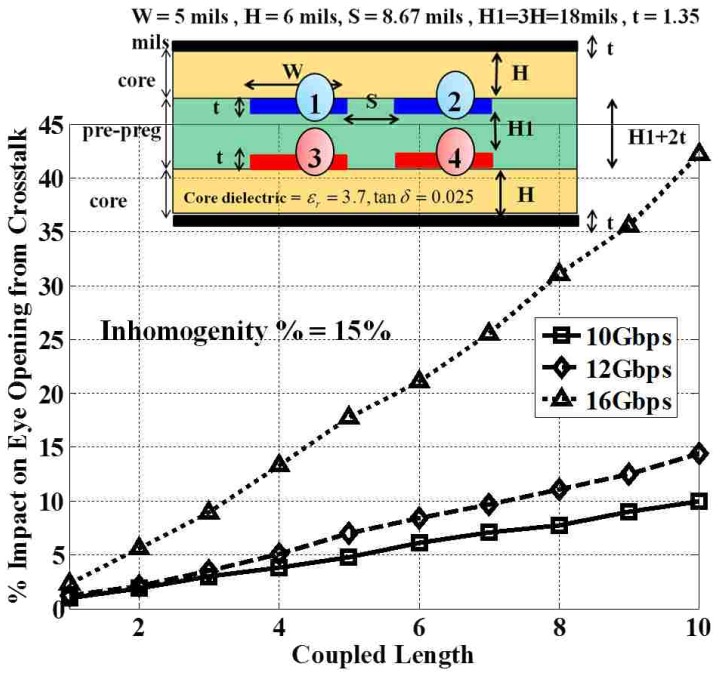

Figure 2.27. Comparison of FEXT impact on eye opening for differential complete broadside coupled lines at 10Gbps, 12Gbps, and 16Gbps by varying the coupled length

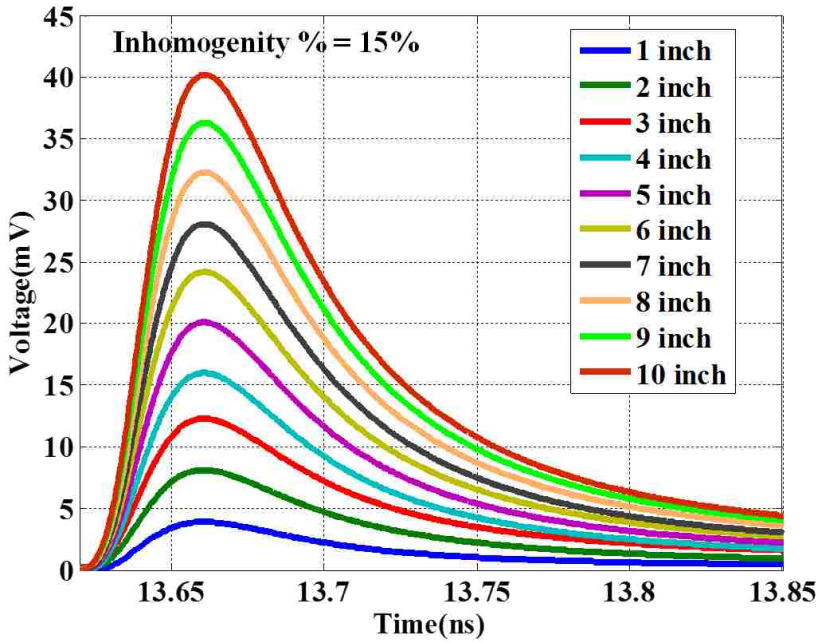

Figure 2.28. Comparison of FEXT step response for various coupled lengths

Guidelines can be developed based on FEXT transfer functions that have one-to-one mapping between the coupling physics and the FEXT impulse response used to generate BER eye contour. The following are some typical guidelines for a10 inch coupled line based on the observations thus far for a receiver with a margin of 10%. To stay within 10% receiver margin, limit the degree of inhomogeneity between the core and pre-preg to less than 5% for complete broadside coupled traces when H1=3H. The coupled length for complete broadside coupled traces cannot be more than 3 inches when inhomogeneity between the core and pre-preg is 15% and H1=3H for signaling speeds beyond 16Gbps. The horizontal spacing between the aggressor and victim traces for broadside coupled traces should be at least 2H for 15% inhomogeneity between the core and pre-preg when H1=3H. The horizontal spacing between the aggressor and victim traces for edge coupled traces should be at least 3H for 15% inhomogeneity between the core and pre-preg when H1=3H. Vertical spacing between the aggressor and victim traces for complete broadside coupled traces should be at least 5H when inhomogeneity between the core and pre-preg is 15%.

2.7. CONCLUSIONS

The focus of this paper is to study the impact of FEXT on eye opening for coupled lines present in inhomogeneous media. Closed form expressions are developed for the FEXT transfer function from telegrapher equations to predict the single-ended and differential crosstalk response and the mode cancellation effect. The FEXT transfer function has one-to-one mapping with the coupling physics and the PCB stackup. The FEXT metric is observed to scale with geometry for fixed line impedance. Differential coupled lines in inhomogeneous media are more robust to FEXT than are single-ended coupled lines. Differential lines are exposed to FEXT when H1 is less than 2H or for data rates above 10 Gbps. To stay within this same 10% receiver margin, coupled length for complete broadside coupled traces cannot be more than 3 inches when inhomogeneity between the core and pre-preg is 15% and H1=3H for signaling speeds beyond 16Gbps. The horizontal spacing between the aggressor and victim traces for broadside coupled traces should be at least 2H for 15% inhomogeneity between the core and pre-preg when

H1=3H. The horizontal spacing between the aggressor and victim traces for edge coupled traces should be at least 3H for 15% inhomogeneity between the core and pre-preg when H1=3H. Vertical spacing between the aggressor and victim traces for complete broadside coupled traces should be at least 5H when inhomogeneity between the core and pre-preg is 15%. The new guidelines can be formulated from the design curves based on amount of margin the receiver allows for FEXT noise. The proposed physics-based FEXT impact metric based on horizontal eye opening at specified BER will help electrical designers in choosing the stackup, coupled length and the dielectric materials that will support higher data rates.

3. EFFECT OF PERIODIC COUPLED ROUTING ON EYE OPENING OF HIGH SPEED LINK IN PRACTICAL PCBS

3.1. INTRODUCTION

Increases in printed circuit board (PCB) costs have led designers to use two signal layers between the reference planes introducing broadside coupling. Additionally, due to the fiber weave effect, designers have also been forced to route signal traces in a zig-zag fashion rather than in straight lines. This type of routing tends to be roughly periodic between the victim and aggressor. The periodic coupled routing creates periodic resonances in the near end crosstalk (NEXT) and nulls in Insertion loss (THRU) transfer functions due to Floquet modes. Due to the periodic resonances, the crosstalk is aggravated, which reduces the signal to crosstalk ratio. The increasing cost of boards with multiple layers has led to denser signal routing, forcing high-speed signal traces to be routed closely together over long distances. Designers generally place two signal layers between the reference planes to reduce the cost of the board. This type of routing creates broadside coupling between the signal layers, as shown in Figure 3.1. The end–end signal link path consists of a driver package block on the line card, which is connected to the backplane using the connector, followed by backplane traces, and a connector and receiver line card with Rx package. The signal link path is compromised by reflections in the packages, crosstalk in the vias, the line card traces and the backplane connectors, and reflections at the connectors. The channel is also affected by dielectric and conductor losses in the packages, line cards, connectors, and the backplane channel. In this state, the channel is already stressed and approaching the point where any additional noise source will close the eye at the receiver. Broadside coupling can be avoided by adding a ground layer or ensuring that signals do not overlap with each other, or by separating the planes far apart, but all of these options would result in board designs that are expensive board and, in some cases, mechanically unfeasible. The major objective of the present study is to determine quantitatively the effect of crosstalk due to periodic routing. Another objective is to help designers figure out the “dos” and “don’ts” of broadside coupled routing for higher signaling rates.

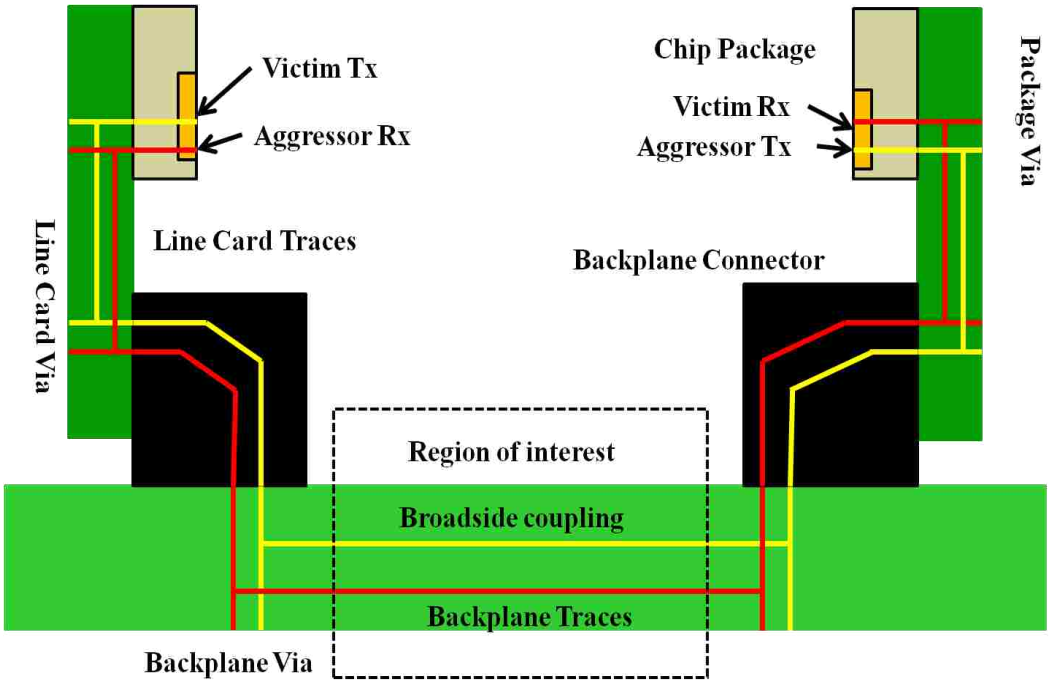

Figure 3.1. Signal link path of high speed channel

These spacing and cost constraints have made the design of routing that satisfies high speed design guidelines challenging. In this scenario, board designers decrease the complexity of the board layout by routing the traces in a zig-zag manner in certain sections of the board. The fiber weave effect also forces designers to route signal traces in a zig-zag fashion rather than in straight lines. The high speed signals routed in broadside coupled fashion, with signal traces routed at an angle, create an angular broadside coupled crosstalk problem. These high speed traces are coupled in a zig-zag fashion near the breakout region, uncoupled for a certain length, and then re-coupled back. Most of the layout routing patterns on adjacent signal layers are roughly periodic in nature. The unit cell lengths of the periodic coupled segments are generally in the range of 100–500 mils in length. As the number of aggressors increases, the amount of crosstalk-induced jitter from the periodic coupled segment increases, resulting in the eye collapsing at the receiver. One of the objectives of the present study is to compute the crosstalk transfer

function and location of Floquet mode frequencies. For near end crosstalk (NEXT), the coupled section near the breakout region—up to a few inches away, depending on the loss—is the more dominant term in the overall crosstalk transfer function, compared to coupled sections that occur far away from Rx. These coupled regions near the breakout at the Rx can be approximately periodic in nature (see Figure 3.2), and thus can introduce Floquet modes into the crosstalk transfer function.

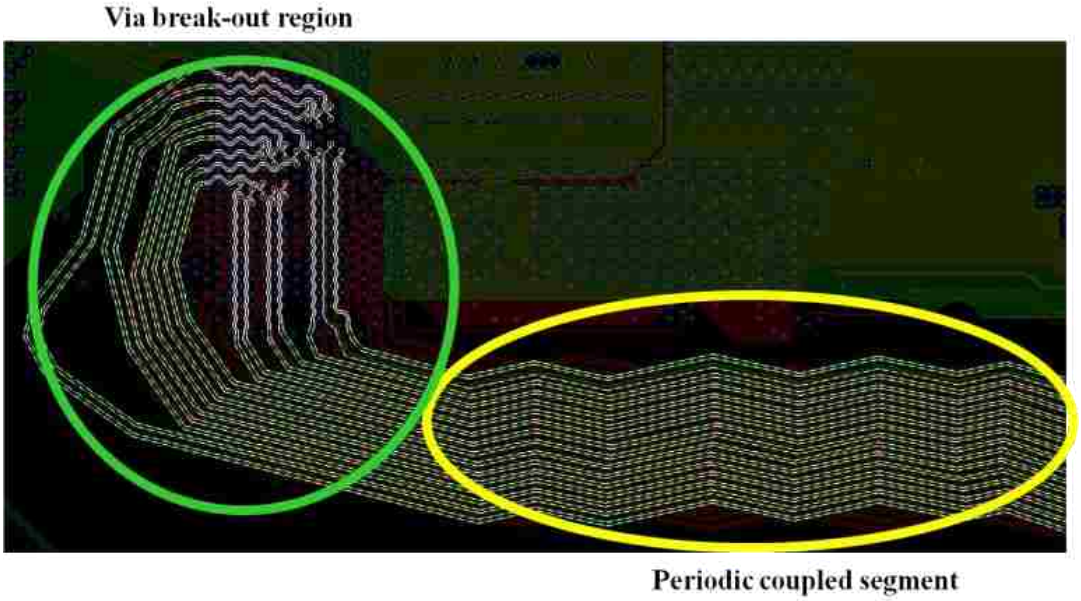

Figure 3.2. Periodic coupling observed in real board after the via breakout region

The periodic coupling phenomenon can occur from different aggressor signal traces of a high speed link to the victim signal trace. The aggregate effect of all these aggressors on the victim trace eye opening is not negligible, and can reduce its jitter budget at data rates above 8 Gbps. Real designs have traces longer than 20 inches,

including the add-in cards and connectors connected to backplane card, so the insertion loss is already very high at the Nyquist frequency without even considering any crosstalk from aggressors. The jitter budget is already limited due to inter-symbol interference (ISI), and any other noise source, like crosstalk from aggressors, can be lethal to the victim bit lane, leading to the failure of the design.

Another aim of this study is to understand the sensitivities of the routing angle, pattern and length of coupled parts that are fairly periodic in nature close to the receiver (Rx) of the victim. This will help to develop design guidelines for layout engineers based on the metric utilizing the mathematical model of crosstalk, so that current designs can be pushed to their limit while maintaining signal integrity.

Floquet mode theory has been studied and used extensively in [33]–[45] for creating frequency-selective structures and waveguides. Recently, periodic structures have been used to create electromagnetic bandgap structures [46]–[53] for suppressing noise on power/ground planes in high speed circuits. Crosstalk impact from periodic structures in practical high-speed server design has not yet been studied, as designers have avoided the coupling by shielding high speed signal layers between reference layers. To reduce the cost of the board, designers have no choice but to use broadside coupling, thereby exposing the design to crosstalk. The work presented in this paper provides an insight in coupling physics using Floquet theory and quantifies the crosstalk impact from periodic coupled segments in practical PCBs. Closed-form expressions for crosstalk transfer function and location of Floquet resonance based on the unit cell period are developed to estimate the impact on the bit-error rate (BER) eye opening using statistical analysis for coupled differential lines.

The physical presence of periodic coupled segments and Floquet mode resonance in crosstalk transfer function is explained in Section 3.2. In Section 3.3, closed-form expressions for the overall periodic coupled segment are derived using S-parameters of a single periodic unit cell with arbitrary source and load termination conditions. The Floquet mode resonances in the crosstalk transfer function are verified using measurements in Section 3.4. A formula to predict the occurrence of Floquet resonance is derived in Section 3.5. A comparison of the crosstalk impact on eye opening from periodic coupled segments and complete broadside coupled segments is given in Section

3.6. Guidelines based on horizontal BER eye opening to help the designer in the presence of Floquet modes are given in Section 3.7. Section 3.8 summarizes the paper.

3.2. FLOQUET MODES OBSERVED IN REAL BOARD SEGMENTS

To check the existence of Floquet modes in practical boards, a coupled segment (see Figure 3.3) is chosen and modeled in full-wave solvers.

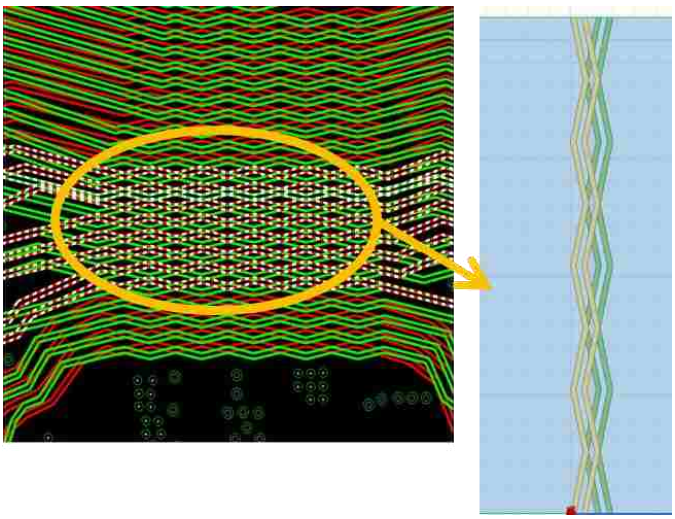

Figure 3.3. Periodic coupled segment picked from real board consisting of four unit cells

The stackup of a broadside coupled segment of length 400 mils is shown in Figure 3.4. The length of the unit cell is around 100 mils. There are four unit cells in the overall segment. The real board segment was composed of four unit cells. From the NEXT profile in Figure 3.5, it can be seen that Floquet resonances occur. Increasing the number of periods from 4 to 10 unit cells increases the Q factor of the resonance peak.

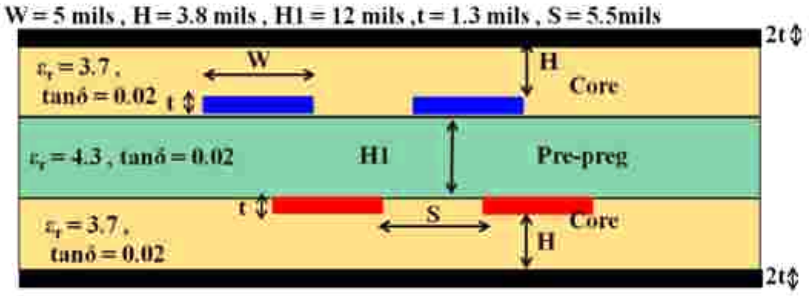

Figure 3.4. Stackup of the broadside coupled periodic segment

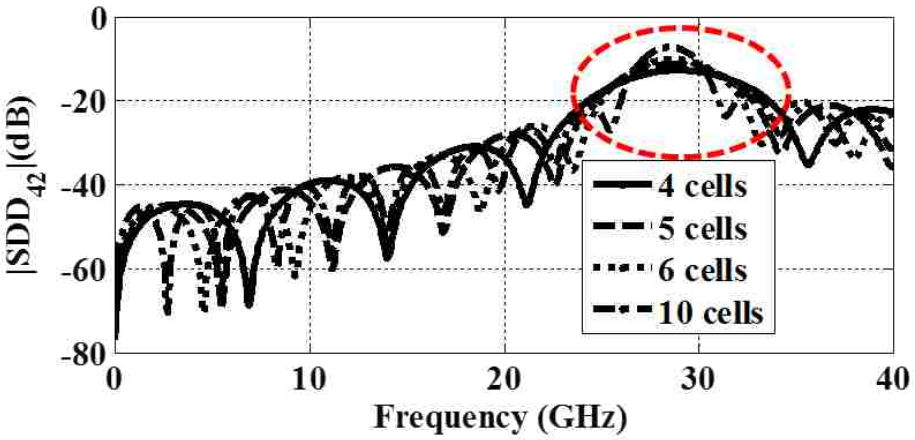

Figure 3.5. NEXT transfer function of real board with Floquet resonances

3.3. CLOSED FORM EXPRESSION OF NEXT TRANSFER FUNCTION OF PERIODIC COUPLED SEGMENTS USING SINGLE UNIT CELL

The periodic routing typically found in real designs can be classified into two types, A and B (see Figure 3.6 and Figure 3.7). The unit cell length varies from a lower limit of 125 mils to an upper limit of 2000 mils. A unit cell length of 2000 mils is

typically observed when routing at an angle of 10 degrees to negate the fiber-weave effect. The periodic topologies described in Figure 3.6 and Figure 3.7 can be generalized to a network of cascaded unit cells describing the differential periodic coupled lines, shown in Figure 3.8. The S-parameters of N unit cells are cascaded with each other as explained in [14] to obtain the overall cascaded S-parameter matrix.

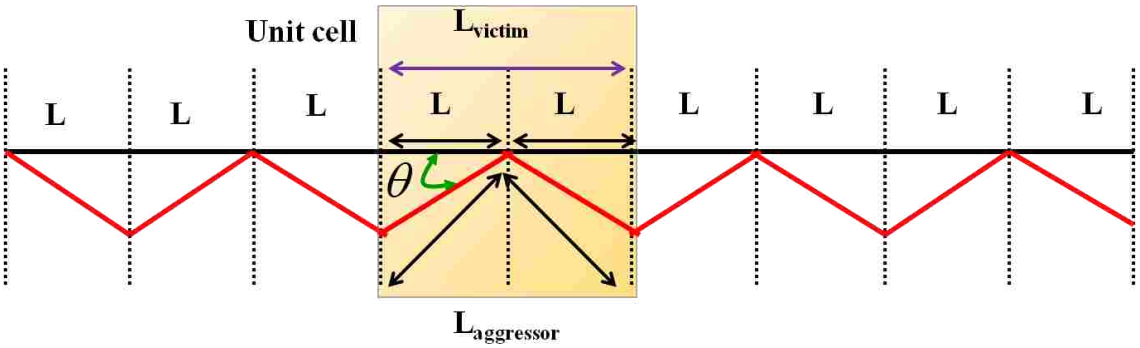

Figure 3.6. Unit cell A routing pattern

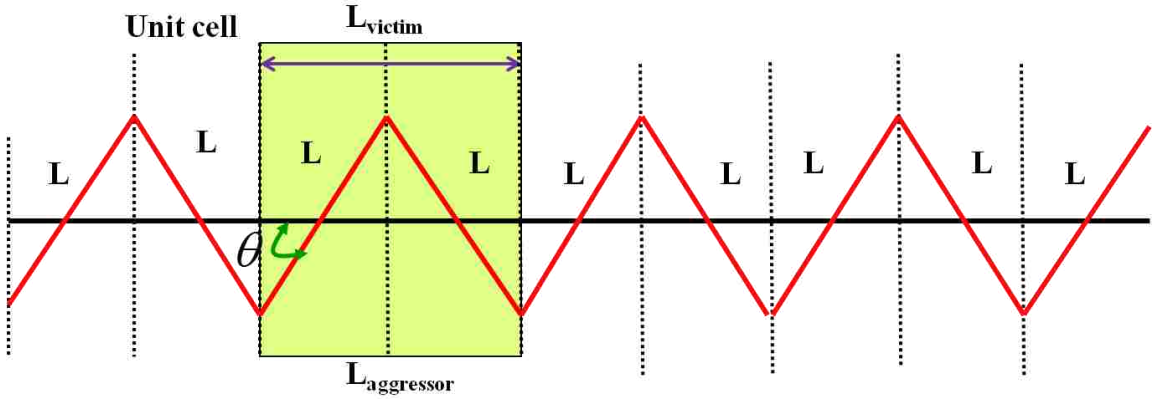

Figure 3.7. Unit cell B routing pattern

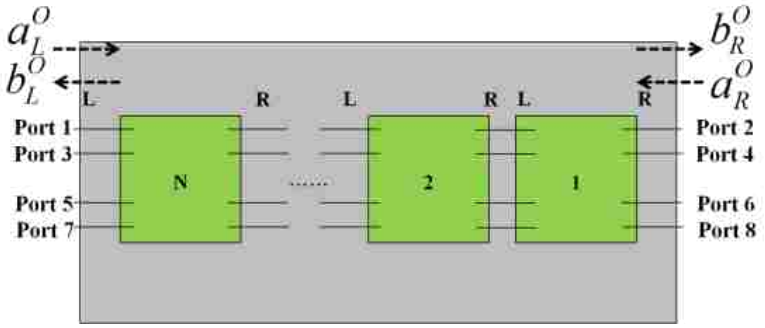

Figure 3.8. Cascaded network of S-parameter blocks representing periodic coupled segment

The cascading relations for cascading two S-parameter blocks are given as

$$S_{total} = \begin{bmatrix} B_1 A_2 (I - D_1 A_2)^{-1} C_1 + A_1 & B_1 A_2 (I - D_1 A_2)^{-1} D_1 B_2 + B_1 B_2 \\ C_2 (I - D_1 A_2)^{-1} C_1 & C_2 (I - D_1 A_2)^{-1} D_1 B_2 + D_2 \end{bmatrix} \quad (64)$$

where,

$$S_1 = \begin{bmatrix} A_1 & B_1 \\ C_1 & D_1 \end{bmatrix}$$

$$S_2 = \begin{bmatrix} A_2 & B_2 \\ C_2 & D_2 \end{bmatrix}$$

This relation is used recursively until all the S-parameter blocks are exhausted. The S-parameter block definition for the final cascaded matrix of N unit cells by re-arranging the port assignment with the leftward and rightward waves is shown in Figure 3.8. The final cascaded S-parameter matrix representing the end-to-end coupled section can be written as

$$\begin{bmatrix} b_L^O \\ b_R^O \end{bmatrix} = \begin{bmatrix} A_{overall} & B_{overall} \\ C_{overall} & D_{overall} \end{bmatrix} = \left[S_{EQ}^{OVERALL}\right] \begin{bmatrix} a_L^O \\ a_R^O \end{bmatrix} \tag{65}$$

After port re-arrangement ports 1,3,5 and 7 in Figure 3.8 become ports 1, 2, 3 and 4. Similarly ports 2, 4, 6 and 8 in Figure 3.8 become ports 5, 6, 7 and 8. To convert from single-ended to mixed mode S-parameters, it is assumed that each device under test's mixed mode port is being fed from input lines which are not coupled. Ports 1 and 2 form the mixed mode port 1, ports 3 and 4 form the mixed mode port 2, ports 5 and 6 form the mixed mode port 3, and ports 7 and 8 form the mixed mode port 4 for the final cascaded matrix given in (65).

The differential and common mode voltages at ports 1, 2, 3 and 4 can be defined as

$$V_{d_1} = V_1 - V_2 \quad , \quad I_{d_1} = \frac{I_1 - I_2}{2} \quad , \quad V_{c_1} = \frac{V_1 + V_2}{2} \quad , \quad I_{c_1} = I_1 + I_2 \tag{66}$$

$$V_{d_2} = V_3 - V_4 \quad , \quad I_{d_2} = \frac{I_3 - I_4}{2} \quad , \quad V_{c_2} = \frac{V_3 + V_4}{2} \quad , \quad I_{c_2} = I_3 + I_4 \tag{67}$$

$$V_{d_3} = V_5 - V_6 \quad , \quad I_{d_3} = \frac{I_5 - I_6}{2} \quad , \quad V_{c_3} = \frac{V_5 + V_6}{2} \quad , \quad I_{c_3} = I_5 + I_6 \tag{68}$$

$$V_{d_4} = V_7 - V_8 \quad , \quad I_{d_4} = \frac{I_7 - I_8}{2} \quad , \quad V_{c_4} = \frac{V_7 + V_8}{2} \quad , \quad I_{c_4} = I_7 + I_8 \tag{69}$$

The incident and reflected waves for differential and common modes are defined as

$$a_{d_n} = \frac{\left(V_{d_n} + Z_{d_n} I_{d_n}\right)}{2\sqrt{Z_{d_n}}} \quad , \quad b_{d_n} = \frac{\left(V_{d_n} - Z_{d_n} I_{d_n}\right)}{2\sqrt{Z_{d_n}}} \tag{70}$$

$$a_{c_n} = \frac{\left(V_{c_n} + Z_{c_n} I_{c_n}\right)}{2\sqrt{Z_{c_n}}} \quad , \quad b_{c_n} = \frac{\left(V_{c_n} - Z_{c_n} I_{c_n}\right)}{2\sqrt{Z_{c_n}}} \tag{71}$$

where V_{d_n} and I_{d_n} are the differential mode voltage and current at port n . V_{c_n} and I_{c_n} are the common mode voltage and current at port n . Z_{d_n} and Z_{c_n} are differential and common mode port impedances at port n.

To convert from single-ended to mixed mode S-parameters, it is assumed that DUT's each mixed mode port is being fed from input lines which are not coupled. Mathematical meaning of no coupling between the input feed lines is explained below.

The 3-conductor MTL equations are given as

$$\frac{d}{dz}\left[\hat{V}_z\right] = -\left[\hat{R} + j\omega\hat{L}\right]\left[\hat{I}_z\right] = -\left[\hat{Z}\right]\left[\hat{I}_z\right] \tag{72}$$

$$\frac{d}{dz}\left[\hat{I}_z\right] = -\left[\hat{G} + j\omega\hat{C}\right]\left[\hat{V}_z\right] = -\left[\hat{Y}\right]\left[\hat{V}_z\right] \tag{73}$$

where,

$$\hat{V}_z = \begin{bmatrix} V_1(z) \\ V_2(z) \end{bmatrix} , \; \hat{I}_z = \begin{bmatrix} I_1(z) \\ I_2(z) \end{bmatrix}$$

$$\hat{Z} = \hat{R} + j\omega\hat{L} \quad , \quad \hat{Y} = \hat{G} + j\omega\hat{C}$$

$\hat{R}$, $\hat{L}$, $\hat{G}$, and $\hat{C}$ are P.U.L RLGC parameter matrices. It is assumed here that feed lines are identical in geometry.

A 3-conductor system can have two fundamental modes of propagation. One of the modes is a odd mode propagation(when lines are driven in opposite phase) and other is a even mode propagation(when lines are driven in same phase) as shown in Figure 3.9.

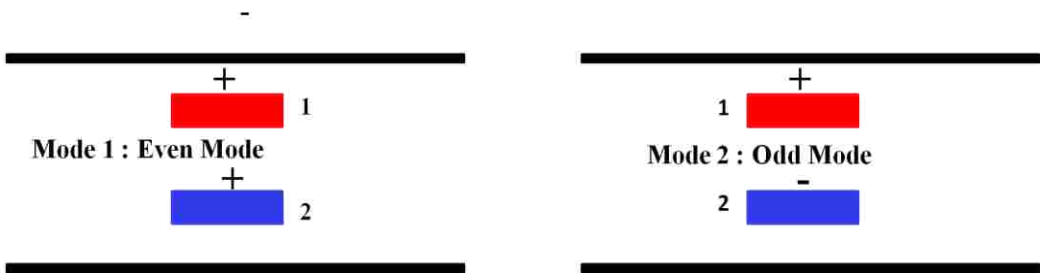

Figure 3.9. The description of fundamental modes that exist in a 3-conductor system

The definition of odd mode characteristic impedance for 3-conductor Tx-line system is given as

$$Z_{0O} = \sqrt{\frac{Z_{11} - Z_{12}}{Y_{11} - Y_{12}}} = \sqrt{\frac{Z_{11}\left(1 - \frac{Z_{12}}{Z_{11}}\right)}{Y_{11}\left(1 - \frac{Y_{12}}{Y_{11}}\right)}} \tag{74}$$

The definition of even mode characteristic impedance for 3-conductor Tx-line system is given as

$$Z_{0E} = \sqrt{\frac{Z_{11} + Z_{12}}{Y_{11} + Y_{12}}} = \sqrt{\frac{Z_{11}\left(1 + \frac{Z_{12}}{Z_{11}}\right)}{Y_{11}\left(1 + \frac{Y_{12}}{Y_{11}}\right)}} \tag{75}$$

The definition of uncoupled characteristic impedance for 2-conductor Tx-line system is given as

$$Z_{0_n} = \sqrt{\frac{Z_{11}}{Y_{11}}} \tag{76}$$

No coupling between the two signal conductors implies

$$\frac{Z_{12}}{Z_{11}} \leq\leq 1 \quad , \quad \frac{Y_{12}}{Y_{11}} \leq\leq 1 \tag{77}$$

Therefore, the odd mode and even mode impedances become equal to each other

$$Z_{0O} = Z_{0E} = Z_{0_n} \tag{78}$$

The differential and common mode port impedances can be computed as

$$Z_{d_n} = 2Z_{0O} \quad , \quad Z_{c_n} = \frac{Z_{0E}}{2} \tag{79}$$

Using the above assumption, the incident and reflected waves for mixed mode ports in terms of incident and reflected waves of single-ended ports is given as

$$\begin{bmatrix} a_{d_1} \\ a_{d_2} \\ a_{d_3} \\ a_{d_4} \\ a_{c_1} \\ a_{c_2} \\ a_{c_3} \\ a_{c_4} \end{bmatrix} = M \begin{bmatrix} a_1 \\ a_2 \\ a_3 \\ a_4 \\ a_5 \\ a_6 \\ a_7 \\ a_8 \end{bmatrix} \quad , \quad \begin{bmatrix} b_{d_1} \\ b_{d_2} \\ b_{d_3} \\ b_{d_4} \\ b_{c_1} \\ b_{c_2} \\ b_{c_3} \\ b_{c_4} \end{bmatrix} = M \begin{bmatrix} b_1 \\ b_2 \\ b_3 \\ b_4 \\ b_5 \\ b_6 \\ b_7 \\ b_8 \end{bmatrix} \tag{80}$$

where,

$$M = \frac{1}{\sqrt{2}} \begin{bmatrix} P & Q \\ R & S \end{bmatrix}$$

$$P = \begin{bmatrix} 1 & -1 & 0 & 0 \\ 0 & 0 & 1 & -1 \\ 0 & 0 & 0 & 0 \\ 0 & 0 & 0 & 0 \end{bmatrix} \quad , \quad Q = \begin{bmatrix} 0 & 0 & 0 & 0 \\ 0 & 0 & 0 & 0 \\ 1 & -1 & 0 & 0 \\ 0 & 0 & 1 & -1 \end{bmatrix}$$

$$R = \begin{bmatrix} 1 & 1 & 0 & 0 \\ 0 & 0 & 1 & 1 \\ 0 & 0 & 0 & 0 \\ 0 & 0 & 0 & 0 \end{bmatrix} \quad , \quad S = \begin{bmatrix} 0 & 0 & 0 & 0 \\ 0 & 0 & 0 & 0 \\ 1 & 1 & 0 & 0 \\ 0 & 0 & 1 & 1 \end{bmatrix}$$

Mixed-mode S-parameters are obtained from the single-ended S-parameters using the transformation M.

$$S_{mmEQ}^{OVERALL} = MS_{EQ}^{OVERALL} M^{-1} \tag{81}$$

The relation between the incident and reflected mixed-mode waves is given as

$$\begin{bmatrix} b_{d_1} \\ b_{d_2} \\ b_{d_3} \\ b_{d_4} \\ b_{c_1} \\ b_{c_2} \\ b_{c_3} \\ b_{c_4} \end{bmatrix} = S_{mmEQ}^{OVERALL} \begin{bmatrix} a_{d_1} \\ a_{d_2} \\ a_{d_3} \\ a_{d_4} \\ a_{c_1} \\ a_{c_2} \\ a_{c_3} \\ a_{c_4} \end{bmatrix} \tag{82}$$

The matrix elements of mixed mode S-parameter matrix are rearranged as

$$\begin{bmatrix} b_{d_1} \\ b_{c_1} \\ b_{d_2} \\ b_{c_2} \\ b_{d_3} \\ b_{c_3} \\ b_{d_4} \\ b_{c_4} \end{bmatrix} = \begin{bmatrix} A & B \\ C & D \end{bmatrix} \begin{bmatrix} a_{d_1} \\ a_{c_1} \\ a_{d_2} \\ a_{c_2} \\ a_{d_3} \\ a_{c_3} \\ a_{d_4} \\ a_{c_4} \end{bmatrix} \tag{83}$$

Boundary condition satisfied at the load is

$$\begin{bmatrix} a_{d_3} \\ a_{c_3} \\ a_{d_4} \\ a_{c_4} \end{bmatrix} = [S_{LOAD}]^{MM} \begin{bmatrix} b_{d_3} \\ b_{c_3} \\ b_{d_4} \\ b_{c_4} \end{bmatrix} \tag{84}$$

where,

$$[S_{LOAD}]^{MM} = \left(\hat{Z}_{LOAD}^{MM} + \hat{Z}_0^{MM}\right)^{-1}\left(\hat{Z}_{LOAD}^{MM} - \hat{Z}_0^{MM}\right)$$

$$\left[\hat{Z}_{LOAD}\right]^{ODD-EVEN} = (M')\left(\hat{Z}_{LOAD}\right)(M')^{-1}$$

$$M' = \frac{1}{\sqrt{2}}\begin{bmatrix} P' & 0 \\ 0 & P' \end{bmatrix}$$

$$P' = \begin{bmatrix} 1 & -1 \\ 1 & 1 \end{bmatrix}$$

$$\hat{Z}_{LOAD}^{MM}(i,j)_{j=1,3} = 2\left[\hat{Z}_{LOAD}\right]^{ODD-EVEN}(i,j)_{j=1,3}$$

$$\hat{Z}_{LOAD}^{MM}(i,j)_{j=2,4} = 0.5\left[\hat{Z}_{LOAD}\right]^{ODD-EVEN}(i,j)_{j=2,4}$$

$$\hat{Z}_0^{MM} = \begin{bmatrix} \hat{Z}_1^{mm} & 0 \\ 0 & \hat{Z}_2^{mm} \end{bmatrix}$$

$$\hat{Z}_1^{mm} = \begin{bmatrix} 2Z_{0_3} & 0 \\ 0 & 0.5Z_{0_3} \end{bmatrix} \quad , \quad \hat{Z}_2^{mm} = \begin{bmatrix} 2Z_{0_4} & 0 \\ 0 & 0.5Z_{0_4} \end{bmatrix}$$

where Z_{0_n} is line impedance of each of uncoupled feed lines forming the mixed mode port n.

Total differential mode and common mode voltages at mixed mode ports 3 and 4 are given as

$$\begin{bmatrix} V_{d_3} \\ V_{c_3} \\ V_{d_4} \\ V_{c_4} \end{bmatrix} = \left(\begin{bmatrix} F_1 & 0 \\ 0 & F_2 \end{bmatrix} \begin{bmatrix} a_{d_3} \\ a_{c_3} \\ a_{d_4} \\ a_{c_4} \end{bmatrix} + \begin{bmatrix} F_1 & 0 \\ 0 & F_2 \end{bmatrix} \begin{bmatrix} b_{d_3} \\ b_{c_3} \\ b_{d_4} \\ b_{c_4} \end{bmatrix} \right) \tag{85}$$

where,

$$F_1 = \begin{bmatrix} \sqrt{2Z_{0_3}} & 0 \\ 0 & \sqrt{\dfrac{Z_{0_3}}{2}} \end{bmatrix} , \quad F_2 = \begin{bmatrix} \sqrt{2Z_{0_4}} & 0 \\ 0 & \sqrt{\dfrac{Z_{0_4}}{2}} \end{bmatrix}$$

Total differential mode and common mode currents at mixed mode ports 3 and 4 are given as

$$\begin{bmatrix} I_{d_3} \\ I_{c_3} \\ I_{d_4} \\ I_{c_4} \end{bmatrix} = \left(\begin{bmatrix} F_3 & 0 \\ 0 & F_4 \end{bmatrix} \begin{bmatrix} a_{d_3} \\ a_{c_3} \\ a_{d_4} \\ a_{c_4} \end{bmatrix} - \begin{bmatrix} F_3 & 0 \\ 0 & F_4 \end{bmatrix} \begin{bmatrix} b_{d_3} \\ b_{c_3} \\ b_{d_4} \\ b_{c_4} \end{bmatrix} \right) \tag{86}$$

where,

$$F_3 = \begin{bmatrix} \frac{1}{\sqrt{2Z_{0_3}}} & 0 \\ 0 & \sqrt{\frac{2}{Z_{0_3}}} \end{bmatrix}, \; F_4 = \begin{bmatrix} \frac{1}{\sqrt{2Z_{0_4}}} & 0 \\ 0 & \sqrt{\frac{2}{Z_{0_4}}} \end{bmatrix}$$

Boundary condition satisfied at the source is

$$\begin{bmatrix} V_{d_1}^S \\ V_{c_1}^S \\ V_{d_2}^S \\ V_{c_2}^S \end{bmatrix} = \begin{bmatrix} V_{d_1} \\ V_{c_1} \\ V_{d_2} \\ V_{c_2} \end{bmatrix} + \left[\hat{Z}_{SOURCE}\right]^{MM} \begin{bmatrix} I_{d_1} \\ I_{c_1} \\ I_{d_2} \\ I_{c_2} \end{bmatrix} \tag{87}$$

where,

$$\left[\hat{Z}_{SOURCE}\right]^{ODD-EVEN} = (M')\left(\hat{Z}_{SOURCE}\right)(M')^{-1}$$

$$\hat{Z}_{SOURCE}^{MM}(i,j)_{j=1,3} = 2\left[\hat{Z}_{SOURCE}\right]^{ODD-EVEN}(i,j)_{j=1,3}$$

$$\hat{Z}_{SOURCE}^{MM}(i,j)_{j=2,4} = 0.5\left[\hat{Z}_{SOURCE}\right]^{ODD-EVEN}(i,j)_{j=2,4}$$

Total differential mode and common mode voltages at mixed modes port 1 and port 2 are given as

$$\begin{bmatrix} V_{d_1} \\ V_{c_1} \\ V_{d_2} \\ V_{c_2} \end{bmatrix} = \left(\begin{bmatrix} F_5 & 0 \\ 0 & F_6 \end{bmatrix} \begin{bmatrix} a_{d_1} \\ a_{c_1} \\ a_{d_2} \\ a_{c_2} \end{bmatrix} + \begin{bmatrix} F_5 & 0 \\ 0 & F_6 \end{bmatrix} \begin{bmatrix} b_{d_1} \\ b_{c_1} \\ b_{d_2} \\ b_{c_2} \end{bmatrix} \right) \tag{88}$$

where,

$$F_5 = \begin{bmatrix} \sqrt{2Z_{0_1}} & 0 \\ 0 & \sqrt{\frac{Z_{0_1}}{2}} \end{bmatrix}, \; F_6 = \begin{bmatrix} \sqrt{2Z_{0_2}} & 0 \\ 0 & \sqrt{\frac{Z_{0_2}}{2}} \end{bmatrix}$$

Total differential mode and common mode currents at mixed mode ports 1 and 2 are given as

$$\begin{bmatrix} I_{d_1} \\ I_{c_1} \\ I_{d_2} \\ I_{c_2} \end{bmatrix} = \left(\begin{bmatrix} F_7 & 0 \\ 0 & F_8 \end{bmatrix} \begin{bmatrix} a_{d_1} \\ a_{c_1} \\ a_{d_2} \\ a_{c_2} \end{bmatrix} - \begin{bmatrix} F_7 & 0 \\ 0 & F_8 \end{bmatrix} \begin{bmatrix} b_{d_1} \\ b_{c_1} \\ b_{d_2} \\ b_{c_2} \end{bmatrix} \right) \tag{89}$$

where,

$$F_7 = \begin{bmatrix} \frac{1}{\sqrt{2Z_{0_1}}} & 0 \\ 0 & \sqrt{\frac{2}{Z_{0_1}}} \end{bmatrix}, \; F_8 = \begin{bmatrix} \frac{1}{\sqrt{2Z_{0_2}}} & 0 \\ 0 & \sqrt{\frac{2}{Z_{0_2}}} \end{bmatrix}$$

Substituting (88) and (89) in (87)

$$\begin{bmatrix} V_{d_1}^S \\ V_{c_1}^S \\ V_{d_2}^S \\ V_{c_2}^S \end{bmatrix} = [G] \begin{bmatrix} a_{d_1} \\ a_{c_1} \\ a_{d_2} \\ a_{c_2} \end{bmatrix} + [H] \begin{bmatrix} b_{d_1} \\ b_{c_1} \\ b_{d_2} \\ b_{c_2} \end{bmatrix} \tag{90}$$

where,

$$[G] = \left(\begin{bmatrix} F_5 & 0 \\ 0 & F_6 \end{bmatrix} + [\hat{Z}_{SOURCE}]^{MM} \begin{bmatrix} F_7 & 0 \\ 0 & F_8 \end{bmatrix} \right)$$

$$[H] = \left(\begin{bmatrix} F_5 & 0 \\ 0 & F_6 \end{bmatrix} - [\hat{Z}_{SOURCE}]^{MM} \begin{bmatrix} F_7 & 0 \\ 0 & F_8 \end{bmatrix} \right)$$

Equations (85) and (86) can be re-written by using relation in equation (84)

$$\begin{bmatrix} V_{d_3} \\ V_{c_3} \\ V_{d_4} \\ V_{c_4} \end{bmatrix} = \begin{bmatrix} F_1 & 0 \\ 0 & F_2 \end{bmatrix} \left([S_{LOAD}]^{MM} + [I] \right) \begin{bmatrix} b_{d_3} \\ b_{c_3} \\ b_{d_4} \\ b_{c_4} \end{bmatrix} \tag{91}$$

$$\begin{bmatrix} I_{d_3} \\ I_{c_3} \\ I_{d_4} \\ I_{c_4} \end{bmatrix} = \begin{bmatrix} F_3 & 0 \\ 0 & F_4 \end{bmatrix} \left([S_{LOAD}]^{MM} - [I] \right) \begin{bmatrix} b_{d_3} \\ b_{c_3} \\ b_{d_4} \\ b_{c_4} \end{bmatrix} \tag{92}$$

From equation (83)

$$\begin{bmatrix} b_{d_3} \\ b_{c_3} \\ b_{d_4} \\ b_{c_4} \end{bmatrix} = [C] \begin{bmatrix} a_{d_1} \\ a_{c_1} \\ a_{d_2} \\ a_{c_2} \end{bmatrix} + [D] \begin{bmatrix} a_{d_3} \\ a_{c_3} \\ a_{d_4} \\ a_{c_4} \end{bmatrix} \tag{93}$$

$$\begin{bmatrix} b_{d_3} \\ b_{c_3} \\ b_{d_4} \\ b_{c_4} \end{bmatrix} = [C] \begin{bmatrix} a_{d_1} \\ a_{c_1} \\ a_{d_2} \\ a_{c_2} \end{bmatrix} + [D][S_{LOAD}]^{MM} \begin{bmatrix} b_{d_3} \\ b_{c_3} \\ b_{d_4} \\ b_{c_4} \end{bmatrix} \tag{94}$$

$$\begin{bmatrix} b_{d_3} \\ b_{c_3} \\ b_{d_4} \\ b_{c_4} \end{bmatrix} = \left([I] - [D][S_{LOAD}]^{MM}\right)^{-1} [C] \begin{bmatrix} a_{d_1} \\ a_{c_1} \\ a_{d_2} \\ a_{c_2} \end{bmatrix} \tag{95}$$

Similarly from equation (83)

$$\begin{bmatrix} b_{d_1} \\ b_{c_1} \\ b_{d_2} \\ b_{c_2} \end{bmatrix} = [A] \begin{bmatrix} a_{d_1} \\ a_{c_1} \\ a_{d_2} \\ a_{c_2} \end{bmatrix} + [B] \begin{bmatrix} a_{d_3} \\ a_{c_3} \\ a_{d_4} \\ a_{c_4} \end{bmatrix} \tag{96}$$

$$\begin{bmatrix} b_{d_1} \\ b_{c_1} \\ b_{d_2} \\ b_{c_2} \end{bmatrix} = \left([A] + [B][S_{LOAD}]^{MM} \left([I] - [D][S_{LOAD}]^{MM}\right)^{-1} [C] \right) \begin{bmatrix} a_{d_1} \\ a_{c_1} \\ a_{d_2} \\ a_{c_2} \end{bmatrix} \tag{97}$$

Substituting equation (97) in equation (90)

$$\begin{bmatrix} a_{d_1} \\ a_{c_1} \\ a_{d_2} \\ a_{c_2} \end{bmatrix} = ([G]+[H][J])^{-1} \begin{bmatrix} V_{d_1}^S \\ V_{c_1}^S \\ V_{d_2}^S \\ V_{c_2}^S \end{bmatrix} \tag{98}$$

where,

$$[J] = \left([A]+[B][S_{LOAD}]^{MM} \left([I]-[D][S_{LOAD}]^{MM} \right)^{-1} [C] \right)$$

Define matrix P as

$$[P] = ([G]+[H][J])^{-1} \tag{99}$$

Equation (98) can be re-written as

$$\begin{bmatrix} a_{d_1} \\ a_{c_1} \\ a_{d_2} \\ a_{c_2} \end{bmatrix} = [P] \begin{bmatrix} V_{d_1}^S \\ V_{c_1}^S \\ V_{d_2}^S \\ V_{c_2}^S \end{bmatrix} \tag{100}$$

Substituting equation (100) in equation (95)

$$\begin{bmatrix} b_{d_3} \\ b_{c_3} \\ b_{d_4} \\ b_{c_4} \end{bmatrix} = \left([I]-[D][S_{LOAD}]^{MM} \right)^{-1} [C][P] \begin{bmatrix} V_{d_1}^S \\ V_{c_1}^S \\ V_{d_2}^S \\ V_{c_2}^S \end{bmatrix} \tag{101}$$

Substituting equation (101) in equations (91) and (92)

$$\begin{bmatrix} V_{d_3} \\ V_{c_3} \\ V_{d_4} \\ V_{c_4} \end{bmatrix} = \begin{bmatrix} F_1 & 0 \\ 0 & F_2 \end{bmatrix} \left([S_{LOAD}]^{MM} + [I] \right) \left([I] - [D][S_{LOAD}]^{MM} \right)^{-1} [C][P] \begin{bmatrix} V_{d_1}^S \\ V_{c_1}^S \\ V_{d_2}^S \\ V_{c_2}^S \end{bmatrix} \quad (102)$$

$$\begin{bmatrix} I_{d_3} \\ I_{c_3} \\ I_{d_4} \\ I_{c_4} \end{bmatrix} = \begin{bmatrix} F_3 & 0 \\ 0 & F_4 \end{bmatrix} \left([S_{LOAD}]^{MM} - [I] \right) \left([I] - [D][S_{LOAD}]^{MM} \right)^{-1} [C][P] \begin{bmatrix} V_{d_1}^S \\ V_{c_1}^S \\ V_{d_2}^S \\ V_{c_2}^S \end{bmatrix} \quad (103)$$

Substituting equations (100) and (97) in (88) and (89)

$$\begin{bmatrix} V_{d_1} \\ V_{c_1} \\ V_{d_2} \\ V_{c_2} \end{bmatrix} = \begin{bmatrix} F_5 & 0 \\ 0 & F_6 \end{bmatrix} ([I] + [J])[P] \begin{bmatrix} V_{d_1}^S \\ V_{c_1}^S \\ V_{d_2}^S \\ V_{c_2}^S \end{bmatrix} \quad (104)$$

$$\begin{bmatrix} I_{d_1} \\ I_{c_1} \\ I_{d_2} \\ I_{c_2} \end{bmatrix} = \begin{bmatrix} F_7 & 0 \\ 0 & F_8 \end{bmatrix} ([I] - [J])[P] \begin{bmatrix} V_{d_1}^S \\ V_{c_1}^S \\ V_{d_2}^S \\ V_{c_2}^S \end{bmatrix} \quad (105)$$

Equation (102) and (104) can be re-written as

$$\begin{bmatrix} V_{d_3} \\ V_{c_4} \\ V_{d_4} \\ V_{c_4} \end{bmatrix} = \begin{bmatrix} \hat{X}_{31} & \hat{X}_{32} \\ \hat{X}_{41} & \hat{X}_{42} \end{bmatrix} \begin{bmatrix} V_{d_1}^S \\ V_{c_1}^S \\ V_{d_2}^S \\ V_{c_2}^S \end{bmatrix} \tag{106}$$

where,

$$\begin{bmatrix} \hat{X}_{31} & \hat{X}_{32} \\ \hat{X}_{41} & \hat{X}_{42} \end{bmatrix} = \begin{bmatrix} F_1 & 0 \\ 0 & F_2 \end{bmatrix} \left([S_{LOAD}]^{MM} + [I] \right) \left([I] - [D][S_{LOAD}]^{MM} \right)^{-1} [C][P]$$

$$\hat{X}_{31} = \begin{bmatrix} X_{31}^{DD} & X_{31}^{DC} \\ X_{31}^{CD} & X_{31}^{CC} \end{bmatrix}, \; \hat{X}_{32} = \begin{bmatrix} X_{32}^{DD} & X_{32}^{DC} \\ X_{32}^{CD} & X_{32}^{CC} \end{bmatrix}$$

$$\hat{X}_{41} = \begin{bmatrix} X_{41}^{DD} & X_{41}^{DC} \\ X_{41}^{CD} & X_{41}^{CC} \end{bmatrix}, \; \hat{X}_{42} = \begin{bmatrix} X_{42}^{DD} & X_{42}^{DC} \\ X_{42}^{CD} & X_{42}^{CC} \end{bmatrix}$$

Equation (104) can be re-written as

$$\begin{bmatrix} V_{d_1} \\ V_{c_1} \\ V_{d_2} \\ V_{c_2} \end{bmatrix} = \begin{bmatrix} \hat{X}_{11} & \hat{X}_{12} \\ \hat{X}_{21} & \hat{X}_{22} \end{bmatrix} \begin{bmatrix} V_{d_1}^S \\ V_{c_1}^S \\ V_{d_2}^S \\ V_{c_2}^S \end{bmatrix} \tag{107}$$

where,

$$\begin{bmatrix} \hat{X}_{11} & \hat{X}_{12} \\ \hat{X}_{21} & \hat{X}_{22} \end{bmatrix} = \begin{bmatrix} F_5 & 0 \\ 0 & F_6 \end{bmatrix} \left([I] + [J] \right) [P]$$

$$\hat{X}_{11} = \begin{bmatrix} X_{11}^{DD} & X_{11}^{DC} \\ X_{11}^{CD} & X_{11}^{CC} \end{bmatrix}, \; \hat{X}_{12} = \begin{bmatrix} X_{12}^{DD} & X_{12}^{DC} \\ X_{12}^{CD} & X_{12}^{CC} \end{bmatrix}$$

$$\hat{X}_{21} = \begin{bmatrix} X_{21}^{DD} & X_{21}^{DC} \\ X_{21}^{CD} & X_{21}^{CC} \end{bmatrix}, \; \hat{X}_{22} = \begin{bmatrix} X_{22}^{DD} & X_{22}^{DC} \\ X_{22}^{CD} & X_{22}^{CC} \end{bmatrix}$$

The victim link is not excited with any voltage sources, implying

$$V_{d_2}^S = 0 \quad , \quad V_{c_2}^S = 0 \tag{108}$$

NEXT differential and common mode voltages are

$$V_{d_2} = X_{21}^{DD} V_{d_1}^S + X_{21}^{DC} V_{c_1}^S \tag{109}$$

$$V_{c_2} = X_{21}^{CD} V_{d_1}^S + X_{21}^{CC} V_{c_1}^S \tag{110}$$

THRU differential and common mode voltages are

$$V_{d_3} = X_{31}^{DD} V_{d_1}^S + X_{31}^{DC} V_{c_1}^S \tag{111}$$

$$V_{c_3} = X_{31}^{CD} V_{d_1}^S + X_{31}^{CC} V_{c_1}^S \tag{112}$$

Differential NEXT and THRU voltage transfer functions are given by

$$NEXT = \frac{V_{d_2}}{V_{d_1}^S} = X_{21}^{DD} + X_{21}^{DC} \frac{V_{c_1}^S}{V_{d_1}^S} \tag{113}$$

$$THRU = \frac{V_{d_3}}{V_{d_1}^S} = X_{31}^{DD} + X_{31}^{DC} \frac{V_{c_1}^S}{V_{d_1}^S} \tag{114}$$

Crosstalk metric based on horizontal eye opening can be defined using the NEXT and THRU voltage transfer functions to generate the impulse responses to obtain the statistical BER eye contour shown in Figure 3.10.

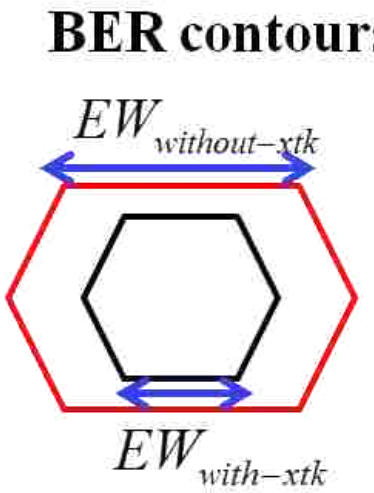

Figure 3.10. The NEXT metric definition based on BER eye contour

The crosstalk metric based on horizontal eye opening is defined as

$$XTK - impact\% = \frac{EW_{without-xtk} - EW_{with-xtk}}{EW_{without-xtk}} \times 100\% \tag{115}$$

The crosstalk metric defined in equation (115) has one to one mapping relation with the THRU and XTK voltage transfer functions. The reason being that the impulse response required to generate the BER eye contours is obtained by taking inverse Fourier transform of voltage transfer function. Inverse Fourier transform is a linear operator and so the transformation between the two crosstalk metric is also linear.

The test structure shown in Figure 3.11 is a 5-inch broadside differential angular periodic coupled segment using core and pre-preg dielectric with relative permittivity of 3.7 and loss tangent of 0.025 at 1GHz. The unit cell period is fixed at 500 mils with angle of 45 degrees. The agreement between the overall full wave model and formulation based on a single unit cell is good, as shown in Figure 3.12 and Figure 3.13.

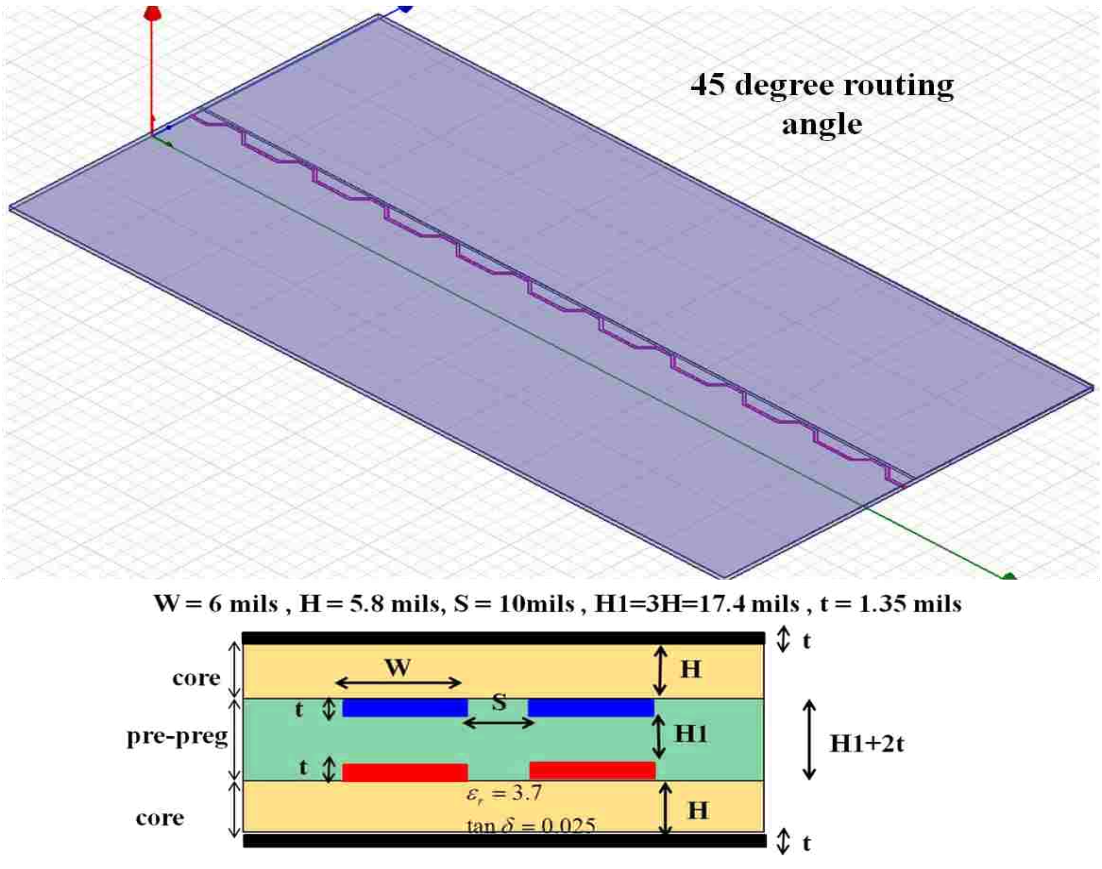

Figure 3.11. Stackup of differential coupled lines of with 10 unit cells at 45-degree angle

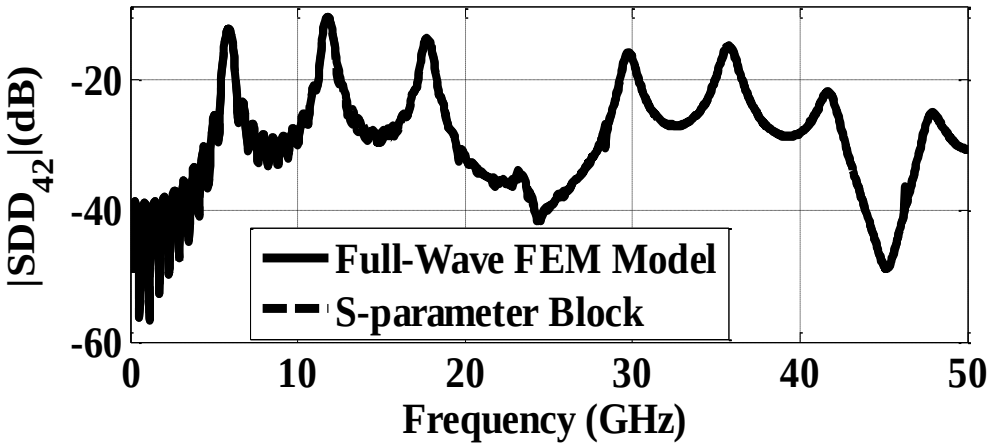

Figure 3.12. Comparison of differential NEXT using single unit cell with overall full-wave model response

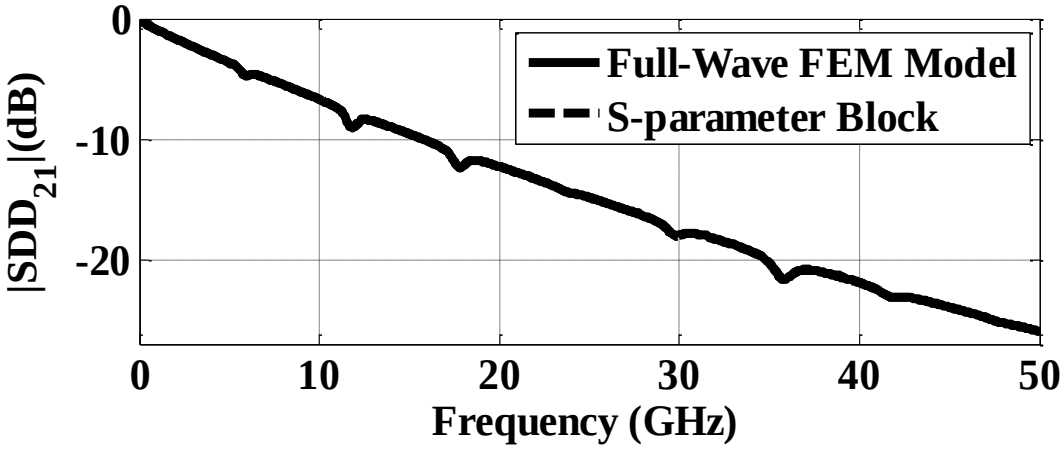

Figure 3.13. Comparison of differential THRU using single unit cell with overall full-wave model response

3.4. VALIDATION OF FLOQUET MODE PHYSICS USING MEASUREMENTS

A test structure was fabricated, shown in Figure 3.14, being a 5-inch broadside differential angular periodic coupled segment using core and pre-preg dielectric with relative permittivity of 4.2 and loss tangent of 0.015 at 1 GHz. The unit cell period is fixed at 500 mils with angle at 45 degrees. The agreement between the overall full wave model and measurement is good, as shown in Figure 3.15 and Figure 3.16.

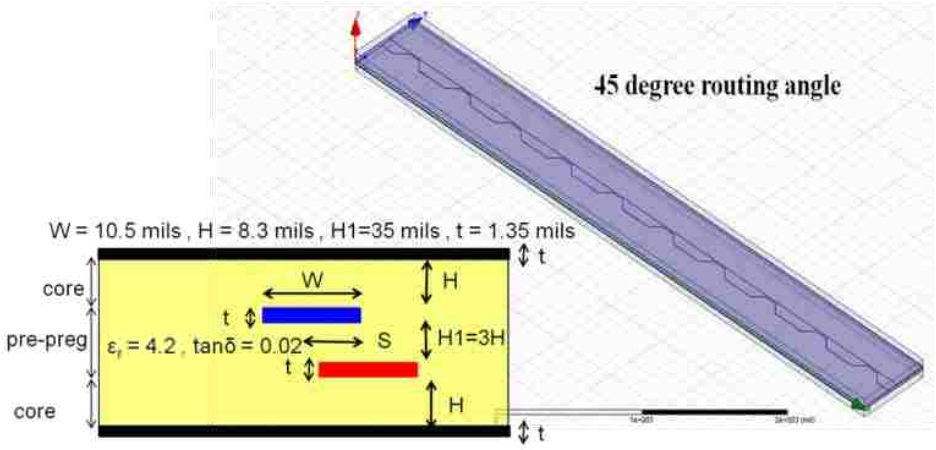

Figure 3.14. Stackup of single-ended broadside coupled lines with 10 periodic unit cells at 45-degree angles fabricated on the PCB

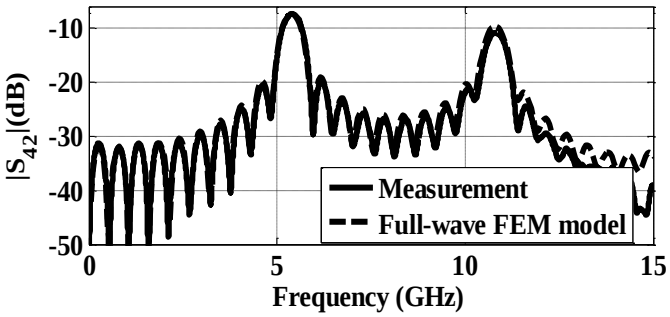

Figure 3.15. Comparison of differential NEXT formulation and measurement

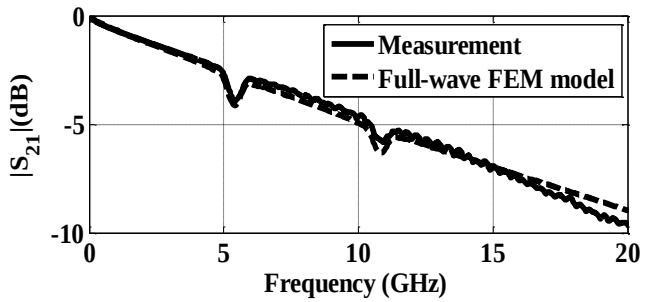

Figure 3.16. Comparison of differential THRU formulation and measurement

3.5. PREDICTION OF FLOQUET MODE RESONANCE LOCATION

For the network shown in Figure 3.8 that represents the geometry of periodic coupled segment shown in Figure 3.17, assuming no losses and reflections at the junctions between the unit cells does not impact the Floquet mode resonance location. The superposition theorem is used to obtain the aggregate near-end crosstalk voltage V_2^{Block1} at receiver differential port 2 when input V_4^{Block1} is applied at differential port 4.

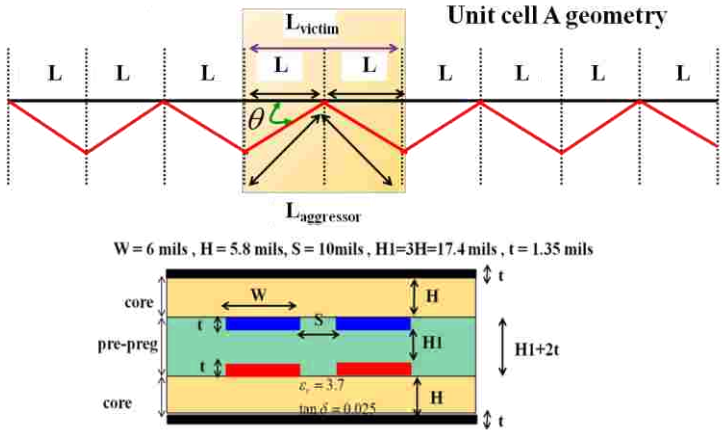

Figure 3.17. Stackup and geometry of the 10-inch periodic coupled segment using unit cell A

$$V_2^{Block1} = \left(S_{dd42}\right)^{Block1}\left(1 + e^{-2j\beta l_{avg}} + \ldots + e^{2j(N-1)\beta l_{avg}}\right)V_4^{Block1} \tag{116}$$

where,

$$S_{dd43}.S_{dd12} \cong e^{-j\beta\left(l_{aggressor}+l_{victim}\right)} = e^{-2j\beta l_{avg}}$$

Maximum crosstalk voltage is coupled to the victim when

$$e^{-2j\beta l_{avg}} = 1 \Rightarrow 2\beta l_{avg} = 2n\pi \tag{117}$$

The Floquet mode resonance location can be obtained from equation (117) in a simplified form as

$$f_{Floquet} = \frac{n}{2t_{delay}} \quad n = 1,2,\ldots \quad , \quad t_{delay} = \frac{l_{avg}}{v} \tag{118}$$

where,

$$l_{avg} = \frac{l_{aggressor} + l_{victim}}{2}, \quad v = \frac{3\times 10^8}{\sqrt{\varepsilon_{eq}}}$$

The delay is 43 ps for the unit cell periodic model with a period of 125 mils for stackup (see Figure 3.17). The Floquet mode resonance location for geometry with unit cell length of 125 mils shown in Figure 3.17. is computed as

$$f = \frac{1}{2t_{delay}} = \frac{1}{43ps} = 23.25GHz \tag{119}$$

The crossing angle is fixed at 30 degrees. The Floquet mode resonance occurs at around 23.5 GHz, as seen from the NEXT frequency response in Figure 3.18. The resonance in the NEXT response is flat and hence the location predicted by the formula with assumptions of no reflections and losses is acceptable. The NEXT frequency response and the step response for the unit cell with periods of 125 and 2000 mils is shown in Figure 3.18 and Figure 3.19.

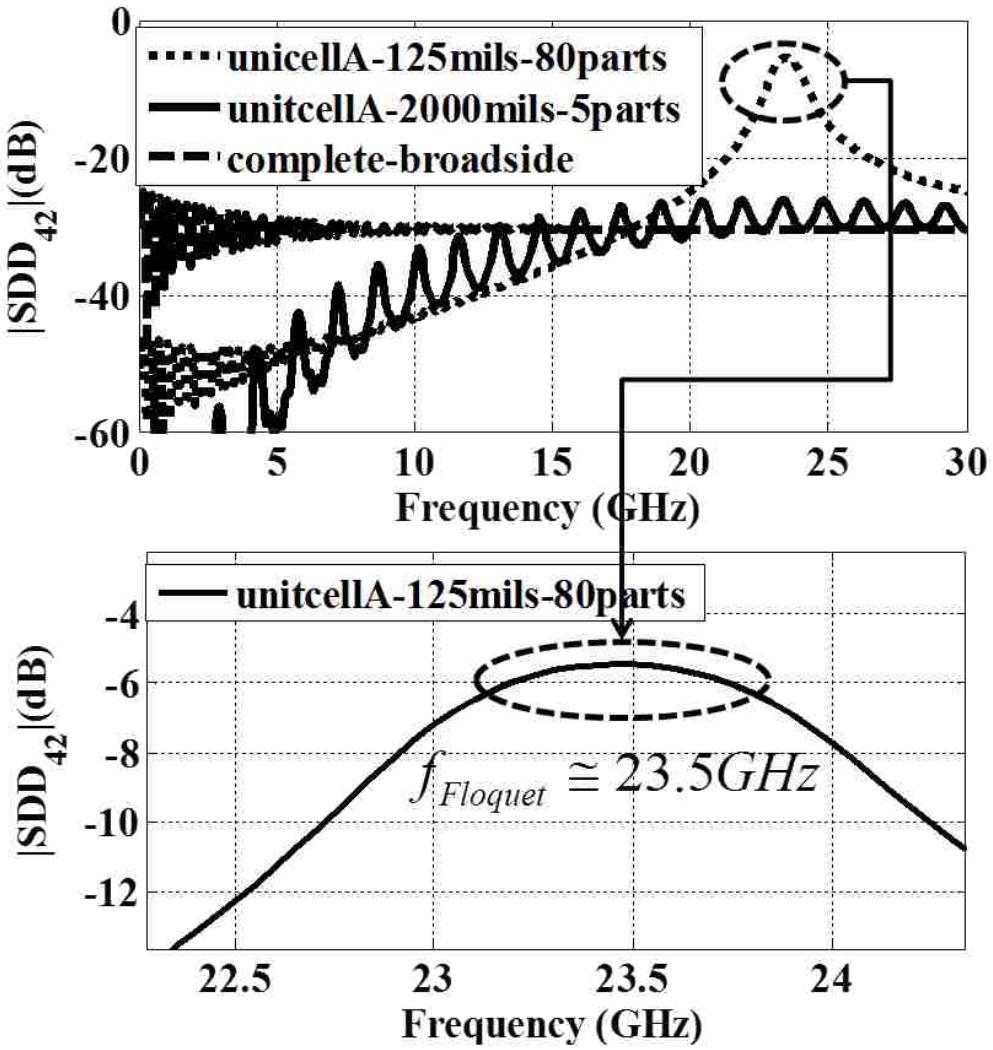

Figure 3.18. Floquet mode resonance observed in NEXT frequency response

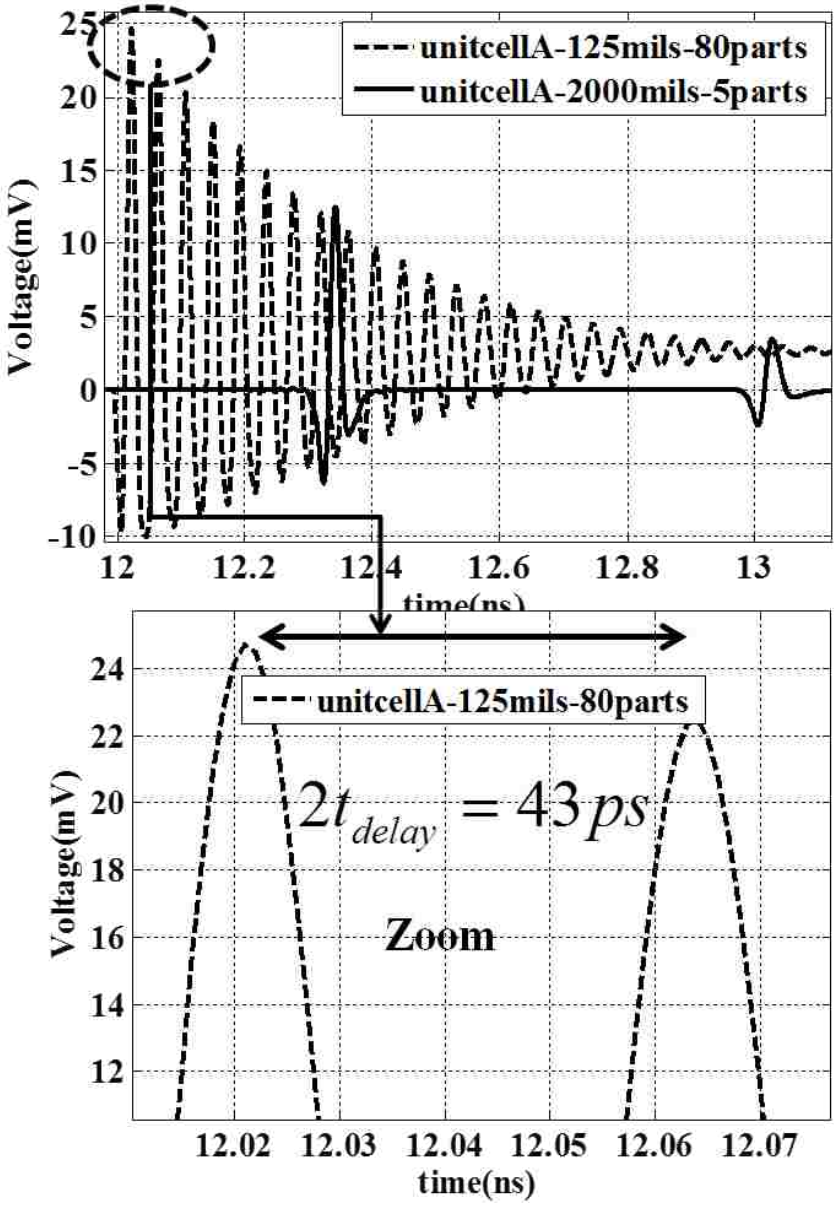

Figure 3.19. Periodic ringing observed in NEXT step response

It can be observed that the delay between the successive pulses in the step response is related to the resonance frequency associated with Floquet mode.

3.6. IMPACT DUE TO NEXT IN PERIODIC COUPLED SEGMENT

The test structure shown in Figure 3.20 is a 10-inch broadside differential angular periodic coupled segment, using core and pre-preg dielectric with relative permittivity of 3.7 and loss tangent of 0.025 at 1 GHz. The unit cell periodicity is fixed at 250 mils with angle of 30 degrees. The periodic segment contains four unit cells followed by 9000 mils of uncoupled segment.

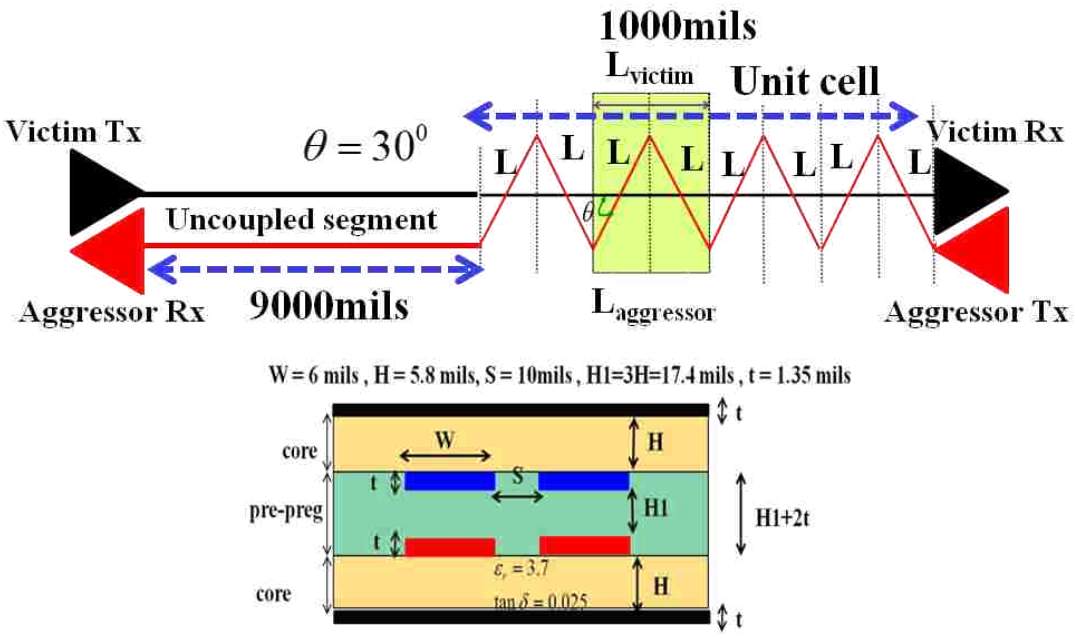

Figure 3.20. Stackup and geometry of the 10 inch periodic coupled segment

A differential input of 500 mV peak-to-peak with a rise/fall time of 30 ps at a data rate of 10 Gbps and rise/fall time of 15 ps at a data rate of 16 Gbps is used on both aggressor and victim. The eye width and eye height of complete broadside and periodic coupled segments are compared at 10 Gbps and 16 Gbps in Table 3.1. It is observed from

NEXT that the frequency response of the periodic model is higher compared to complete broadside coupling above 20 GHz (see Figure 3.21). The higher frequencies contribute to rise time of the signals which manifest to more crosstalk. The impact of NEXT on eye height and eye width at 10 Gbps and 16 Gbps is given in Figure 3.22.

It can be observed from Table 3.1 that the periodic segment with four unit cells has 13 ps of crosstalk-induced jitter compared to 6 ps for 10-inch complete broadside at 16 Gbps. Periodic coupled segments found in practical PCBs have at least four unit cells, and the crosstalk impact cannot be neglected, as observed from the data in Table 3.1. The impact of NEXT from the periodic broadside coupled aggressors on the BER eye contour is severe compared to the NEXT from the complete broadside coupled aggressor. The Floquet modes aggravate the crosstalk, thereby reducing the horizontal eye opening of the BER contour.

Table 3.1. Comparison of crosstalk-induced jitter from periodic coupled segment and complete broadside segment

Geometry	Peak-to-peak jitter (ps)
Complete broadside, aggressor quiet	35
Periodic structure, aggressor quiet	37
Complete broadside, aggressor active	41
Periodic structure, aggressor active	50

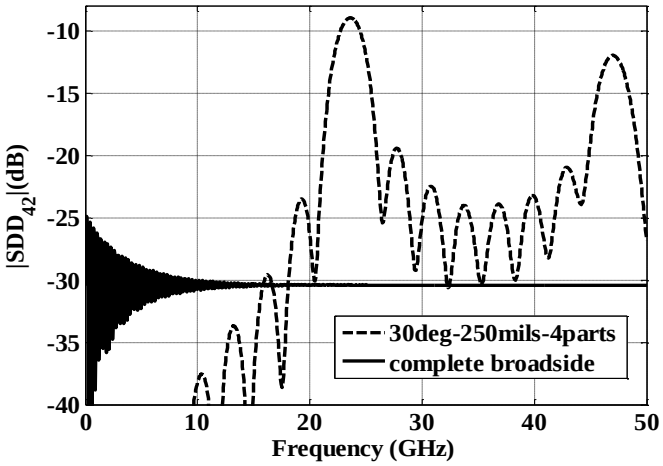

Figure 3.21. NEXT comparison between the periodic coupled segment and complete broadside line

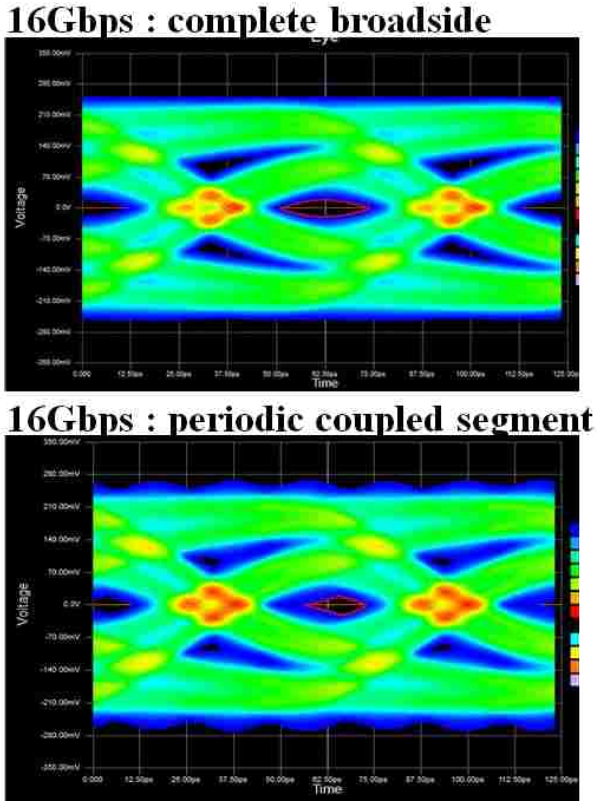

Figure 3.22. Eye opening comparison between periodic coupled segment and complete broadside segment at 16Gbps

3.7. SENSITIVITY OF ROUTING ANGLE, PATTERN TYPE AND LENGTH OF UNIT CELL WITH RESPECT TO EYE OPENING

A 10-inch periodic coupled trace segment using unit cells described in Figure 3.6 using the stackup shown in Figure 3.17 is assembled by varying the period from 125 mils to 2000 mils. The core and pre-preg dielectric with relative permittivity of 3.7 and loss tangent of 0.025 at 1 GHz is used. The crosstalk impact at 10 Gbps and 16 Gbps observed in Figure 3.23 and Figure 3.24 show that as the periodicity of the unit cell increases the impact on the horizontal eye opening decreases for angles above 30 degrees. The deviation in the trend occurs for smaller angles less than 30 degrees. For smaller unit cell periodicity and angles, the overall coupled structure is very close to complete broadside coupled routing. The Floquet mode resonances are very weak in this scenario. As the unit cell periodicity increases for smaller angles, the Floquet mode resonances become dominant. For larger angles in unit cell irrespective of periodicity, Floquet modes are dominant. As the unit cell periodicity increases, the number of unit cells over the entire coupled region decreases, thereby decreasing the crosstalk impact on eye opening. When the unit cell length and angle is small, the zero of the unit cell is close to the Floquet mode pole location (see Figure 3.25). As the zero and pole are close, the peak of the Floquet mode is compromised. As the angle increases, the pole and zero move further apart, which improves the peak of the Floquet mode (see Figure 3.26). As the angle increase above 45 degrees, the coupling is saturated, and so even when the angle is increased the peak does not go up (see Figure 3.27). This clearly explains why smaller angles have a smaller impact on the eye opening at 16 Gbps than larger angles. As the unit cell length is increased, the Floquet resonance is pushed to lower frequencies, which fall within bandwidth of interest. For smaller angles, the effect is predominant, as coupling at smaller angles are stronger, leading to more eye closure as the unit cell length is increased. As the angle increases above 30 degrees, the larger unit cell has lower impact from crosstalk, as the coupling becomes saturated very quickly as unit cell length is increased.

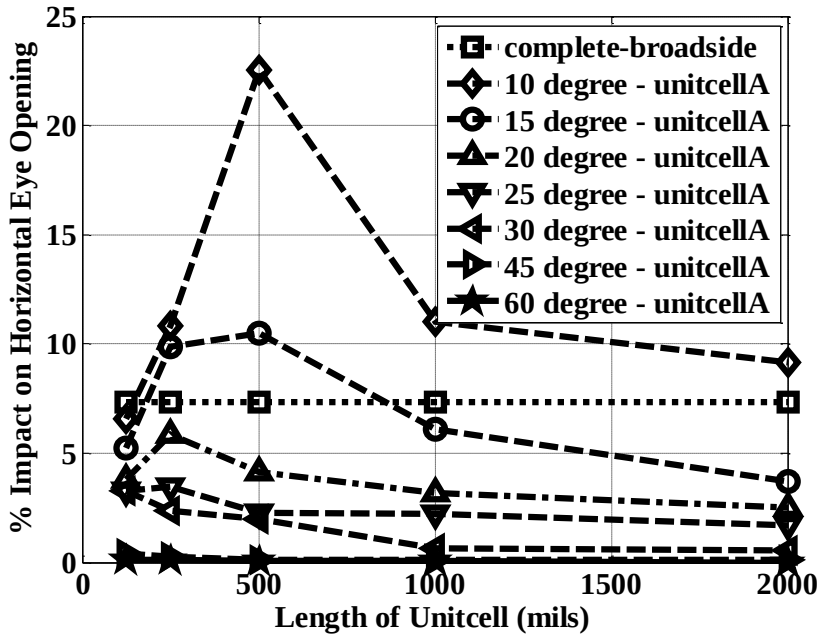

Figure 3.23. Comparison of NEXT impact on eye opening at 10 Gbps by varying angle and period of unit cell A

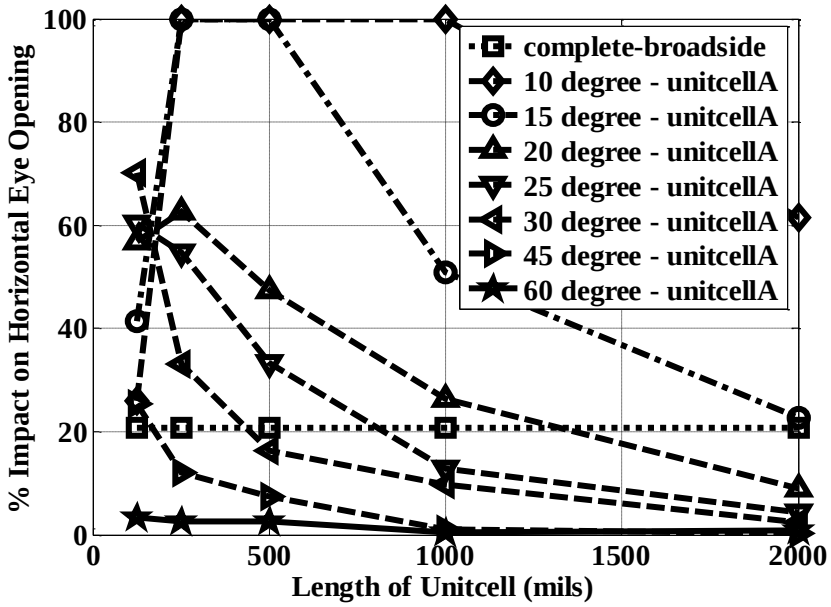

Figure 3.24. Comparison of NEXT impact on eye opening at 16 Gbps by varying angle and period of unit cell A

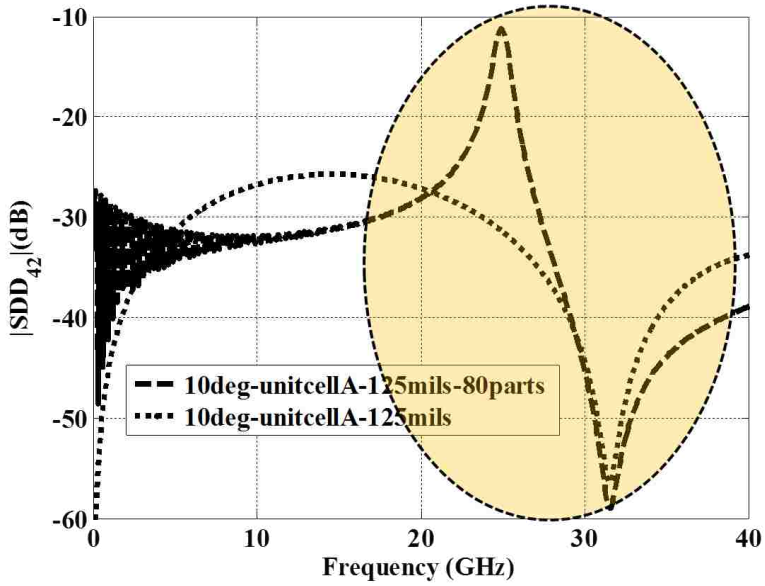

Figure 3.25. Reduction of Floquet resonance pole peak to due to proximity of unit cell zero to the pole

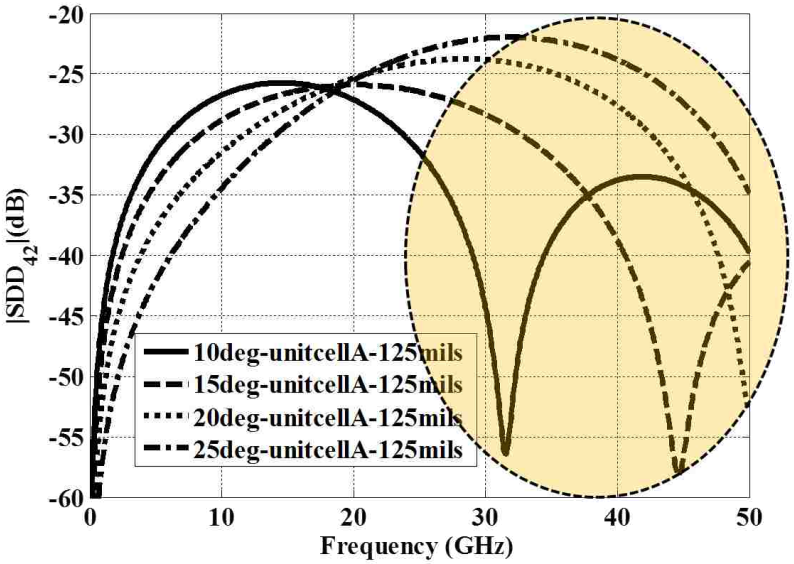

Figure 3.26. Increase in separation between Floquet pole and unit cell zero as angle increases

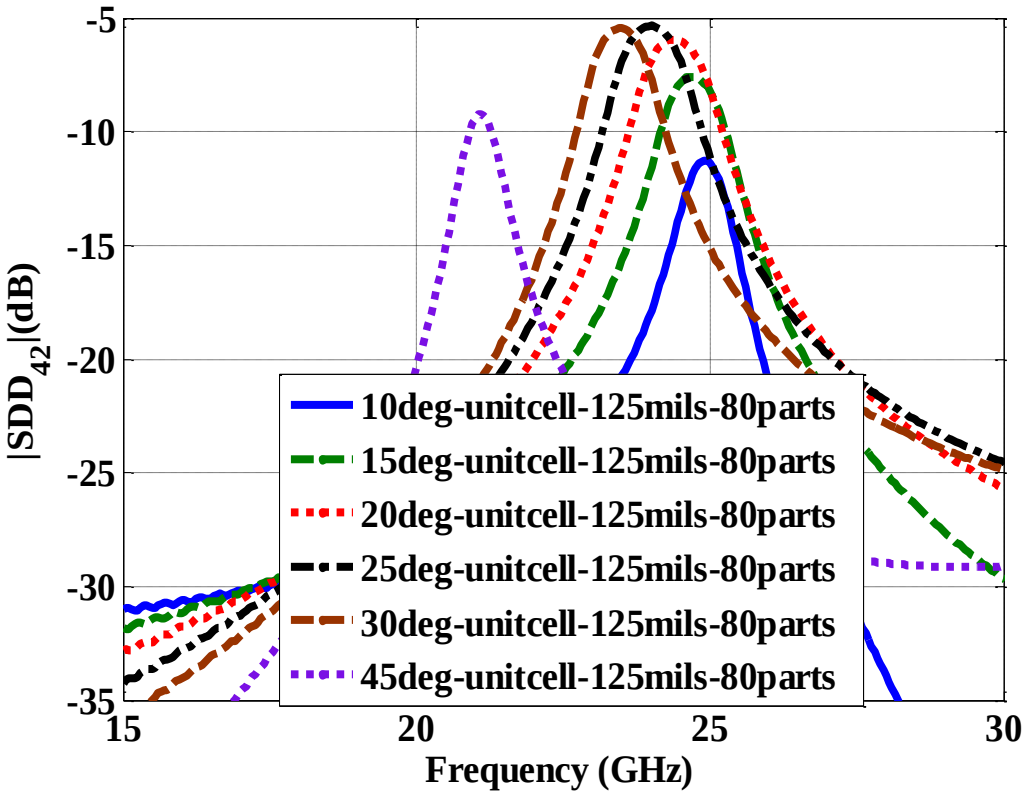

Figure 3.27. Floquet resonance peak amplitude as angle is increased for 125-mil unit cell period

A 10-inch periodic coupled trace segment using the unit cell described in Figure. 7 and the stackup shown in Figure 3.17 is assembled by varying the period from 125 mils to 2000 mils. The core and pre-preg dielectric with relative permittivity of 3.7 and loss tangent of 0.025 at 1 GHz is used. The crosstalk impact at 10 Gbps and 16 Gbps observed in Figure 3.28 and Figure 3.29 follows similar trend as unit cell A, except for the location of Floquet resonance. The Floquet mode resonance for unit cell B of same length as unit cell A occurs exactly at twice the Floquet mode resonance frequency of unit cell A, since the aggressor crosses the victim twice in a single unit cell.

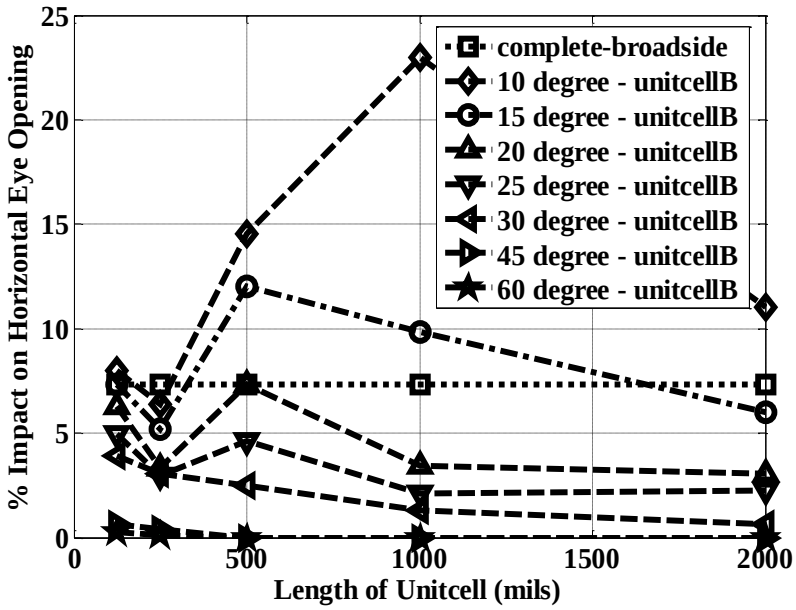

Figure 3.28. Comparison of NEXT impact on eye opening at 10 Gbps by varying angle and period of unit cell B

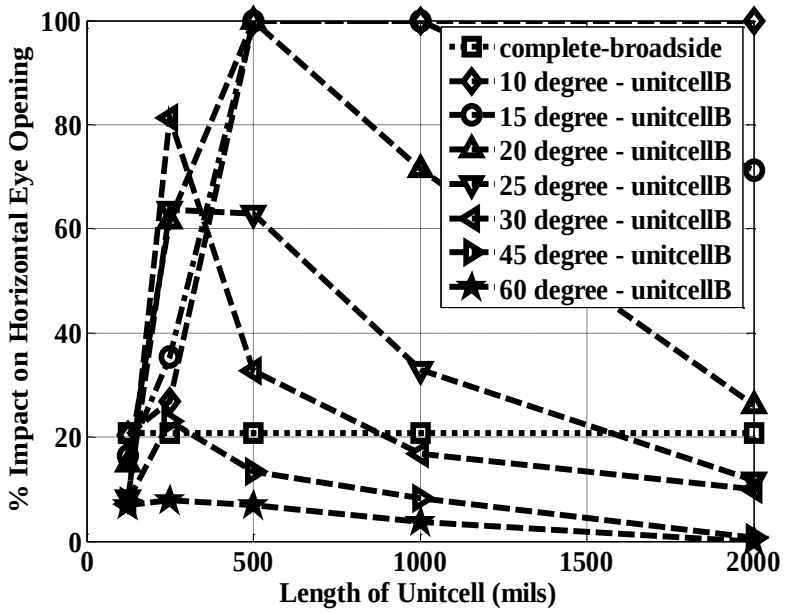

Figure 3.29. Comparison of NEXT impact on eye opening at 16 Gbps by varying angle and period of unit cell B

3.8. CONCLUSIONS

The focus of the paper is to quantify the effect of broadside coupling in terms of BER for various routing topologies commonly observed in practical PCB design. NEXT peaks and THRU dips at frequencies associated with Floquet modes are related to unit cell periodicity. A periodic coupled aggressor with only four periods induced more peak-to-peak crosstalk jitter compared to a complete broadside aggressor for a 10-inch coupled line. The longer the periodicity of the unit cell, the lesser is the impact from crosstalk. For data rates up to 10 Gbps, complete broadside coupled routing is more lethal than periodic, for any periodicity with angles above 15 degrees. It is observed from analyzing the layout of the practical PCBs that period length is less than 500 mils and contain no more than five unit cells. Complete broadside routing is not as lethal as periodic coupled routing, for periodicities above 125 and below 500 mils and for angles up to 30 degrees. It is recommended to use routing angles above 45 degrees to maintain less than 10% impact on horizontal eye opening, irrespective of the period length. It is recommended to exercise caution when increasing the routing angle, as it will increase the length of routing adding more loss. This study may help electrical designers to create a set of routing guidelines that maintain integrity of the channel in the presence of NEXT due to periodic coupled routing.

4. IMPROVED TRANSMITTER JITTER MODELING FOR ACCURATE BIT ERROR RATE (BER) EYE CONTOURS USING TRANSIENT SIMULATION OF SHORT BIT PATTERNS

4.1. INTRODUCTION

Increase in the signaling speeds has led to decrease in jitter budget available for the channel to pass the product specifications. The current specifications are based on a BER metric and hence there is a need to account for jitter statistically. Accurately capturing jitter through the channel is very important to have confidence in the product specifications. Previously, when the data rates were not faster, channel analysis was based on transient analysis to compute the eye opening at the receiver using thousands of bits. With increasing complexity and data rates, it is not possible to predict eye opening with just a few thousands of bits. Transient analysis using a SPICE simulator is the most accurate way of capturing all the non-linearities in the channel, including jitter, non-linear Tx/Rx models, but it is very time consuming to completely characterize the channel through all possible patterns. Worst-case link analysis methods (e.g., peak distortion analysis in [54]) eliminated the need for time consuming simulations by analytically determining the worst-case eye from the channel response and noise models. The results of a worst-case analysis in which the worst-case effects of several noise and interference sources are simply superimposed can be highly pessimistic, since the probability of these occurrences is very low. Due to the drawbacks of transient and worst-case analysis methods, most of the link analysis that has been developed to date ([54]–[70]) are statistical in nature. The early statistical and fast time domain approaches ([54]-[59]) are based on generating the system response to a single bit (pulse) or a step input. The extracted pulse or step response was used to generate the output response of different data patterns. The underlying assumption in these methods is that the system is linear and time-invariant. It is also assumed that rise and fall times are equal in the data patterns simulated. However, these assumptions are not valid, especially when the transmitter has non-linear behavior or the system is not linear. When the pull up and pull down transistors of a Tx are mismatched, the assumption of equal rise and fall times is not valid, giving erroneous results when pulse and step response based methods are used. The

double edge response (DER) approach introduced in [60] solves the unequal rise/fall time issue, but it still assumes that the system is linear and time-invariant. The multiple edge response (MER) introduced in ([64]-[68]) utilizes multiple edges from different bit patterns before the rising/falling step input to account for the system non-linearity, which extends beyond one bit and unequal rise/fall time issues.

Based on the pulse response of the channel, the single bit response (SBR) approach ([54]-[57]) can accurately handle ISI, XTK, Rx jitter modeled using the Dual-Dirac jitter model. The pulse-response approach cannot handle Tx jitter accurately. Tx jitter was modeled as Rx jitter without accounting channel impact on Tx jitter [54, 57]. The pulse response based approach proposed in [54] has been improved in [58, 59] to handle the Tx jitter. The Tx jitter is modeled as equivalent voltage noise that needs to be added to the received pulse response. This approach can account for the jitter amplification through the channel. It cannot handle the non-linear nature of jitter for a non-linear system, especially for large jitter values. The step-response based method proposed in [55-56] handles the Tx jitter more accurately than the pulse-response based methods. The segment-based analysis method using the step-response has a drawback in that Tx jitter in one segment is uncorrelated to the other segments. The effect of ISI from Tx jitter on the successive segments is not captured. Deterministic jitter (DJ) and random jitter are separately handled in [63]. Time domain simulation is used to handle DJ and deals with RJ by extrapolating the bathtub using the Dual-Dirac method. Therefore, jitter amplification of RJ due to the channel is ignored. The multiple edge response (MER) based approach ([64]-[68]) modeled high frequency jitter in the time-domain and low frequency jitter in the statistical domain. In [70], a statistical approach using multiple short bit pattern waveforms is introduced to obtain statistical BER contours. The response of multiple short bit patterns is performed in the time-domain in SPICE. The system non-linearity is handled in this method.

The multi bit response approach [70] did not describe the process to account for Tx jitter. None of the approaches mentioned above accounted for the initial phase of the Tx driver jitter and correlation between the different waveform segments constructed from the fundamental single bit or multiple edge response approaches. The phase and

jitter correlation between different basis waveforms has to be accounted for to get accurate jitter statistics at the output.

The initial phase can take any value in the range of 0 to 2 , especially for sinusoidal periodic jitter. A more rigorous model for Tx jitter with initial phase was introduced in [69]. The method handles Tx jitter in the time-domain by simulating 2m m-bit waveforms. The jitter injected into different waveforms is assumed to be independent of each other. Only a few initial phase points are selected, and no algorithm is described to explain the basis for selecting the initial phase values. The effect of zero correlation and insufficient initial phase values between different waveforms is shown in Figure 4.1. This effect is visible when the channel is low loss since the edges are more distinct. This is also the case when the injected jitter at Tx input is large

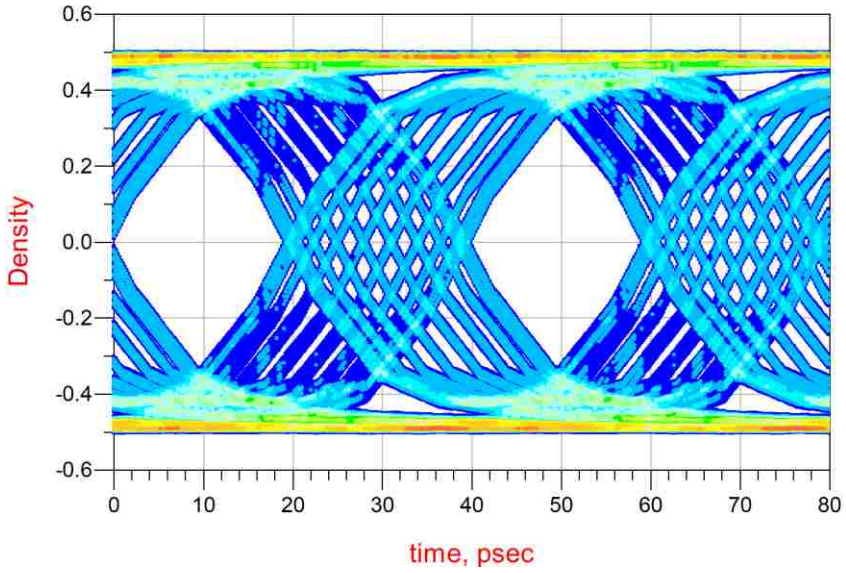

(a)

Figure 4.1. (a) Statistical eye diagram with Tx jitter injection methodology described in [69] (b) Eye diagram with Tx jitter injection by transient simulation of million bits

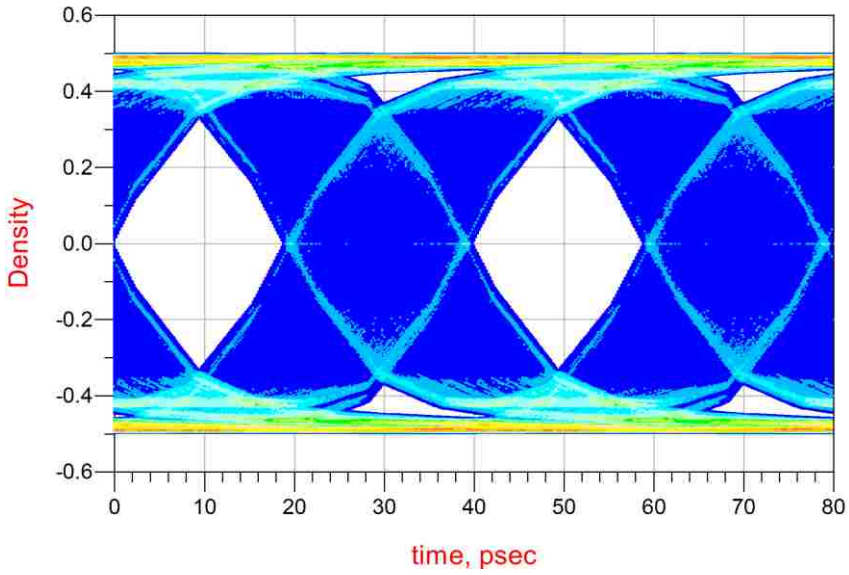

(b)

Figure 4.1. (a) Statistical eye diagram with Tx jitter injection methodology described in [69] (b) Eye diagram with Tx jitter injection by transient simulation of million bits (cont.)

Even though the inner contour of the eye diagrams is similar, the statistics are not same. Finally, all of the statistical link approaches based on single bit response ignore the correlation between the different bit patterns. Once the input bit stream is passed through a pre-coder block, the bits are correlated with each other. The time-domain based approaches described in ([64] - [70]) can handle the coding scheme impact on final BER contour.

A statistical time-domain based approach with improved Tx jitter handling combining the accuracy of transient simulations is presented in this paper. This approach uses the concept of time-domain simulation of short bit patterns developed from the truth table and are arranged in unique fashion to account for the system non-linearity, jitter amplification, and correlation between the different waveforms. A procedure to accurately add driver jitter is also developed that addresses the initial phase selection problem and jitter correlation between different waveform patterns. The method is useful for applications where characterizing the jitter through the channel accurately is vital.

The procedure of generating BER contours with rigorous Tx jitter injection is discussed in Section 4.2. The definition of unique waveform patterns and the procedure to generate the probability density function (PDF) and cumulative density function (CDF) is also explained in Section 4.2. Validation of the method is done by comparing the BER contours from transient simulation of very long PRBS pattern in Section 4.3. The drawbacks of the proposed waveform-residual method are discussed in Section 4.4. Section 4.5 summarizes the paper.

4.2. PROPOSED METHOD

The entire process of generating the BER contours is divided into channel characterization, generation of time-domain output responses, and finally generating BER contours. The S-parameters of individual blocks that include connectors, backplane board, and plugged in daughter cards of a serial link along with PDN models are all assembled in a SPICE based transient simulator to obtain a step response. The channel characterization process to obtain the step response is shown in Figure 4.2.

The rise time of the step input applied at transmitter is chosen so that response captures the max frequency of the s-parameters. The impulse response of the channel transfer functions that include THRU and crosstalk are obtained by differentiating the step response. The voltage transfer function for the channel is obtained by applying the Fourier transform (FFT) on the impulse response. This step is based on the assumption that the system is linear. Complex real-world channels that have non-linear components can be assumed to behave linearly, as the step response obtained from the transient simulator has non-linear behavior embedded into an approximate linear model. The waveform-residual method to obtain the BER eye contours has a unique feature of including short bit patterns assembled from n bit truth table bit combinations. The truth table combinations cover all possible bit combinations that cover the entire frequency band of interest. The length of bit pattern is decided from the settling time of the pulse response of the channel. The second step of the end-end flow is shown in Figure 4.3.

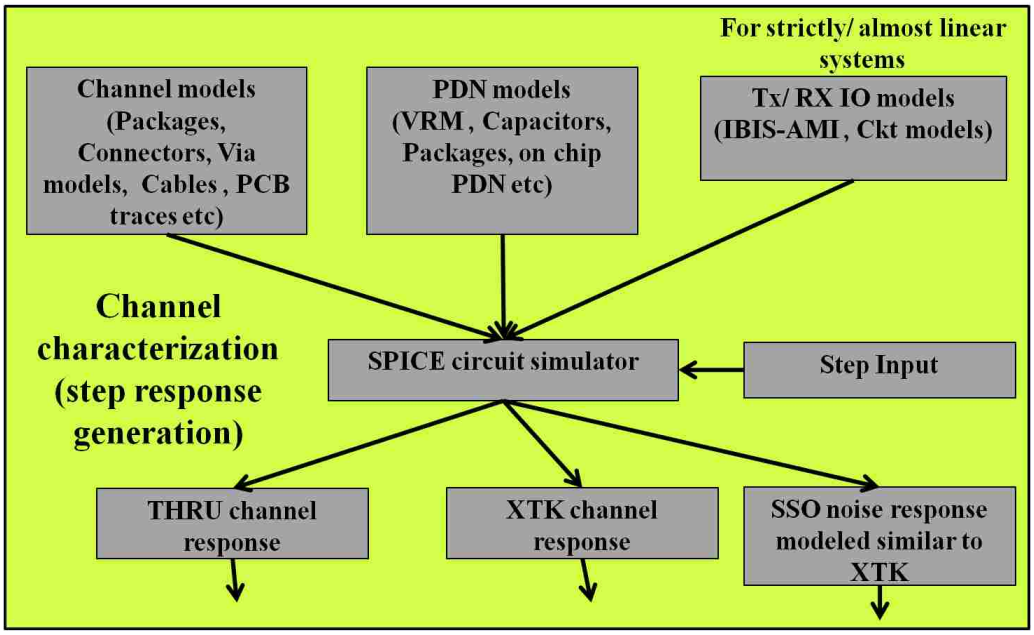

Figure 4.2. Channel characterization procedure

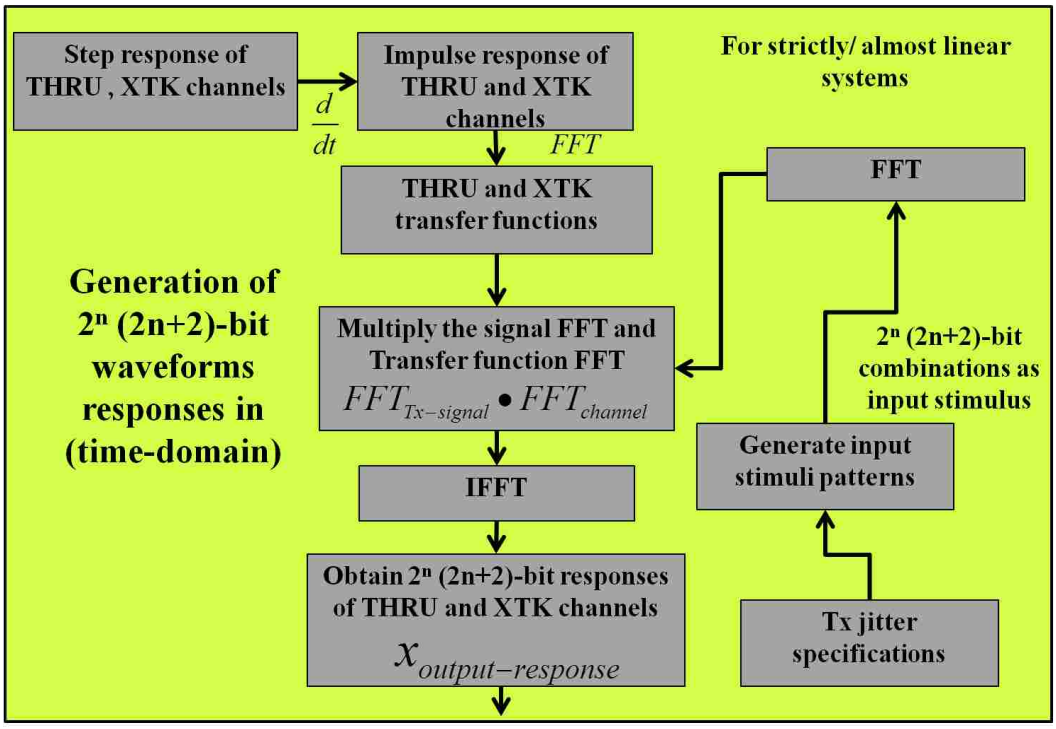

Figure 4.3. Generating the time-domain output response for all unique waveforms

The logic 1 and 0 bit definition defined by the user at the transmitter is shown in Figure 4.4. The unit interval (UI) of the input signal is related to the signaling speed by the relation.

$$UI = \frac{1}{signaling \quad speed} \tag{120}$$

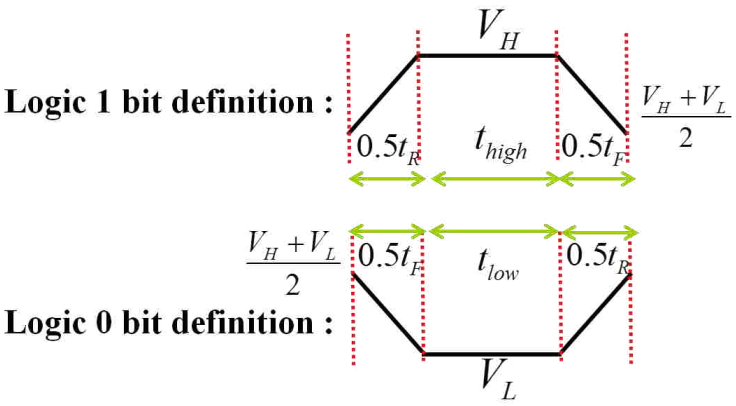

Figure 4.4. Logic "1" and Logic "0" bit definition

The pulse response of the channel under study shown in Figure 4.5 is obtained by giving pulse input at the input. The rise/fall times and signaling speed of the pulse input is same as the one used for statistical eye analysis. The pulse response of the channel is obtained by taking the inverse Fourier transform (IFFT) of the product the transfer function and the Fourier transform of the pulse input. The number of bits "N" needed to determine the truth table bit combinations is found from settling the time of the pulse response using energy stored in the pulse response where Δt is the sampling time. N_c is location of the main cursor in pulse response of the channel as shown in Figure 4.5.

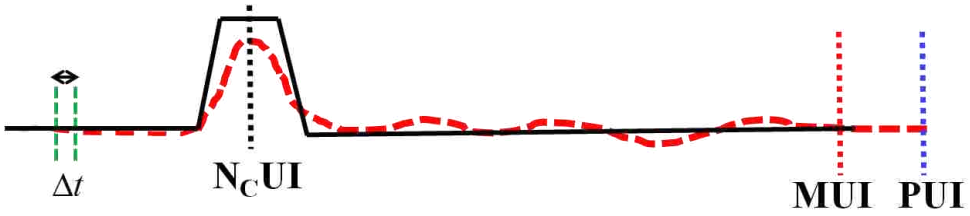

Figure 4.5. Pulse response of the channel to determine number of bits "N" needed

The number of bits N needed is related to settling time of the pulse response and main cursor location Nc. The settling time is also related to the energy in pulse response. P is the number of UIs after the pulse settles with no residual energy and is the end point in time of the transient simulation of pulse input.

$$\int_0^{MUI} \left(x_{pulse}(t)\right)^2 dt - \int_0^{MUI+PUI} \left(x_{pulse}(t)\right)^2 dt = 0 \tag{121}$$

$$N = M - N_c \tag{122}$$

The input stimulus is constructed from n-bit combinations of a binary count followed by the next occurring bit combination to capture the residual ISI. For example if n = 3, the bit sequence is 0-1-1-"000"-"001"-0-1, 0-0-0-"001"-"010"-0-0, and so on. This type of arrangement of the truth table pattern is sufficient for obtaining the BER contours, as all possible patterns are covered in the input stimulus and no extra information is obtained from analyzing other types of arrangements which are not sequential. The arrangement is constructed in a fashion to embed the continuity information between adjacent bit patterns to the current bit pattern. The arrangement of bit patterns to obtain the input waveforms 1, k, and 2^N is defined as shown in Figure 4.6. To maintain continuity between the successive patterns, the bit pattern 1 is arranged as a combination of last bit of pattern 2^N, followed by n bits of pattern 1, followed by n bits of pattern 2,

and finally followed by first bit of pattern 3. The first and last bits mimic the continuity of transient simulation as if all the patterns are arranged sequentially. The n bits of pattern 2 also serve the purpose of capturing the residual energy leaking from pattern 1 to pattern 2. There is no need to consider more than n bits of pattern 2, as the residual energy from the last bit of pattern 1 decays by nth bit of pattern 2 and will not influence the future bit patterns 3 to 2^N. The precursor ISI from pattern 2 on pattern 1 is also accounted for by arrangement of the bit patterns. Similarly, bit pattern k is arranged as a combination of last bit of pattern k - 1, followed by n bits of pattern k followed by n bits of pattern k + 1 and finally followed by first bit of pattern k + 1. Bit pattern 2^N is arranged as a combination of last bit of pattern 2^N-1, followed by n bits of pattern 2^N followed by n bits of pattern 1, and finally followed by first bit of pattern 2.The total number of bits in the final bit pattern after the arrangement is 2N+2, including the bits that are added to ensure the continuity between successive patterns.

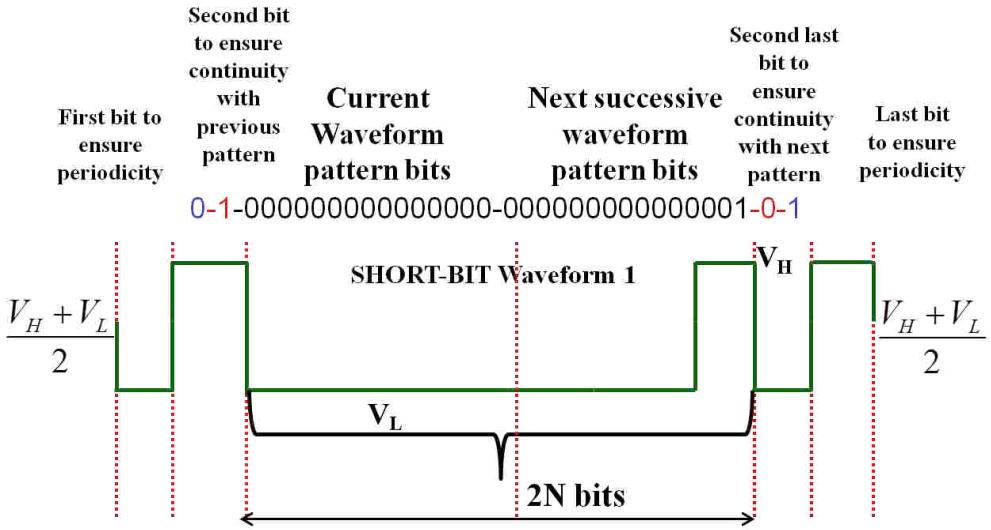

(a)

Figure 4.6. (a) Input stimulus definition from pattern 1 (b) Input stimulus definition from pattern 2 (c) Input stimulus definition from pattern 2^N

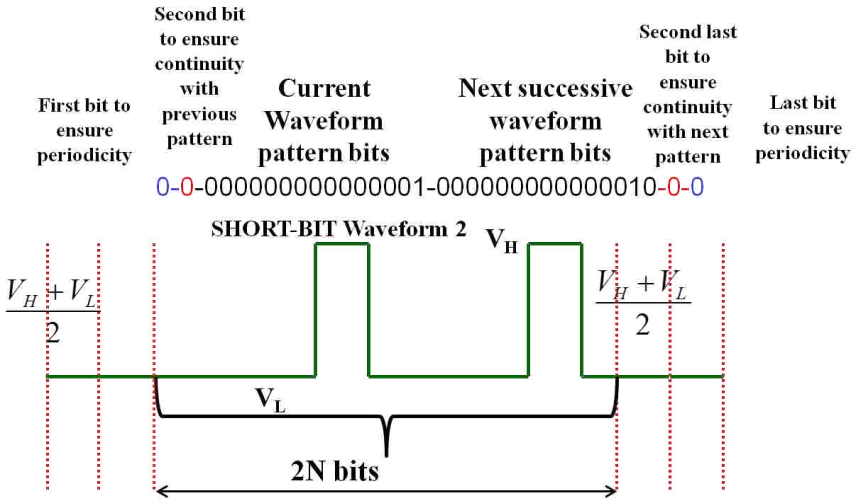

(b)

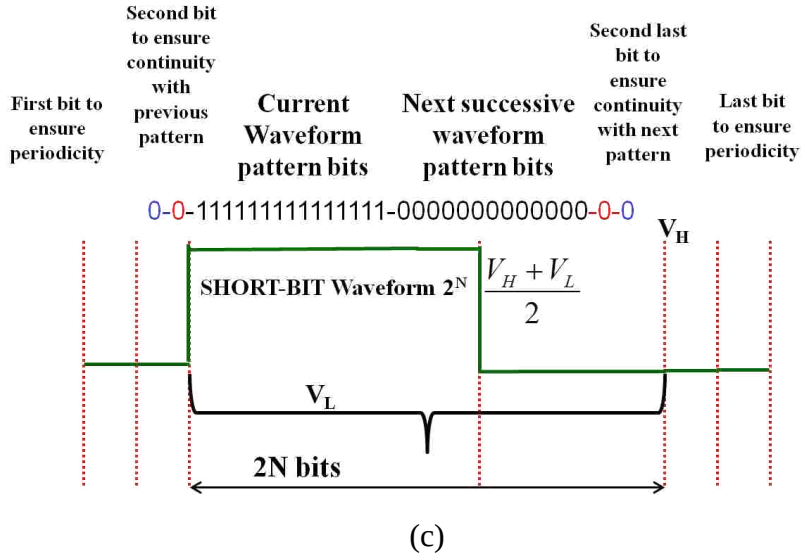

(c)

Figure 4.6. (a) Input stimulus definition from pattern 1 (b) Input stimulus definition from pattern 2 (c) Input stimulus definition from pattern 2^N (cont.)

The Fourier transform assumes that the input signal is periodic in nature, and so to ensure that FFT is performed accurately, two bits are added to the waveform pattern, one at the beginning and one at the end, as shown in Figure 4.6. The logic to decide the bits to be added at the ends is basically to ensure the periodicity of the waveform.

The amount of total Tx jitter injected into the waveforms consists of random jitter (RJ), periodic jitter (PJ), and duty cycle distortion (DCD) jitter. The total Tx jitter is given using equation (123).

$$t_{jitter} = t_{jitter}^{RJ} + t_{jitter}^{PJ} + t_{jitter}^{DCD} \tag{123}$$

Where t_{jitter}^{RJ} is the random jitter injected, t_{jitter}^{PJ} is the periodic jitter injected, and t_{jitter}^{DCD} is the DCD jitter injected. The Periodic jitter mathematical model t_{jitter}^{PJ} with pk-pk jitter amplitude PJ_{pk-pk} and periodic jitter modulation frequency f_{PJ} used to inject jitter in the input waveform patterns is explained in equation (124).

The mathematical model is designed to maintain the continuity between the different waveform patterns that is observed when very long bit patterns are simulated using SPICE simulators, as explained in Figure 4.1(b). Similar mathematical relations are used for random jitter and DCD jitter by changing the jitter modulation functions. An example sinusoidal jitter variation is shown in Figure 4.7. The jitter injected in the waveforms depends on the initial phase of PJ.

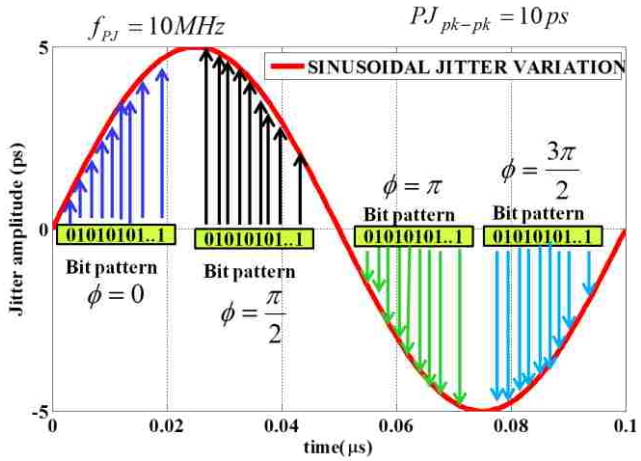

Figure 4.7. Importance of initial phase in sinusoidal jitter injection

The jitter injected into N bits of pattern k in kth waveform is

$$t_{jitter}^{PJ}[2:N+1]=\frac{PJ_{pk-pk}}{2t_{sampling}}\sin\left(2\pi f_{pj}t+\phi\right) \tag{124}$$

where,

$$\left(t=0+(k-1)NUI:UI:(N-1)UI+(k-1)NUI\right)$$

$$t_{sampling}=\Delta t=\frac{UI}{samples\_per\_UI}$$

$$1\le k\le 2^{N}$$

Each waveform is constructed by combining two adjacent bit patterns. The jitter injected in the N bits of pattern k+1 of kth waveform follows same mathematical model as described in equation (124). RJ and DCD jitter are modeled in same fashion as the PJ by just varying the jitter function. The initial phase of Tx driver PJ is random relative to the data pattern. It can take any value in the range . DCD jitter takes only two values due to its histogram characteristics. Since RJ is random, the accuracy of its injection does not depend on initial phase. The number of distinct phases to be considered is computed using the unit interval and PJ modulation frequency.

$$M=\frac{1}{f_{PJ}UI} \tag{125}$$

Sweeping the phase M times for every waveform is time consuming. A stochastic collocation method is used to select initial phase intelligently at select points in the interval. The probability of occurrence of M phase points is equal. Uniform distribution is used to model the initial phase. The Curtis-Clenshaw rule is used to find the weights of the selected grid points. The number of grid points selected is 1, 3, 5, 9, 17, 33, and so on, depending on how small the user wants the error of numerical integration to be. The

final input waveform is obtained from the individual input waveforms for every initial phase point selected using the Curtis-Clenshaw rule.

$$x_{k-input}(t) = w_1 x_{k-input}(t, \phi_1) + .. + w_n x_{k-input}(t, \phi_n) \tag{126}$$

The output response of the 2^N arranged unique bit patterns is obtained by taking the inverse Fourier transform of the product of the channel transfer function and the Fourier transform of the input bit patterns. The output response using a sampler with Δt sampling time after removing channel delay t_{delay} is given using the relation

$$x_{k-waveform} = x_{k-output}\left(\frac{t_{delay}}{\Delta t} + \frac{2UI}{\Delta t} + 1 : \frac{t_{delay}}{\Delta t} + (2N+2)\frac{UI}{\Delta t}\right) \tag{127}$$

The residual energy that is leaked from the first n bits of the truth table pattern is captured in the response of the next n bits of the next successive pattern and vice versa. The overall response of the constructed pattern k consists of the waveform part from truth table pattern k, residual from truth table pattern k into truth table pattern k + 1, and the waveform part from truth table pattern k + 1. This arrangement of bit patterns mimics the output response of 2^N bit patterns arranged in sequential fashion. It should be noted that the output response of 2^N bit patterns can also be obtained from any SPICE simulators without using the FFT/IFFT process if the system is strictly non-linear. The third step in the process of generating the BER contours from the waveform responses is shown in Figure 4.8.

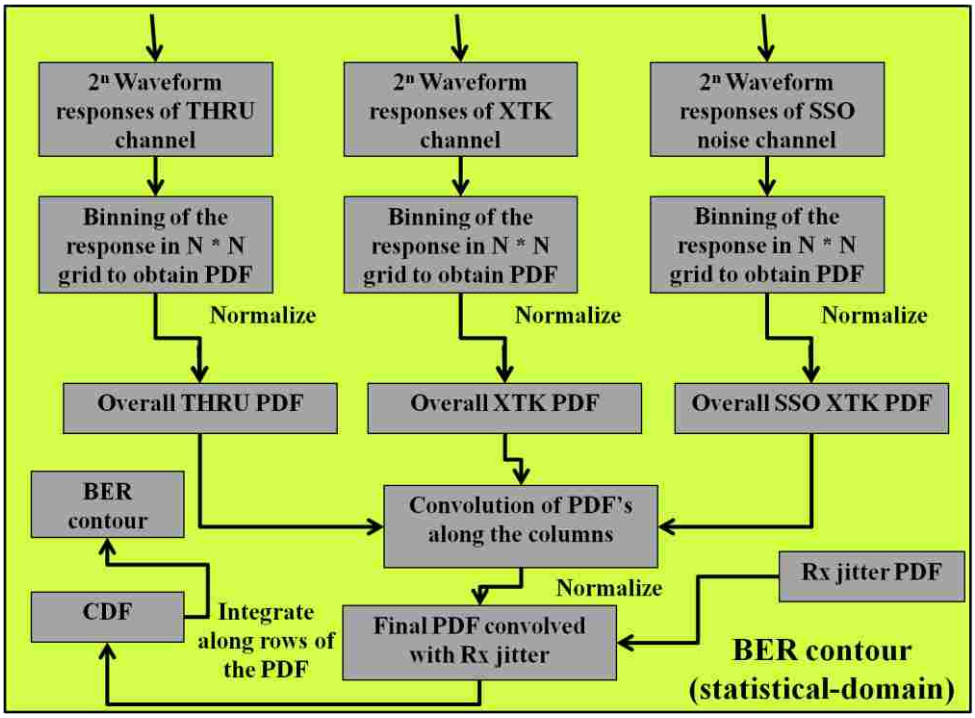

Figure 4.8. BER contour estimation from probability density function

An example showing the procedure to obtain the probability density function (PDF) grid matrix from the time domain waveform is shown in Figure 4.9. First, convert the time-domain data to the eye diagram, then make a 2D histogram, counting how many times the signal passes through each bin. Sum all instances for one time slice (all columns should equal the same value if the signal was interpolated properly, and should equal the number of bits that were sampled). Divide all bin values by this sum to normalize to a probability density value.

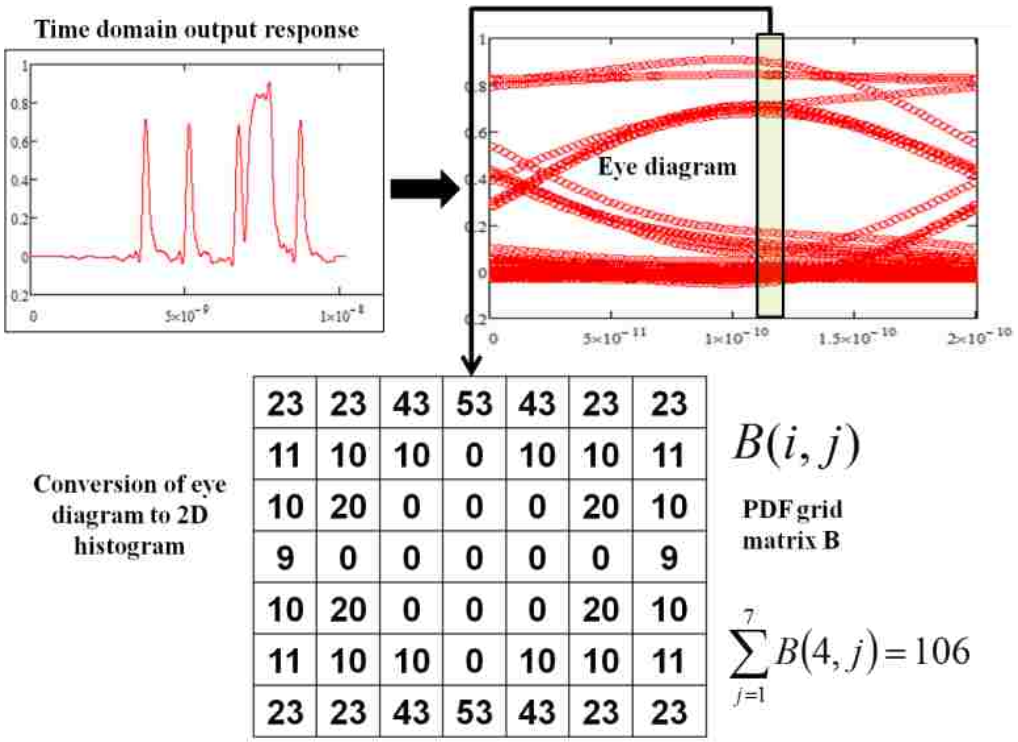

Figure 4.9. Illustration of generating waveform grid matrix

The waveform grid matrix of the output response is generated using the procedure explained in Figure 4.9. An eye diagram is formed from the waveform k response on a grid uniformly discretized with Q x Q cells, Q is user-defined grid size of the 2D-histogram. Each column of the grid captures the statistics of the waveform response at time ti. After normalization, a probability density function (PDF) is obtained for that column. This operation is repeated on all the columns of the grid to generate Q PDF's as shown in Figure 4.10. The overall waveform k grid matrix contains the statistics of truth table pattern k, truth table pattern k+1 including the residual energy leaking from truth table pattern k in to truth table pattern k + 1.

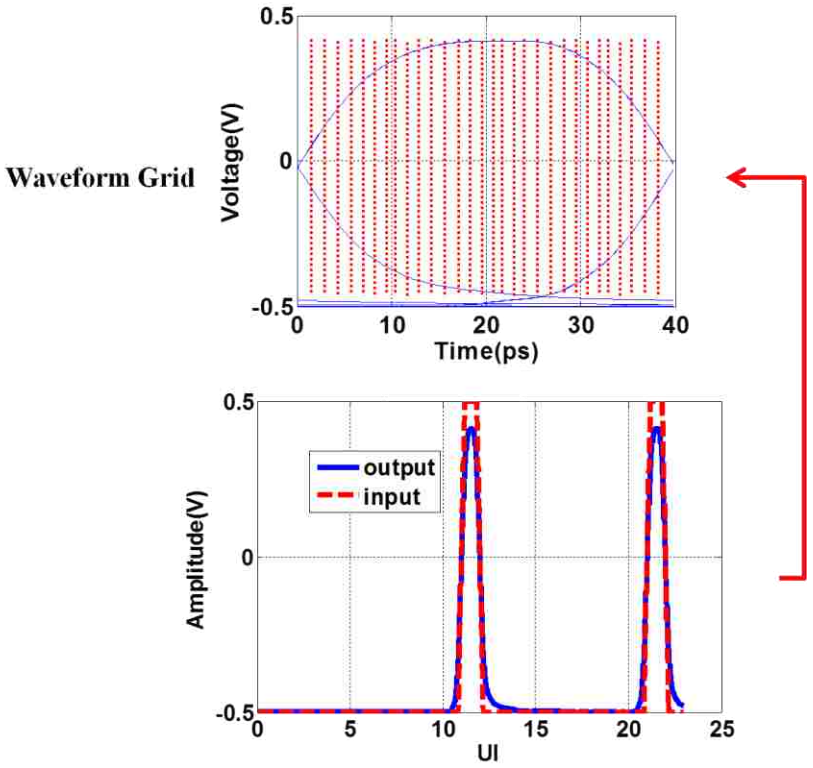

Figure 4.10. Waveform-residual PDF grid generation

The final PDF grid is obtained after the normalization of individual columns. Transient simulation of the sequential arrangement of waveform 2^N and waveform 1 generates output response where the output of waveform 1 is impacted by the residual energy leaking from waveform 2^N. This effect of transient simulation needs to be accounted for in the statistical BER contours for accurate channel characterization. This effect is captured by the arrangement of the truth table patterns, as explained in Figure 4.6. A similar procedure is performed to obtain the PDF of the remaining 2^N waveform patterns. The final overall waveform grid matrix is obtained by element-by-element summation of all waveform grid matrices from 2^N waveform patterns. The probability of the summation of 2^N random variables, defined by the statistics of waveforms 1 to 2^N PDF grid matrices, is given as convolution of the waveforms 1 to 2^N grid matrices. This

summation is equivalent to superposition of all waveforms into a single eye diagram. Normalization along the columns is performed to convert the final grid in to a PDF grid.

$$PDF_{overall} = \frac{\sum_{k=1}^{2^N} PDF_k}{sum\left(\sum_{k=1}^{2^N} PDF_k\right)} \tag{128}$$

The crosstalk effect from the aggressors is taken into account by generating the crosstalk waveform grids using similar waveform pattern arrangement and crosstalk transfer function. The overall PDF of the crosstalk waveform is computed. The impact of crosstalk is added on the eye contour with ISI by convolving the crosstalk and ISI waveform grids columns. The convolution procedure is the same as the summation of crosstalk and waveform response random variables. The convolution procedure is accurate, as crosstalk and ISI waveform are independent of each other. Normalization is then performed to obtain the probability density. It is important to span the voltage axis and timing axis limits using the same number of N x N cell grid. The convolution procedure is performed until all the crosstalk PDFs are exhausted.

$$PDF_{overall}^{ISI+XTK} = PDF_{overall}^{ISI} \otimes PDF_{overall}^{XTK} \tag{129}$$

The receiver jitter PDF is then convolved with the final PDF obtained after convolving the ISI and XTK PDFs. The cdf grid is obtained by integrating the final PDF grid along every column upwards and downwards from center cell of that column. The relations to convert from PDF to CDF are in (130) and (131).

$$CDF_{upper}^{i} = \int_{V_{medium-voltage-level}}^{V_K} PDF_{overall}(i,k)|_{k=mvl:V_H} \tag{130}$$

where,

$$i = 0 : UI$$

$$CDF_{lower}^{i} = \int_{V_{medium-voltage-level}}^{V_K} PDF_{overall}(i,k)|_{k=mvl:V_L} \tag{131}$$

The BER contour is generated by joining the points of equal probability on the cumulative distribution function (cdf) grid. An example of statistical BER contours generated by waveform-residual approach is shown in Figure 4.11.

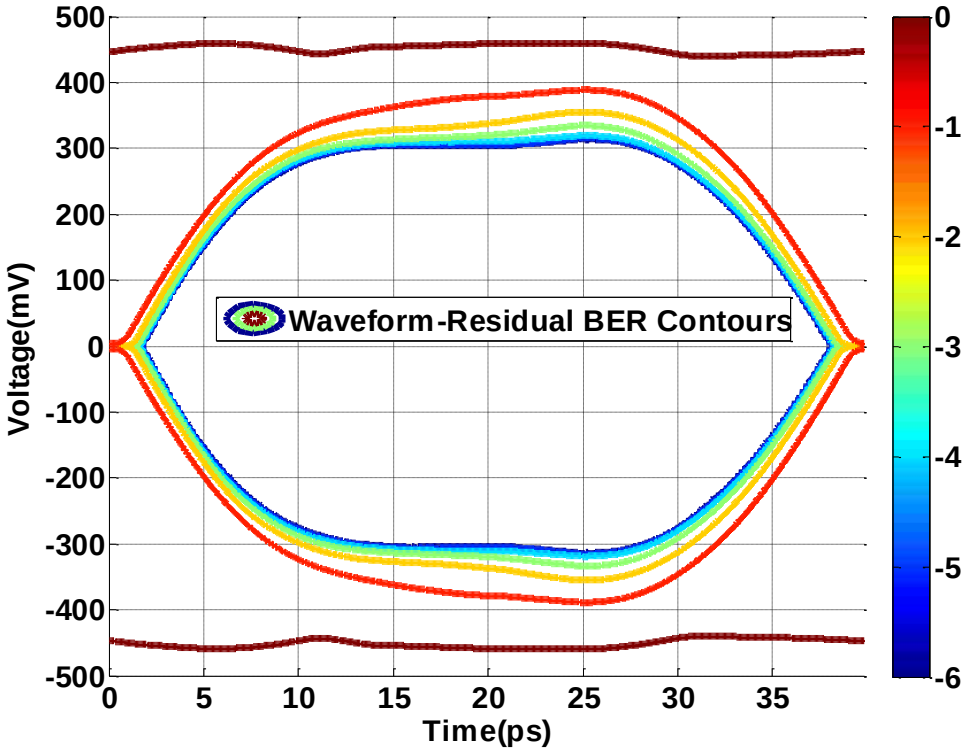

Figure 4.11. BER eye contours generated from CDF

4.3. EXAMPLES

The main focus of the proposed approach is to accurately capture Tx jitter and its effect through the channel in all the examples discussed here. Rx jitter handling is fairly straightforward and is discussed extensively in previous statistical based approaches. The geometry and stackup information of a broadside coupled link under study to estimate the crosstalk impact on BER contour is shown in Figure 4.12 and Figure 4.13. The overall coupled length is 2 inches. The dielectric material used has a relative permittivity of 3.7 and a loss tangent of 0.02 at 1GHz.

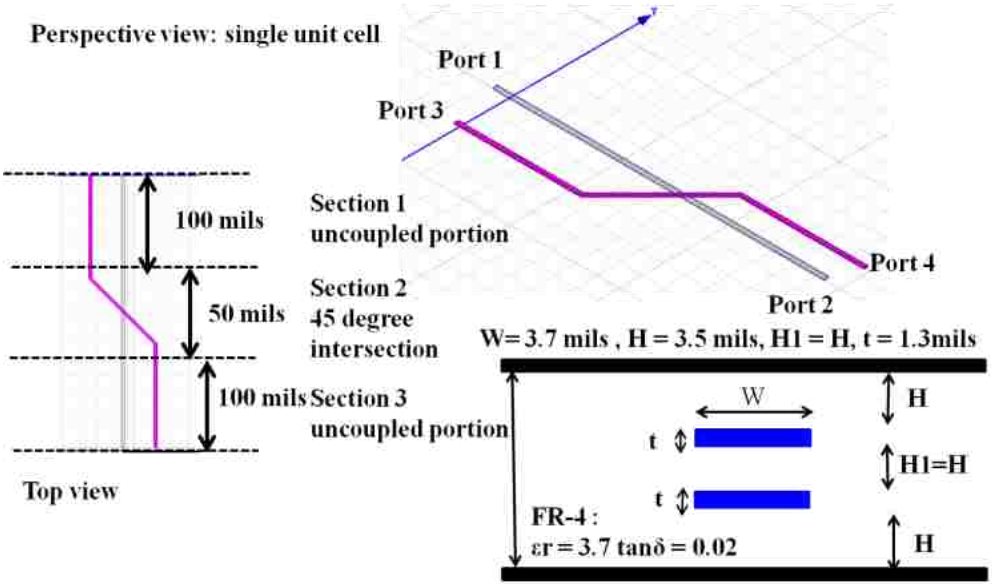

Figure 4.12. Geometry and stackup of fundamental part in overall structure

An input of 1V pk-pk with a rise/fall time of 14 ps at data rate of 25 Gbps is used on the victim. The number N obtained from pulse settling time is 11. The ISI jitter is deterministic in nature and it saturates by a BER of 1E-6 for this channel. It can be observed from Table 4.1 that the difference in the horizontal eye contour opening is less

than 1% between waveform-residual and brute force transient simulation of PRBS-18 pattern in the SPICE simulator. The S-parameter plots of return loss, insertion loss, NEXT and FEXT are shown in Figure 4.14. A waveform-residual approach is applied on the channel to generate the BER eye contours at BER = 1E-6, as shown in Figure 4.15

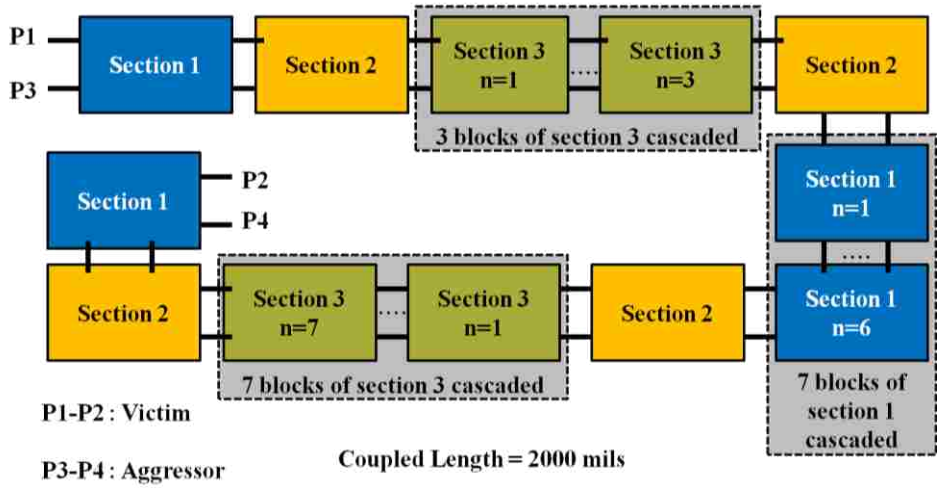

Figure 4.13. Connection of S-parameter blocks to create overall coupled structure

Table 4.1. Comparison of eye contour opening of channel with ISI and in-phase XTK at BER = 10^{-6}

Approach	Eye Width (ps)
Proposed Approach	34.1
SPICE simulation of PRBS-18	34

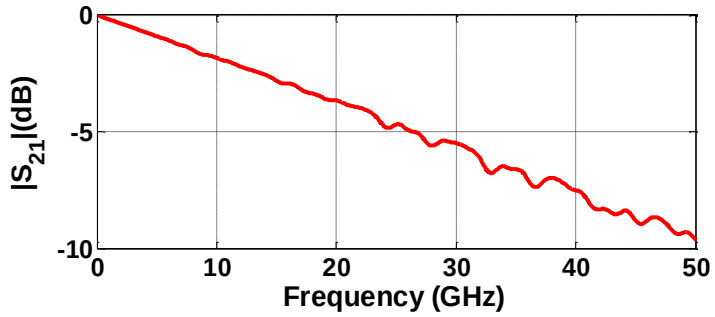

(a)

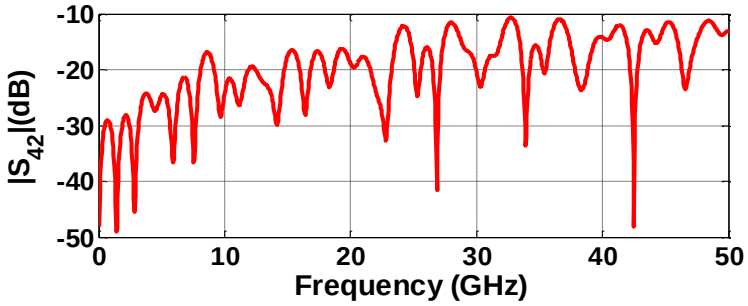

(b)

Figure 4.14. (a) Insertion Loss of victim channel (b) Near-End crosstalk due to aggressor on the victim channel

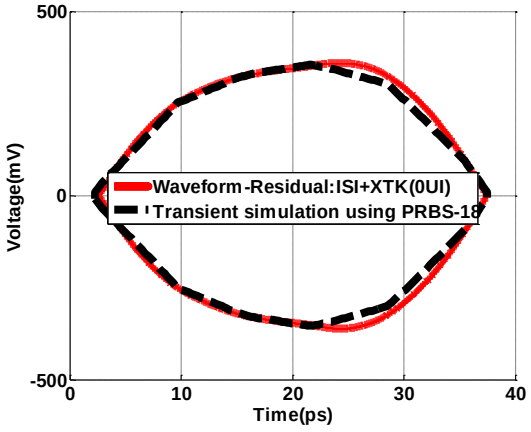

(a)

Figure 4.15. (a) Comparison of BER=10^{-6} contour from proposed method and SPICE simulation of PRBS-18 pattern (b) BER contour map using the proposed approach

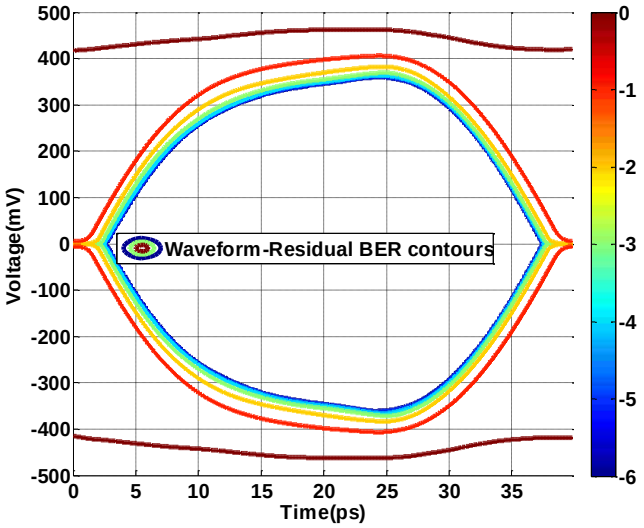

(b)

Figure 4.15. (a) Comparison of BER=10^{-6} contour from proposed method and SPICE simulation of PRBS-18 pattern (b) BER contour map using the proposed approach (cont.)

Periodic jitter of 10ps amplitude and 10MHz modulating frequency is injected at the input of the transmitter. The eye diagram obtained from proposed method with periodic jitter injected at Tx is shown in Figure 4.16.

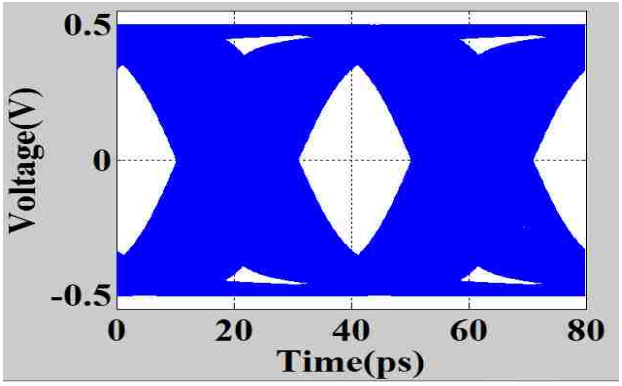

Figure 4.16. Eye diagram obtained from proposed method with 10ps PJ injected

The jitter statistics from the proposed method correlate very well with the eye diagram in Figure 4.1(b) obtained from transient simulation of PRBS-18. The waveform-residual convolution approach is applied on the victim channel to generate the eye contours at BER = 1E-6, which is shown in Figure 4.17.

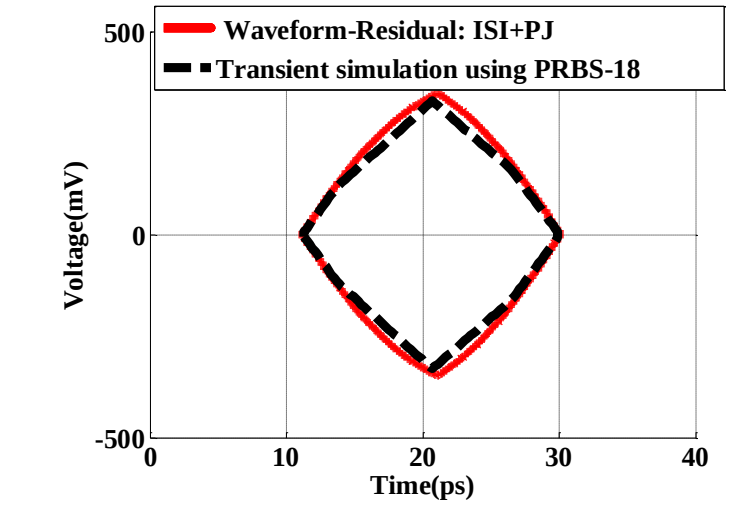

(a)

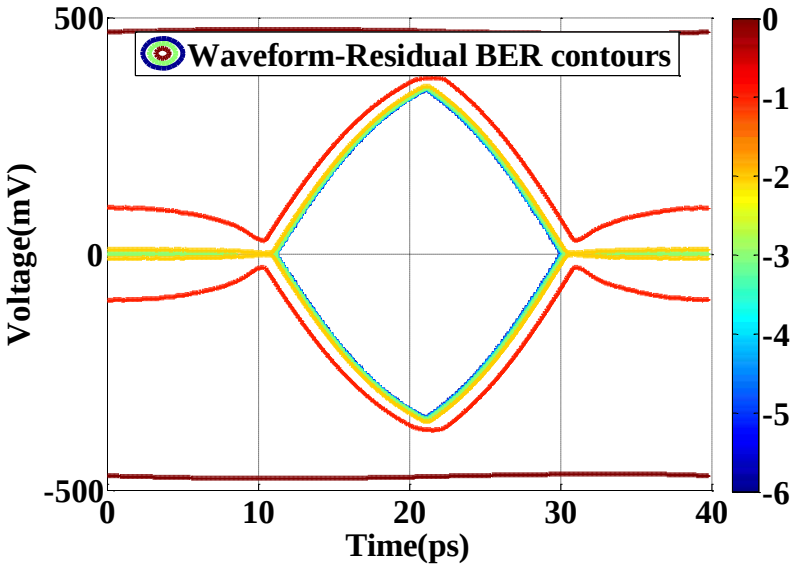

(b)

Figure 4.17. (a) Comparison of BER=10^{-6} contour from proposed method and SPICE simulation of PRBS-18 pattern with 10ps PJ (b) BER contour map using the proposed approach with 10ps PJ

It can be observed from Table 4.2 that differences in the horizontal eye contour opening is less than 1% between waveform-residual convolution method and transient simulation. The eye diagrams from the proposed approach and transient simulation of PRBS-18 pattern in SPICE simulator capture Tx periodic jitter characteristics accurately.

Table 4.2. Comparison of eye contour opening of channel with ISI and 10ps Tx PJ at BER = 10^{-6}

Approach	**Eye Width (ps)**
Proposed Approach	**18.9**
SPICE simulation of PRBS-18	**18.8**

The end to end signal link is built using two daughter cards connected through 12 inch differential flex cable using two hirose FH-41 connectors as shown in Figure 4.18. The overall setup is used to evaluate the quality of channel consisting of flex cable along with connectors rated at 4 Gbps. The S-parameter plots of return loss and insertion loss are shown in Figure 4.19. An input of 1V pk-pk with a rise/fall time of 87ps at data rate of 4 Gbps is used on the victim. The number N obtained from the pulse settling time is 15. Periodic jitter of 5ps amplitude and 10MHz modulating frequency is injected at the input of the transmitter. The waveform-residual approach is applied on the link, as described in Figure 4.18, to generate the eye contours at BER = 1E-6, as shown in Figure 4.20. It can be observed from Table 4.3 that the difference in the horizontal eye contour opening is negligible between waveform-residual method and transient simulation using PRBS-18.

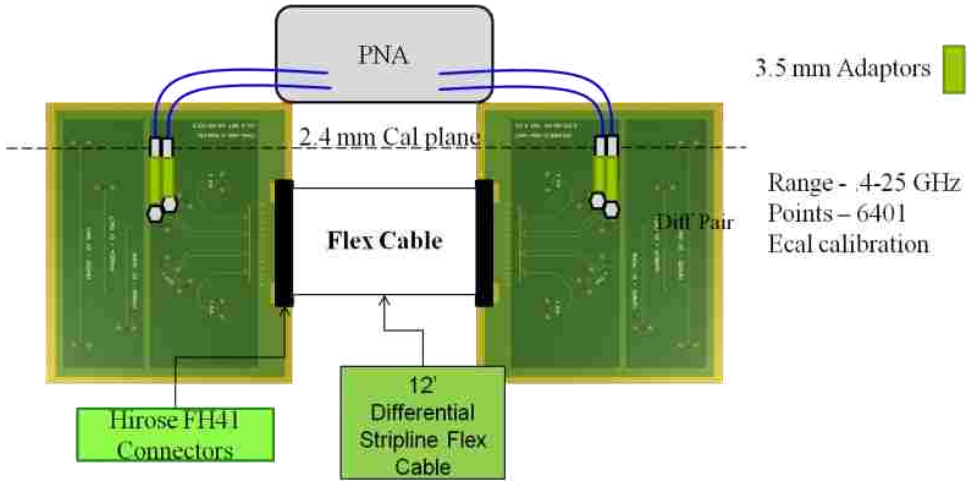

Figure 4.18. Channel consisting of two line cards connected through flex cable

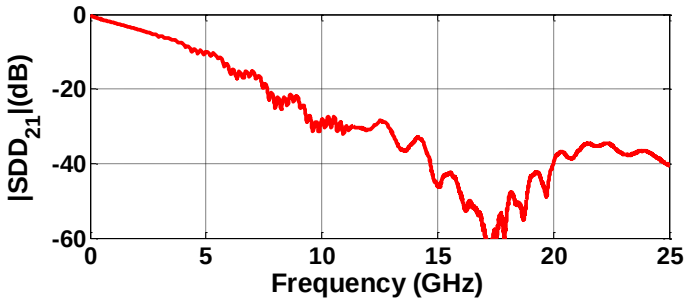

(a)

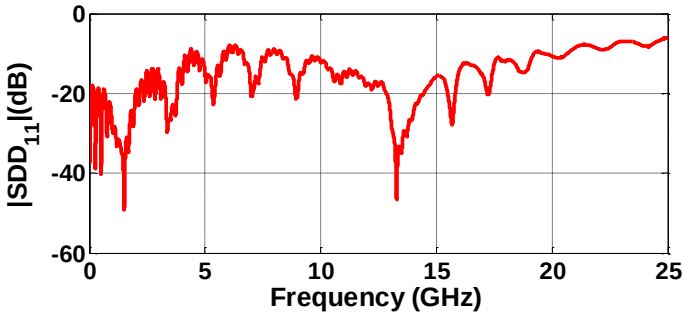

(b)

Figure 4.19. (a) Measured insertion loss of flex cable channel (b) Measured return loss of flex cable channel

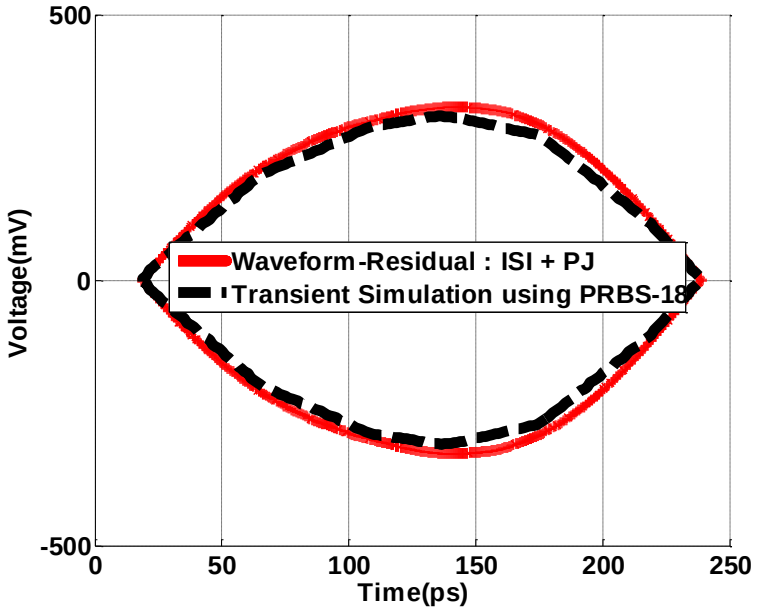

(a)

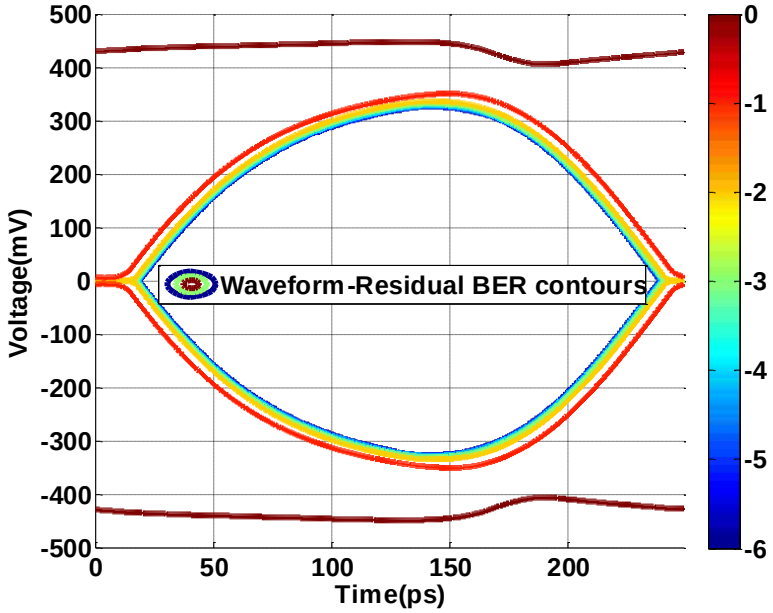

(b)

Figure 4.20. (a) Comparison of BER=10^{-6} contour from the proposed method and SPICE simulation of PRBS-18 pattern with 5ps PJ for flex cable channel (b) BER contour map using the proposed approach with 5ps PJ for flex cable channel

Table 4.3. Comparison of eye contour opening of flex cable channel with ISI and 5ps Tx PJ at BER = 10^{-6}

Approach	Eye Width (ps)
Proposed Approach	231.2
SPICE simulation of PRBS-18	231.2

4.4. DRAWBACKS OF THE METHOD

Extra time is consumed in accounting for the Tx jitter in a short bit waveform compared to the single bit pulse response or step response used in previous statistical approaches. Simulation time can be reduced for longer N bit patterns by utilizing the parallel processing capability. It is also important to ensure that pulse/step response settles and it satisfies passivity and causality conditions. If the pulse/step response does not settle due to S-parameter non-passivity and non-causality issues, then a large N value magnifies the error in the eye contour computation as discussed in [11]. All statistical approaches are sensitive to pulse response settling, passivity, and causality conditions.

4.5. CONCLUSIONS

With I/O data rates moving into the multi-Gb/s regime, signaling analysis techniques have evolved from simple empirical and worst-case analysis to a more comprehensive statistical analysis. Over lossy channels, there can be significant amplification of TX jitter, which can be captured by the waveform-residual method using the unique waveform patterns proposed in this paper. The proposed method is very useful for capturing Tx jitter through the channel. The proposed approach accounts for initial phase accurately. The jitter correlation observed in the transient simulation of very long sequences is also accurately captured. It is highly recommended for special design

problems where jitter analysis is very important. The method is sensitive to value of N, as increase in its value increases the simulation time. The simulation time can be reduced by utilizing parallel processing techniques. The settling of the response is important even in statistical methods utilizing single pulse/step input to get accurate BER contours.

BIBLIOGRAPHY

[1] S. Wu, "Modeling of Crosstalk between non-parallel striplines on adjacent layers," PhD Dissertation, Missouri S&T, 2011.

[2] K. Araki, F. Xiao and Y. Kami, "Simplified interference coupling model for two orthogonal striplines on adjacent layers," IEEE Trans. Commun., vol. E91-B, pp. 3983–3989, Dec. 2008.

[3] K. Araki, F. Xiao, Y. Kami, H. Bishnoi and J. Drewniak, "Modeling interference coupling between two orthogonal strip lines on adjacent layers," International symposium on EMC Europe, pp. 1–6, 2008.

[4] C. R. Paul, "Modeling electromagnetic interference properties of printed circuit boards," IBM J. Res. Dev., vol.33, no.1, pp. 33–50, 1989.

[5] F. M. Romeo and M. M. Santomauro, "Time-domain simulation on n-coupled transmission line network, " IEEE Trans. Microwave Theory Tech., fol. MTT-35, pp. 131–137, Feb. 1987.

[6] C. Wei, R. F. Harrington, J. R. Mautz and T. K. Sarkar, "Multiconductor transmission lines in multilayered dielectric media," IEEE Trans. Microwave Theory Tech., fol. MTT-32, pp. 439-450, Apr. 1984.

[7] F. Xiao, W. Liu and Y. Kami, "Analysis of crosstalk between finite-length microstrip lines: FDTD approach and circuit-concept modeling," IEEE Trans. on EMC., vol. 43, no.4, pp. 573–578, Nov. 2001.

[8] Y. Kami and W. Liu, "Analysis of coupling between transmission lines in arbitrary directions," IEEE International Symposium on EMC, vol. 2, pp. 952–957, 1998.

[9] C. R. Paul, Analysis of multiconductor transmission lines, Hoboken, NJ: John Wiley & Sons, Inc., 2008.

[10] A. R Chada, S. Wu, J. Fan, J. L. Drewniak, B. Mutnury, and D. N. de Araujo, "Modeling broadside coupled traces using Eq PUL RLGC model," IEEE EPEP Conference, 2012.

[11] A. Chada, B. Mutnury, D. Wallace, D. Winterberg, M. Wang, A.C. Scogna. "Simulation challenges in designing high speed serial links," in IEEE ECTC Conf., 2012.

[12] K. D. Marx, “Propagation Modes, Equivalent Circuits, and Characteristic Terminations for Multiconductor Transmission Lines with Inhomogeneous Dielectrics,” IEEE Trans. Microwave Theory Tech., vol. 21, no. 7, pp. 450–457, Jul. 1973.

[13] C. R. Paul, “Decoupling the Multiconductor Transmission Line Equations,” IEEE Trans. Microwave Theory Tech., vol. 44, no. 8, pp. 1429–1440, Aug. 1996.

[14] G.-T. Lei, G.-W. Pan, and B. K. Gilbert, “Examination, Clarification and Simplification of Modal Decoupling Method for Multiconductor Transmission Lines,” IEEE Trans. Microwave Theory Tech., vol. 43, no. 9, pp. 2090–2100, Sep. 1995.

[15] W. Shi and J. Fang, “Evaluation of Closed-Form Crosstalk Models of Coupled Transmission Lines,” IEEE Trans. Adv. Packag., Vol. 22, no. 2, May. 1999.

[16] S. H. Hall, G. W. Hall, and J. A. McCall, High Speed Digital System Design: A Handbook of Interconnect Theory and Design Practices. New York: Wiley, 2000, pp. 42–73.

[17] B. Young, Digital signal integrity: Modeling and Simulation with Interconnects and Packages, NJ, Prentice Hall, 2001.

[18] C. Wei, R. F. Harrington, J. R. Mautz, and T. K. Sarkar, “Multiconductor Transmission Lines in Multilayered Dielectric Media,” IEEE Trans. Microwave Theory Tech., Vol. MTT-32, pp. 439-450, Apr. 1984.

[19] J. F. Whitaker, T. B. Norris, G. Mourou, and T. Y. Hsiang, “Pulse Dispersion and Shaping in Microstrip Lines,” IEEE Trans. Microwave Theory Tech., vol. MTT-35, pp. 41-47, Jan. 1987.

[20] J. G. Richings and B. Easter, “Measured Odd and Even Mode Dispersion of Coupled Microstrip Lines,” IEEE Trans. Microwave Theory Tech., vol. 23, no. 10, pp. 826–828, Oct. 1975.

[21] C. R. Paul, “Literal Solutions for Time Domain Crosstalk on Lossless Transmission Lines,” IEEE Trans. Electromagn. Compat., vol. 34, no.4, pp. 433–444, Nov. 1992.

[22] J. Kim and J. F. Mcdonald, “Transient and Crosstalk Analysis of Slightly Lossy Interconnection Lines for Wafer Scale Integration and Wafer Scale Hybrid Packaging- Weak Coupling Case,” IEEE Trans. Circuits Syst., Vol. 35, no. 11, Nov. 1988.

[23] J. P. Gilb and C.A. Balanis, “Pulse Distortion on Multilayer Coupled Microstrip Lines,” IEEE Trans. Microwave Theory Tech., Vol. 37, no. 11, Apr. 1989.

[24] G. Blando, J. R. Miller, and I. Novak, "Losses Induced by Asymmetry in Differential Transmission Lines," Proc. of DesignCon 2007, Jan.31-Feb.3 2007, Santa Clara, CA.

[25] R. A. Speciale, "Even- and Odd-Mode Waves for Nonsymmetrical Coupled Lines in Nonhomogeneous Media," IEEE Trans. Microwave Theory Tech., Vol. MTT-23, no. 11, Nov. 1975.

[26] F. D. Mbairi and P. W. Siebert, "High-Frequency Transmission Lines Crosstalk Reduction Using Spacing Rules," IEEE Trans. Comp. Packag. Technol., Vol. 31, no. 3, Sept. 2008.

[27] I. Novak, B. Eged, and L. Hatvani, "Measurement and Simulation of Crosstalk Reduction by Discrete Discontinuities Along Coupled PCB Traces," IEEE Trans. Instrum. Meas., Vol. 43, no. 2, Nov. 1994.

[28] F. Broyde and E. Claveleir, "A New Method for the Reduction of Crosstalk and Echo in Multiconductor Interconnections," IEEE Trans. Circuits Syst., Vol. 52, no. 2, Feb. 2005.

[29] P. Muthana and H. Kroger, "Behavior of Short Pulses on Tightly Coupled Microstrip Lines and Reduction of Crosstalk by Using Overlying Dielectric," IEEE Trans. Adv. Packag., Vol. 30, no. 3, Aug. 2007.

[30] K. Lee, H.-B. Lee, H.-K. Jung, J.-Y. Sim, and H.-J. Park, "A Serpentine Guard Trace to Reduce the Far-End Crosstalk Voltage and the Crosstalk Induced Timing Jitter of Parallel Microstrip Lines," IEEE Trans. Adv. Packag., vol. 31, no. 4, pp. 809–817, Nov. 2008.

[31] T. Ciamulski and W. K. Gwarek, "Coupling Compensation Concept Applied to Crosstalk Cancelling in Multiconductor Transmission Lines," IEEE Trans. Electromagn. Compat., Vol. 50, no. 6, pp. 437–441, May 2008.

[32] J. Lee, S. Lee, and S. Nam, "Active Crosstalk Cancellation for Next-Generation Single-ended Memory Interfaces," IEEE Trans. Electromagn. Compat., Vol. 53, no. 2, May. 2011.

[33] S. G. Johnson and J. D. Joannopoulus, Photonic Crystals: The Road From Theory to Practice. Boston, MA: Kluwer, 2002.

[34] L. Brillouin, Wave Propagation in Periodic Structure. New York: Dover, 1953.

[35] R. E. Collin, Field Theory of Guided Waves. New York: McGraw-Hill, 1960.

[36] P. J. B. Clarricoats and M. I. Sobhy, "Propagation behavior of periodically loaded waveguides," Proc. Inst. Elect. Eng., vol. 115, pp. 652–661, 1968.

[37] G. H. Bryant, “Propagation in corrugated waveguides,” Proc. Inst. Elect. Eng., vol. 116, pp. 203–213, 1969.

[38] P. J. B. Clarricoats and P. K. Saha, “Propagation and radiation behavior of corrugated feeds,” Proc. Inst. Elect. Eng., vol. 118, pp. 1167–1176, Sep. 1971.

[39] M. S. Navarro, T. E. Rozzi, and Y. T. Lo, “Propagation in a rectangular waveguide periodically loaded with resonant irises,” IEEE Trans. Microw. Theory Tech., vol. MTT-28, no. 8, pp. 857–865, Aug. 1980.

[40] R. Lech and J. Mazur, “Propagation in rectangular waveguide periodically loaded with cylindrical posts,” IEEE Microw. Wireless Compon. Lett., vol. 14, no. 4, pp. 177–179, Apr. 2004.

[41] S.-G. Mao and M.-Y. Chen, “Propagation characteristics of finite-width conductor-backed coplanar waveguides with periodic electromagnetic bandgap cells,” IEEE Trans. Microw. Theory Tech., vol. 50, no. 11, pp. 2624–2628, Nov. 2002.

[42] L. Zhu, “Guided-wave characteristics of periodic coplanar waveguides with inductive loading-unit-length transmission parameters,” IEEE Trans. Microw. Theory Tech., vol. 51, no. 10, pp. 2133–2138, Oct. 2003.

[43] R. S. Kshetrimayum and L. Zhu, “Guided-wave characteristics of waveguide based periodic structures loaded with various FSS strip layers,” IEEE Trans. Antennas Propag., vol. 53, no. 1, pp. 120–124, Jan. 2005.

[44] Y. L. R. Lee, A. Chauraya, D. S. Lockyer, and J. C. Vardaxoglou, “Dipole and tripole metallodielectric photonic bandgap (mpbg) structures for microwave filter and antenna applications,” IEEE Proc. Optoelectronics, vol. 147, pp. 395–400, Dec. 2000.

[45] B. Lenoir, D. B. S. Verdeyme, P. Guillon, C. Zanchi, and J. Puech, “Periodic structures for original design of voluminous and planar microwave filters,” IEEE MTT-S International Microwave Symposium Digest, vol. 3, pp. 1479–1482, May 2001.

[46] G. R. Simpson, “A generalized n-port cascade connection,” IEEE MTT-S. International Symposium, pp. 507–509, 1981.

[47] J. Choi, V. Govind, and M. M Swaminathan, “A novel electromagnetic bandgap (EBG) structure for mixed-signal system applications,” IEEE Radio and Wireless Conference, pp. 243–246, Sep. 2004.

[48] R. Abhari and G. V. Eleftheriades, “Suppression of the parallel-plate noise in highspeed circuits using a metallic electromagnetic band-gap structure,” IEEE MTT-S International Microwave Symposium Digest, vol. 1, pp. 493–496, Jun. 2002.

[49] R. Abhari and G. V. Eleftheriades, “Metallo-dielectric electromagnetic bandgap structures for suppression and isolation of the parallel-plate noise in high-speed circuits,” IEEE Trans. Microw. Theory Tech., vol. 51, pp. 1629–1639, Jun. 2003.

[50] S. Shahparnia and O. M. Ramahi, “Electromagnetic interference (EMI) reduction from printed circuit boards (PCB) using Electromagnetic bandgap structures,” IEEE Trans. Electrom. Compat., vol. 46, no. 4, pp. 580–586, Nov. 2006.

[51] T. L. Wu, Y. Y. Lin, C. C. Wang, and S. T. Chen, “Electromagnetic bandgap power/ground planes for wideband suppression of ground bounce noise and radiated emission in high-speed circuits,” IEEE Trans. Microw. Theory Tech., vol. 53, no. 9, pp. 2935–2942, Sep. 2005.

[52] J. Qin, O. M. Ramahi, and V. Granatstein, “Novel planar electromagnetic bandgap structures for mitigation of switching noise and EMI reduction in high-speed circuits,” IEEE Trans. Electromag. Compat., vol. 49, no. 3, pp. 661–669, Aug. 2007.

[53] G. Goussetis, A. Feresidis, and P. Kosmas, “Efficient analysis, design, and filter applications of EBG waveguide with periodic resonant loads,” IEEE Trans. Microw. Theory Tech., vol. 54, no. 11, pp. 3885–3892, Nov. 2006.

[54] B. Casper, M. Haycock, and R. Mooney. “An accurate and efficient analysis method for multi-Gb/s chip-to-chip signaling schemes,” in IEEE Very Large Scale (VLSI) Circuits Symp. Tech. Papers, Jun. 2002, pp. 54–57.

[55] B. Casper et al. “Future microprocessor interfaces: Analysis, design and optimization,” in IEEE Custom Integrated Circuits Conf., 2007, pp. 479–486.

[56] V. Stojanovic and M. Horowitz, “Modeling and analysis of High-speed links,” in IEEE Custom Integrated Circuits Conf., Sep. 2003, pp. 589–594.

[57] A. Sanders, M. Resso, and J. D’Ambrosia. “Channel compliance testing utilizing novel statistical eye methodology,” presented at the DesignCon, Santa Clara, CA, Feb. 2004.

[58] F. Lambrecht, Q. Lin, S. Chang, D. Oh, C. Yuan, and V. Stojanovic, “Accurate system voltage and timing margin simulation in CDR based high speed designs,” in Proc. IEEE 15th Topical Meeting Electrical Performance Electron. Packag, EPEP’06, Oct. 23–25, 2006, pp.171–174.

[59] D. Oh, F. Lambrecht, S. Chang, Q. Lin, J. Ren, J. Zerbe, C. Yuan, C. Madden, and V. Stojanovic, "Accurate method for analyzing highspeed I/O system performance," presented at the DesignCon, Santa Clara, CA, Feb. 2007.

[60] F. Lambrecht, C.-C. Huang, and M. Fox, "Technique for determining performance characteristics of electronic systems," U.S. Patent 6775809, Mar. 14, 2002.

[61] D. Oh, F. Lambrecht, J.-H. Ren, S. Chang, B. Chia, C. Madden, and C. Yuan. "Prediction of system performance based on component jitter and noise budgets," in Proc. IEEE 16th Electr. Perform. Electron. Packag., Atlanta, GA, Oct. 2007, pp. 33–36.

[62] S. Chang, D. Oh, and C. Madden. "Jitter modeling in statistical link simulation," in Proc. IEEE Int. Symp. Electromagn. Compat., Detroit, MI, Aug. 2008, pp. 1–4.

[63] K. Xiao, B. Lee, and X. Ye, "A flexible and efficient bit error rate simulation method for high-speed differential link analysis using time domain interpolation and superposition," in Proc. IEEE Int. Symp. Electromagn. Compat., Detroit, MI, Aug. 2008, pp. 1–6.

[64] D. Oh. "Multiple edge responses for fast and accurate system simulations," in Proc. IEEE 15th Electr. Perform. Electron. Packag., Scottsdale, AZ, Oct. 2006, pp. 163–166.

[65] J. Ren and D. Oh. "Multiple edge responses for fast and accurate system simulations," IEEE Trans. Adv. Packag., vol. 31, no. 4, pp. 741–748, Nov. 2008.

[66] Y. Chang and D. Oh. "Fast ISI characterization of passive channels using extreme value distribution," in Proc. IEEE 16th Electr. Perform. Electron. Packag., Atlanta, GA, Oct. 2007, pp. 127–130.

[67] J. Ren, D. Oh, S. Chang, and F. Lambrecht. "Statistical link analysis of high-speed memory I/O interfaces during simultaneous switching events," in Proc. IEEE 17th Electr. Perform. Electron. Packag., San Jose, CA, Oct. 2008, pp. 25–28.

[68] J. Ren and D. Oh. "Multiple edge responses for fast and accurate system simulations," IEEE Trans. Adv. Packag., vol. 31, no. 4, pp. 741–748, Nov. 2008.

[69] F. Rao, V. Borich, H. Abebe, M. Yan, J. Ren, J. Zerbe, C. Yuan, C. Madden, and V. Stojanovic. "Rigorous Modeling of Transmit Jitter for Accurate and Efficient Statistical Eye Simulation," presented at the DesignCon, Santa Clara, CA, Feb. 2007.

[70] Zhaoqing Chen, Wiren Dale Becker, George Katopis. “A New Approach to Deriving Packaging System Statistical Eye Diagram Based on Parallel Non-Linear Transient Simulations Using Multiple Short Signal Bit Patterns,” in IEEE ECTC Conf., 2012.

VITA

Arun Reddy Chada did his schooling at the Sandeepam Vidyalaya High School, Hyderabad, India (1989-2000) and the Sri Chaitanya Junior Kalasala, Hyderabad, India (2000-2002) before going to Indian Institute of Technology (IIT), Guwahati, India for his Bachelor of Engineering degree in Electronics Engineering (2006). Thereafter, he went to the Missouri University of Science and Technology, where he received his Masters Degree in Electrical Engineering from the Department of Electrical and Computer Engineering in December 2009. He received his Ph.D. Electrical Engineering in December 2014, from Missouri University of Science and Technology.